Dissertation

submitted to the
Combined Faculties for the Natural Sciences and for Mathematics
of the Ruperto-Carola University of Heidelberg, Germany
for the degree of

Doctor of Natural Sciences

Put forward by

M.Sc. Wasim Abuillan

Born in Althahria, Palestine.

Oral examination: 13th November 2013

Fine-Structures, Lateral Correlation and Diffusion of Membrane-Associated Proteins on Biological Membrane Surfaces

Referees: Prof. Dr. Motomu Tanaka

Prof. Dr. Ulrich Schwarz

Fine-Structures, Lateral Correlation and Diffusion of Membrane-Associated Proteins on Biological Membrane Surfaces

The primary aim of this thesis is to investigate the lateral diffusion, correlation and interactions of proteins and peptides with cell membrane models by the combination of experimental techniques in real and reciprocal space. In Chapter 4, the characteristic distance and range of lateral correlation between non-crystalline proteins anchored to fluid lipid monolayers at high surface densities were determined by grazing incidence small angle X-ray scattering (GISAXS) for the first time. Moreover, the lateral density of membrane-anchored proteins could be quantified from Sulfur Kα emission detected by grazing incidence X-ray fluorescence (GIXF). In Chapter 5, the influence of molecular crowding on the lateral diffusion of membrane-anchored proteins was investigated by fluorescence recovery after photobleaching and single particle tracking microscopy, yielding a clear transition from free diffusion to confined diffusion. In Chapter 6, the interactions between antimicrobial peptides and bacterial membrane models are probed by GIXF that allows for the identification of the spatial localization of ions with Ångstrom accuracy. This enabled one to discriminate different "modes" of membrane-protein interactions, such as adsorption and incorporation on the molecular level. The obtained results demonstrated that the use of real and reciprocal space techniques can provide information about fine-structures, electrostatics, and dynamic correlation at biological interfaces.

Feinstrukturen, laterale Korrelation und Diffusion der membranassoziierten Proteine auf biologischen Membranoberflächen

Das Hauptziel dieser Arbeit war die Untersuchung der Diffusion, Korrelation und Wechselwirkungen von Proteinen und Peptiden mit zellähnlichen Modellmembranen durch Kombination experimenteller Techniken im realen und reziproken Raum. In Kapitel 4 konnten zum ersten Mal die charakteristische Distanz und Reichweite der lateralen Wechselwirkungen zwischen nicht kristallinen Proteinen, die an fluide Lipidmonolagen in hoher Oberflächendichte gebunden waren, mit Hilfe von Kleinwinkel-Röntgenstreuung (GISAXS) bestimmt werden. Desweiteren konnte die laterale Dichte der membran-gebundenen Proteine anhand der Schwefel Kα Emission, die mit Hilfe der Röntgen-Fluoreszenz Analyse erhalten wurde, quantitativ bestimmt werden. In Kapitel 5 wurde der Einfluss der hohen molekularen Dichte auf die laterale Diffusion der membran-gebundenen Proteine mittels FRAP (*Fluorescence Recovery after Photobleaching)* und Einzelmolekülspektroskopie untersucht, woraus ein klarer Übergang von freier zu eingeschränkter Diffusion resultierte. In Kapitel 6 wurden die Wechselwirkungen zwischen antimikrobiellen Peptiden und bakteriellen Modellmembranen mittels GIXF erforscht, was die Identifizierung der räumlichen Anordnung der Ionen in der Größenordnung von Ångström ermöglichte. Dadurch konnten verschiedene Zustände der Membran-Protein-Wechselwirkungen wie z.B. Adsorption und Einlagerung in die Membran auf molekularer Ebene voneinander unterschieden werden. Die erhaltenen Ergebnisse zeigten, dass die Kombination optischer Techniken im realen und reziproken Raum Informationen über Feinstrukturen, Elektrostatik und dynamische Korrelation an biologischen Grenzflächen gewonnen werden können.

ACKNOWLEDGEMENTS

I would like to thank

Prof. Motomu Tanaka for guidance and discussions beside his support to make this happen,

Prof. Ulrich Schwarz for acting as my reviewer,

Prof. Markus Engstler for the great collaboration,

Prof. Klaus Brandenburg for the collaboration and supplying the LPSs,

Dr. Emmanuel Schneck, Dr. Hiroshi Yoshikawa, Dr. Thomas Schubert, Dr. Thomas Kaindl, Dr. Murat Tutus and Dr. Fernanda Rossetti for the fruitful scientific discussions and their help during my PhD work,

Dr. Ali Makky, Dr. Conni Monzel and Dr. Stefan Kaufman for their help in corrections and translation,

Dr. Oleg Konovalov, Dr, Alexei Vorobiev and Dr. Bruno Demé for their help in scattering experiments,

Alexander Körner, Alexandra Burk, Nataliya Frenkel and Mariam Veshgini for spending great time at the beamlines carrying out experiments mixed with social and scientific discussions,

Agatha Korytowski, Victoria Frank, Harden Rieger, Moritz Herrmann, Akihisa Yamamoto and Rami Mandow for discussions on scattering results and others,

Andreas Hartel, Thien-Ly Julia Dinh and Stephen Krämer for working together in FRAP and SPT experiments,

Finally many thanks go to my family for their spiritual support especially my wife and my two little sons Muhammad and Qais.

The important thing in science is not so much to obtain new facts as to discover new ways of thinking about them.

William H. Bragg

Table of Contents

1. Introduction 1

2. Theoretical Background 8

2.1 Basic introduction 8

2.1.1 Self-assembly of membranes 8

2.1.2 Phase behavior of lipids 9

2.1.3 Lateral diffusion 10

2.2 X-ray scattering 13

2.2.1 X-ray interaction with matter 13

2.1.2 Basics of X-ray scattering 14

2.2.3 Refractive index 16

2.3 Specular X-ray reflectivity 17

2.3.1 Reflection from a single smooth interface 17

2.3.2 The Born approximation 21

2.3.3 Rough interface 22

2.3.4 Reflectivity from stratified layers 22

2.4 Grazing incidence small angle X-ray scattering 25

2.4.1 Form factor in the DWBA (dilute case) 26

2.4.2 Structure factor (Concentrated case) 30

2.5 Grazing incidence X-ray fluorescence 32

3. Materials and Methods 37

3.1 Materials 37

3.1.1 Lipids 37

3.1.2 Lipopolaysaccarides 37

3.1.3 Proteins and peptides 38

3.1.3 Fluorophores 41

3.1.3 Chemicals and buffers 41

3.2 Preparations 42

3.2.1 Suspensions and solutions 42

3.2.2 Preparation methods 43
3.2 Methods 47
3.2.1 Specular X-ray reflectivity 47
3.2.2 Grazing incidence small angle scattering 49
3.2.3 Grazing incidence X-ray fluorescence 50
3.2.4 Fluorescence recovery after photobleaching 52
3.2.4 Single particle tracking 53

4. Lateral Correlation between Membrane-Anchored Proteins 56

4.1 Structure of proteins anchored on membrane surfaces 57
4.2 Correlation between membrane-anchored proteins 62
4.3 Lateral density of membrane-anchored proteins 65

5. Lateral Diffusion of Membrane-Anchored Proteins 69

5.1 The structure of membrane-anchored protein 69
5.1.1Structure of neutravidin proteins bound to membrane lipid bilayer 69
5.1.2 Structure of VSG incorporated into membrane lipid bilayer 73
5.2 Lateral diffusion of membrane-anchored proteins in crowded systems 76
5.2.1 Molecular crowding threshold of membrane-anchored proteins 76
5.2.2 N-linked glycans reduce the molecular crowding threshold of membrane-anchored proteins 79
5.3 Lateral diffusion of membrane-anchored proteins on sub-micron length scale 81
5.3.1 SPT revealed transition from free to confined diffusion for membrane-anchored proteins 81
5.3.2 Non-VSG proteins hamper the VSG lateral diffusion on the surface of Trypanosoma brucei 84

6. Physical Interactions of Peptides with Bacterial Cell Membranes 88

6.1 Influence of Ca^{2+} ions on bacterial membrane 88
6.1.1 Pressure-area isotherms of LPS Ra monolayers 88
6.1.2 Influence of Ca^{2+} ions on the structure of LPS Ra membranes 90
6.1.2 Influence of Ca^{2+} ions on the electrostatics of LPS Ra membranes 91

6.2 Interactions of peptide drugs with bacterial membrane 97
6.2.1 Interaction of anti-sepsis peptide with LPS Ra monolayer..... 97
6.2.2 Interaction of fish protamine with LPS Ra monolayer 102

Appendix 110

Bibliography 117

1. Introduction

Cell membranes are crucial components to the life of cells and organelles. Biological membranes surrounding the cell body define the boundaries between interior and exterior of cells and sustain the stable shape. They consist of lipid bilayers and membrane-associated proteins, and a variety of carbohydrates are attached to the membrane surface (Fig. 1.1), facilitating communication and transport of nutrients and waste between cells and their surrounding environments [1]. Looking into molecular components, lipids are amphiphilic molecules possessing hydrophilic head groups and hydrophobic hydrocarbon chains. In aqueous solution, lipids form a self-assembled bilayer through the entropy-driven hydrophobic effect [2]. Singer and Nicolson provided a model called the fluid-mosaic model [3] which considers the lipid bilayer as two dimensional fluid matrix in which the proteins have a degree of motion that in turn leads to a dramatic impact on their activity and physiological function [4]. The fluidity of the cell membrane is biologically important. For instance, certain membrane transport processes and enzyme activity can be ceased when the membrane fluidity is decreased [5].

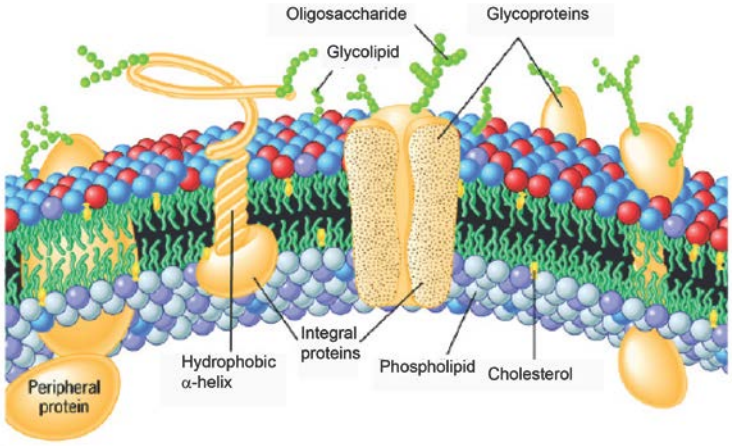

Fig. 1.1 *Sketch of a cell membrane, consisting of a lipid bilayer, membrane proteins, and carbohydrates decorating the surface [6].*

In the past decades, many studies demonstrated that Creutzfeldt-Jakob disease and bovine spongiform encephalitis are caused by abnormal interactions of prion proteins with cell membranes, while Parkinson and Alzheimer diseases by non-prion proteins [7]. In terms of

a structural point of view, both prion and non-prion proteins belong to a family of GPI-anchored proteins, whose C-terminal is connected to glycerophosphatidylinositols (GPIs) [8-10]. In contrast to transmembrane proteins spanning across lipid bilayers, GPI anchors are only integrated into the outer leaflet and thus more mobile than transmembrane proteins. Several studies reported that the lateral diffusion of membrane protein plays a major role in the development of prion based diseases [11-14]. For example, the modification of the GPI-anchor on prion glycoproteins with sialic acid allows the protein to be more mobile in the plane of the lipid bilayer [15].

GPI-anchored proteins are also known to play important roles in various cellular processes, such as membrane trafficking, cell signaling, and cell adhesion. In some lower eukaryotes, such as parasitic protozoa, GPI-anchored proteins are among the most abundant cell-surface proteins that are responsible for cell viability and defense against the host immune system [16]. One prominent example is *Trypanosoma brucei* a parasite that causes the sleeping sickness. The surface of trypanosome is coated with GPI-anchored proteins (Fig. 1.2), called variant surface glycoproteins (VSGs), which is responsible for the survival of the parasite in the bloodstream of the mammalians by three different mechanisms; (1) antigenic variation of VSG [17-18], (2) immune-suppression [19], and (3) clearance of surface-bound antibodies [20-22]. Recently, Engstler et al. suggested that the antibody clearance and sorting of antibody-VSG complex at the posterior cell pole requires forward cellular motility. Namely, the swimming of trypanosome causes directional movement of antibody-VSG complex in the plasma membrane [23].

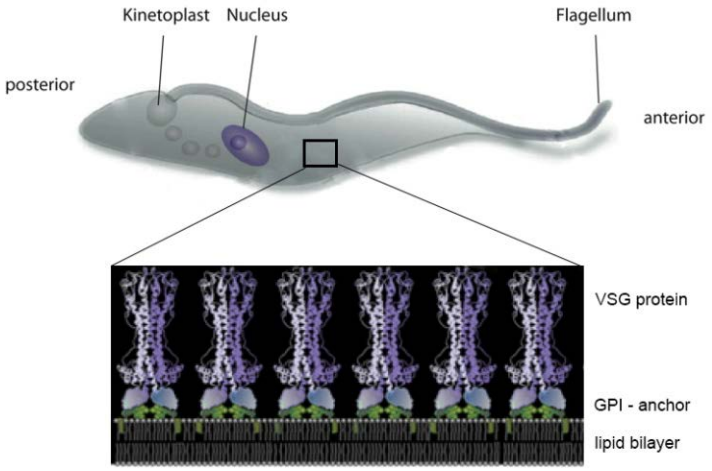

Fig. 1.2 *Schematic representation shows the Trypanosoma brucei and its cell surface which is dominated by a dense coat of VSG proteins (adapted from [23]).*

Although there have been many theoretical studies on the lateral diffusion of particles in crowded systems, experimental studies on the organization and the lateral diffusion of such highly concentrated GPI-anchored proteins on the membrane surface remains a challenge. From experimental viewpoints, it is technically difficult to incorporate/anchor high amounts of lipid-anchored proteins in cell membrane models.

Similar to the parasitic protozoa that displays a dense coat based on GPI-anchored proteins, gram negative bacteria display a dense layer of lipopolysaccharides (LPSs) at their outer surfaces (Fig. 1.3) [24]. The surface of one bacterial cell is coated with aproximately 3.5 millon LPS molecules [25-26]. LPS molecules protect themselves against changes in the surrounding environments and intruders, and stabilize their structural integrity. LPSs are also known as endotoxins since they induce a strong immune response by binding to the receptor complex that promotes the secretion of pro-inflammatory cytokines [27]. Despite the broad range of antibiotics which may kill bacteria, they also promote the release of LPSs in the circulation which in turns causes sepsis (blood poisoning) or septic shock, a severe infectious disease with high mortality [28]. For instance, there is an estimate of 150,000 death cases only for Germany based on data from critical care units [29]. However, a number of in vivo studies demonstrated that LPSs prevent the intrusion of cationic antimicrobial peptides (CAPs) into the cell membrane in the presence of divalent ions such as Ca^{2+} and Mg^{2+} ions [30-32].

Additionally, chelating agents such as ethylenediaminetetraacetate (EDTA) can remove these metal ions from the bacterial surface and increase the permeability of the membrane [33-34]. This suggests that for the design of peptide-based antibiotics one requires a better understanding about the electrostatics and their role in governing the interaction between LPSs and antimicrobial peptides at the molecular level.

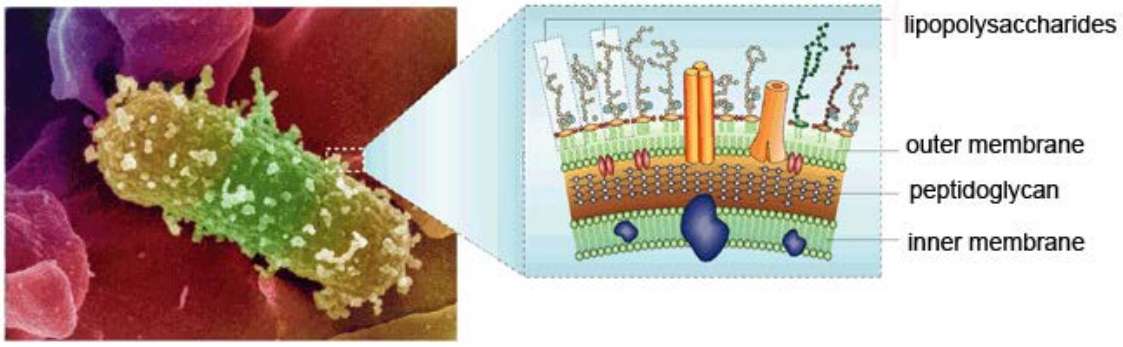

Fig. 1.3 *Electron micrograph of Escherichia coli (type of gram negative bacteria) with a schematic view showing the bacterial cell wall components (from [35]).*

Moreover, molecular dynamic simulations demonstrated that Ca^{2+} ions are essential for the stability and integrity of the LPSs outer bacterial membrane [36-37]. In addition, they reported that most of the Ca^{2+} ions are confined within a thin layer with thickness of ~ 2 nm in the negatively charged inner core of the LPSs [38] and a well-defined structural pattern existed for the location of the Ca^{2+} ions interacting with the phosphate groups adjacent to inner core saccharides [37-38]. Moreover, the divalent ions bridge the LPSs molecules leading to very low membrane permeability. For instance, the water molecules can penetrate the LPS membrane to a depth of ~ 3 nm [37]. Monte Carlo (MC) simulation of the number density distributions of ions and LPSs including protamine molecules has been carried out by Pink et al [39]. A “minimum model” of negatively charged wild type LPS strains was created in order to simulate the conformational changes of molecules on a more realistic time-scale up to milliseconds in a large simulation volume containing 100 PAO1 LPS molecules. The simulations predicted that protamine molecules are kept away from the LPS surface in the presence of divalent ions. However, although these simulations clarified the role of divalent ions in protecting the bacteria against chemical molecules, the structural evidence and the interaction mechanisms from the experimental approaches at the molecular level is still missing. Recently, Schenck et al. [40] utilized grazing incidence X-

ray fluorescence technique to reconstruct the density profiles of ions in the vicinity of LPS Re (possesses four negatively charged sugars) monolayer's. The results showed that divalent could replace the monovalent ions from the negatively charged sugars of LPS Re. Further work is still needed to investigate the interaction mechanisms between the bacterial membrane and antimicrobial or anti-sepsis peptides in the presence and absence of divalent ions.

In this study, planar model cell membranes, such as lipid monolayers at the air/water interface and solid supported lipid bilayer membranes at the solid/liquid interface, are utilized to study (I) the lateral diffusion and correlation of membrane-anchored proteins and (II) the interactions between antimicrobial peptides and bacterial membranes.

In chapter 4, the correlations between non-crystalline, membrane-anchored proteins were studied using grazing incidence small angle X-ray scattering (GISAXS). GISAXS has intensively been used to gain the structure and form factors of nano- to meso-scale objects (e.g. metal nano-particles [41-43], semiconductor quantum dots [44-47] and block copolymers [48-50]) in the vicinity of surfaces [51]. In this study, GISAXS was utilized for the first time to extract the inter-molecular separation distance and the range of the correlation of biological nano-particles (proteins) confined on the surface of fluid lipid membranes at the air-water interface (Fig. 1.4A). Furthermore, grazing incidence X-ray fluorescence (GIXF) was used in parallel to quantify the lateral density of proteins within the membrane through their S K_α fluorescence intensity for the first time (Fig. 1.4A). We demonstrated that the quantitative GIXF analysis requires X-ray reflectivity (XRR), since the electronic structures of ultrathin, stratified layer systems significantly influence the propagation (and thus illumination profiles) of electromagnetic waves.

In Chapter 5, the lateral diffusion of membrane-anchored proteins is determined as a function of proteins lateral density. For this purpose, two methods were employed to quantify the diffusion coefficient in different length scales: (1) Fluorescence recovery after photobleaching (FRAP) was used to estimate the average diffusion constant of an ensemble on micrometer length scale, and (2) The lateral diffusion of individual proteins on sub-micron length scale are studied by single particle tracking (SPT) microscopy (Fig. 1.4B). As a physical model of the surface of cells coated with densely packed, non-crystalline

proteins coupled to lipid anchors, we functionalized the surface of solid-supported membranes by coupling of neutravidin to biotinylated lipid anchors which allows one to control the inter-molecular distance with nanometer accuracy. In addition, as a representative model of GPI-anchored proteins, VSG proteins were incorporated in supported lipid membrane with different protein / lipid ratios that allows the control of proteins lateral density.

In chapter 6, the interaction mechanisms of cationic antimicrobial peptides are studied using the two complementary techniques; XRR and GIXF where the role of electrostatics and the influence of divalent ions on the interactions are discussed. A defined model of gram negative bacteria outer membrane was prepared form lipopolysacchrides (LPS Ra) monolayers at the air-water interface to investigate their interaction with natural and synthetic peptides. The fine structures perpendicular to the membrane plane and the ion distribution near the interface were determined by XRR and GIXF in the presence and absence of divalent cations.

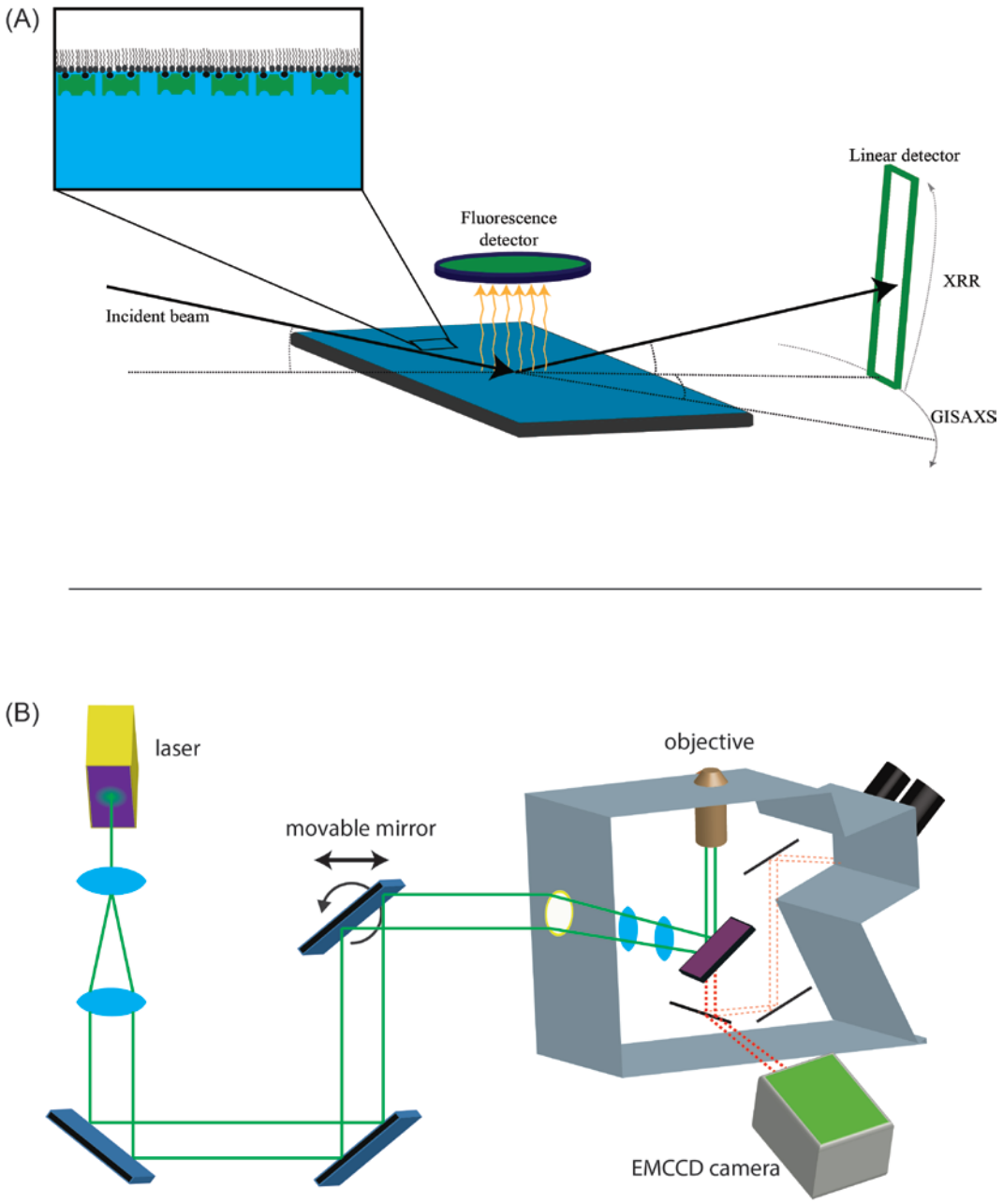

Fig. 1.4 *(A) The experimental setup and the scattering geometry used for GISAXS, XRR, and GIXF. (B) The experimental setup used for SPT measurements.*

2. Theoretical Background

2.1 Basic introduction

2.1.1 Self-assembly of membranes

When amphiphilic molecules such as lipids are dispersed in water they tend to self-assemble into micelles, bilayers or other forms. The driving force for the self-assembly in this case is the hydrophobic effect. This effect is originally an entropic effect arising from the hydrogen bonded structure of water. This can be understood in terms of the change in Gibbs free energy as:

$$\Delta G = \Delta H - T\Delta S \tag{2.1}$$

If one transfers one lipid molecule into water, a more ordered structure of water molecules around the hydrocarbon chains is formed (clathrate cage). This means that the entropy of transfer ΔS is always negative. The enthalpy of transfer is of less significance and can be either positive or negative [52]. Thus, the change in Gibbs free energy is always positive which means it costs energy to introduce a lipid molecule into water. To go into more details, the change in the free energy here is equivalent to the change in the chemical potential when one transfers a lipid molecule from a standard state $\mu_{HC,ref}$ (hydrocarbon chain in pure hydrocarbon environment) into water $\mu_{HC,w}$:

$$\mu_{HC,ref} - \mu_{HC,w} = RT \ln X_{HC,w} \tag{2.2}$$

where $X_{HC,w}$ is the mole fraction of the lipid in water. However, equation 2.2 tells us that the difference in chemical potential can be determined experimentally from the solubility of hydrocarbon chains in water. McAuliffe et al. has determined the solubility of a number of hydrocarbon molecules relevant to lipid bilayer and reported that the solubility of hydrocarbon chains in water decreases linearly with the chain length [53]. The determined energy cost found to be 6×10^{-21} J for additional methyl group in the hydrocarbon chain. This energy is about 20% of a hydrogen bond and arises because the new group will force more water molecules to lie in contact with the hydrocarbon chain.

However, from Gibbs phase rule, a lipid in water and a lipid in bilayer can be in equilibrium only at a fixed value of $X_{HC,w}$. This value called the critical aggregate concentration $X^{*}_{HC,w}$, rearrangement of equation 2.2 into a logarithmic form yields:

$$X^{*}_{HC,w} = X_{HC,l} e^{\left(\frac{\Delta\mu}{kT}\right)} \tag{2.3}$$

For lyso-DPPC (single chain lipid) this value is about 10^{-4} M and for double chain DPPC lipid it is about 10^{-12} M [54]. This small value indicates that at very low lipid concentrations, the lipids spontaneously start to form micelles.

2.1.2 Phase behavior of lipids

Fully hydrated lipid bilayers can undergo a well defined thermotropic phase transition in which the lipid chains change from ordered or gel-phase L_β to a fluid or liquid crystalline phase L_α. Additional intermediate phase P_β is found in the gel-phase of certain lipids in which the lipid bilayer is rippled [55]. The transition between the phases is a first order transition. Therefore the change in the Gibbs free energy must be zero at the phase transition (L_β to L_α) and equation 2.1 reads:

$$T_m = \Delta H \big/ \Delta S \tag{2.4}$$

T_m is the transition temperature which is also refers to the melting temperature of the hydrocarbon chains. However, as discussed in the previous section the change in entropy is proportional to the chain length. For instance, the incremental increase of the enthalpy and entropy with additional CH_2-group is 4.5 kJM^{-1} and 12 $JM^{-1}K^{-1}$ [54]. Therefore the melting temperature increases monotonically with the chain length.

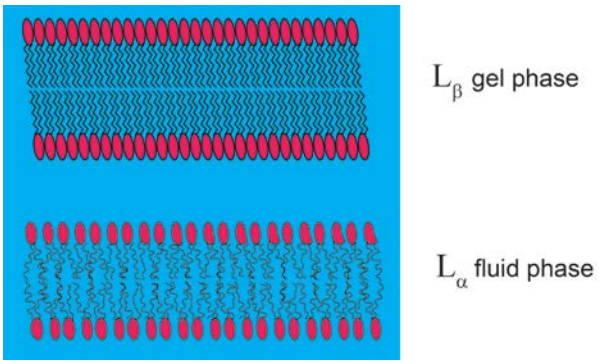

Fig. 2.1 *Representation of the thermotropic phases L_α (fluid phase) and L_β (gel phase). In the L_β phase the hydrocarbon chains are stretched and ordered. In the L_α phase the hydrocarbon chains are disordered.*

There are other factors that affect the transition temperature such as packing density of lipid molecules, non-saturated bond in the hydrocarbon chains, and surface charge [54-55]. For example the melting temperature of DPPC with saturated hydrocarbon chains is T_m = 41°C and T_m = 6 °C for SOPC with one unsaturated bond in the hydrocarbon chains.

2.1.3 Lateral diffusion

The cell membrane is considered to be a two dimensional matrix in which membrane proteins are embedded or anchored to the surface. Similar to the Brownian motion in three dimension, thermal energy induces the movement of lipids and proteins in the plane of the lipid bilayer i.e. lateral diffusion [56]. This can be rotational and translational diffusion, for biological membranes the translational diffusion is the most important. Therefore, the discussion is restricted here to the translational diffusion. However, in the following a brief review of some theories concerning the lateral diffusion is given.

2.1.3.1 Continuum hydrodynamic theory

Within the framework of the continuum approach, the bilayer is assumed to be two-dimensional continuum. The bilayer is treated as a viscous fluid sheet with a viscosity of η_{m} and a finite thickness of h surrounded by a fluid with much smaller viscosities η_1 and η_2 [57-61]. The diffusion coefficient is given by Einstein relation as

$$D = \frac{k_B T}{f} \tag{2.5}$$

where f is the friction coefficient. The task is to solve the Navier-Stockes equation for two-dimensional motion and derive an expression for the friction coefficient f that can be used in the Einstein relation for D. Saffman and Delbrück [57-58] treated the case $\eta_1 = \eta_2$, and gave an expression for the translational diffusion coefficient of a cylindrical particle (radius R_p) which is given as:

$$D = \frac{k_B T}{4\pi\eta_m h}\ln\left(\frac{\eta_m h}{\eta_w R_p} - \gamma\right). \tag{2.6}$$

η_w and η_m are the viscosities of medium (water) and membrane, h is the thickness of the membrane and hence the height of a particle, and γ is Euler's constant $\gamma = 0.5772$. Such a logarithmic law agrees well with previous experimental studies, suggesting relatively little dependence of D on the radius of transmembrane domain R_p [62-63].

For the translational diffusion of lipids and proteins in contact with viscous, asymmetric environments (e.g. glycocalyx and cytoskeleton), Evans and Sackmann modified the classical model by taking asymmetric boundary conditions into account [64]. In the modified model, the diffusion coefficient D as a function of the dimensionless particle radius of diffusing particle ε is given as:

$$D = \frac{k\ T}{4\pi\eta_m h}\left(\frac{1}{4}\varepsilon^2 + \frac{\varepsilon K_1(\varepsilon)}{K_0(\varepsilon)}\right)^{-1}. \tag{2.7}$$

K_0 and K_1 are modified zero and first orders Bessel functions of the second kind. Note, that ε can analytically be obtained from the dimensionless particle mobility $m = 4\pi\eta_m D/k_B T$, which can be determined from the diffusion coefficient D (Fig. 2.2). Here, the frictional coefficient b_s can be calculated by the membrane viscosity η_m, membrane thickness h, and the ratio between ε and R_p: $b_s = \eta_m h(\varepsilon/R_p)^2$ [65-66].

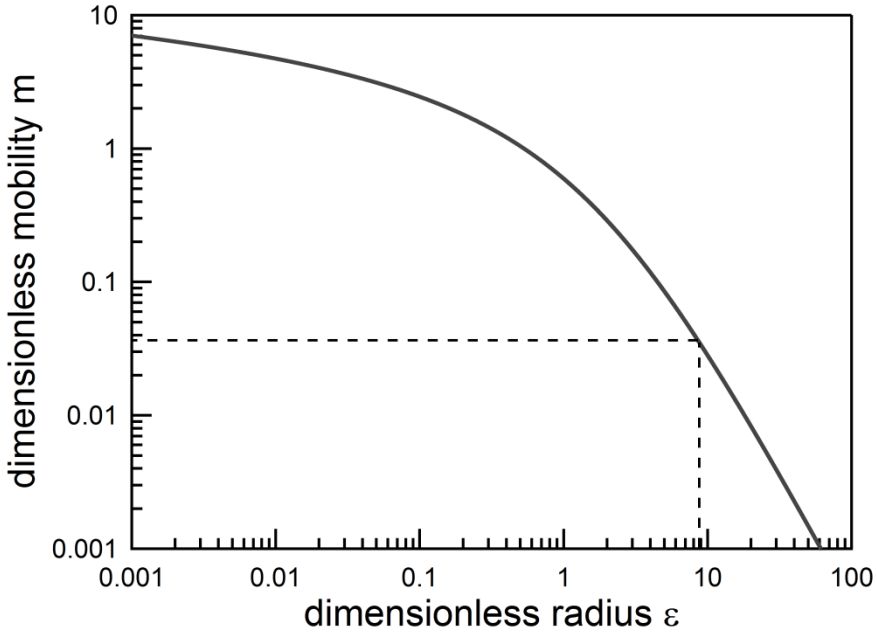

Fig. 2.2 *The dimensioless mobility m plotted as function of the dimensionless particle radius ε. From the experimental diffusion coefficient one calculates the dimensionless mobility in order to analytically determine the dimensioless particle radius (as indicated in dashed line).*

2.1.3.2 Theory of obstacled diffusion

In case membrane-associated proteins are expressed at a high surface density, the lateral diffusion of proteins is hindered by the presence of other proteins, which act as "obstacles". When the obstacles are immobile, the diffusion coefficient decreases linearly with the surface density, reaching to zero at a certain density threshold (percolation threshold). On the other hand, in the presence of mobile obstacles, that the diffusion coefficient can be related to a correlation function $f(c,\gamma)$ [67-70]:

$$f(c,\gamma) = \frac{-[(1-\gamma)(1-A)f_0+A]+\sqrt{[(1-\gamma)(1-A)f_0+A]^2+4\gamma(1-A)f_0^2}}{2\gamma(1-A)f_0}$$

$$f_0 = (1-\alpha)/(1+\alpha(2\gamma-1)). \qquad (2.8)$$

A is the area fraction of the obstacles and α a lattice-specific constant. γ is the ratio between the jump rate of a diffusing particle and the jump rate of obstacles, which indicates the fraction of immobile obstacles.

2.2 X-ray scattering

2.2.1 X-ray interaction with matter

X-ray radiation is part of the wide range electromagnetic spectrum which is a sort of energy which propagates as an oscillating electric and magnetic field. Therefore, when a beam of X-ray hits any type of matter the interaction is essentially between the electric field of the incident wave and the charges or between the magnetic field of the wave and the magnetic moments (spin). When a photon meets an atom, it can undergo one of the three events (Fig. 2.3); *elastic scattering* where the energy of the scattered photon remains unchanged, *inelastic scattering* where part of the energy is lost due to the collision with an electron (Compton scattering) or excitation of a vibrational state (Raman scattering) and eventually *absorption.* The later involves the photoelectric effect where the incident photon is absorbed by inner electron and leaves the atom with a vacancy that can be filled by another electron from the upper levels. This process is combined with an emission of X-ray fluorescent photon. However, the X-ray fluorescent photon can be reabsorbed in a secondary process by a valence electron causing the ejection of the electron from the atom (Auger electron).

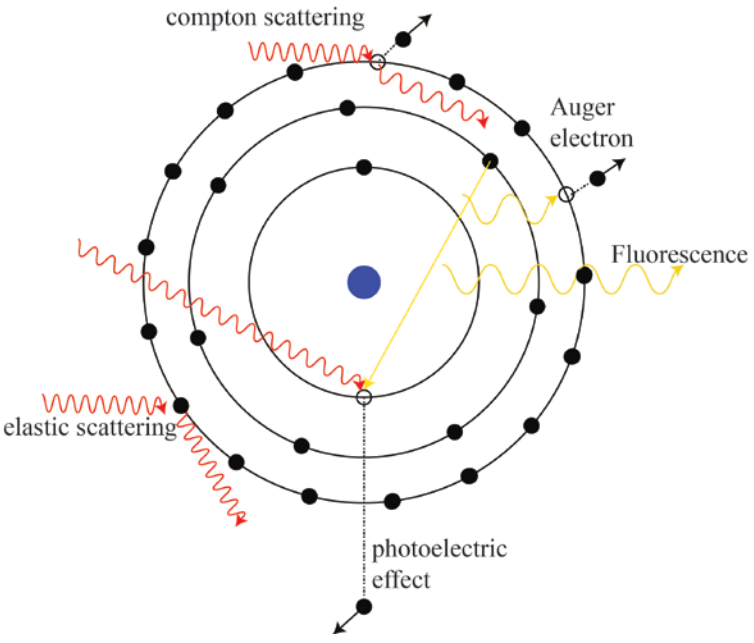

Fig. 2.3 *Illustration shows the main possible interactions between X-ray and an atom.*

The amplitude of the elastically scattered photons is inversely proportional to the mass. Thus, electrons are the main contributors in the scattering since the mass of the electron is 1836 times smaller than the mass of the proton. Indeed, the scattering amplitude depends on the number of electrons per atom and thereby the atom type. Besides, the far-field amplitude where constructive and destructive interference takes place depends on the relative positions of the scatters. Consequently, the elastic scattering provides information about the structure and the arrangement of atoms within the sample while the inelastic scattering provides information about the movements of the atoms (vibrations). Eventually, the absorption is usually used to study the fine structure, type and the environment of the atoms.

2.1.2 Basics of X-ray scattering

In X-ray scattering experiments, X-rays are elastically scattered by the individual electrons within the atoms. If there is no change in phase between the incident ray and the scattered one and the only phase difference is due to the path length difference, then the scattering is said to be coherent. With this condition the scattered rays are the sum of waves scattered by individual electrons within the sample. A simple scattering problem from a single electron (Thomson scattering) can be treated classical point of view.

Assume a plane wave polarized in the z-axis which travels in the x-direction and hits a single static electron located at the origin. The polarization here is defined in the direction of the electric field (Fig 2.4).

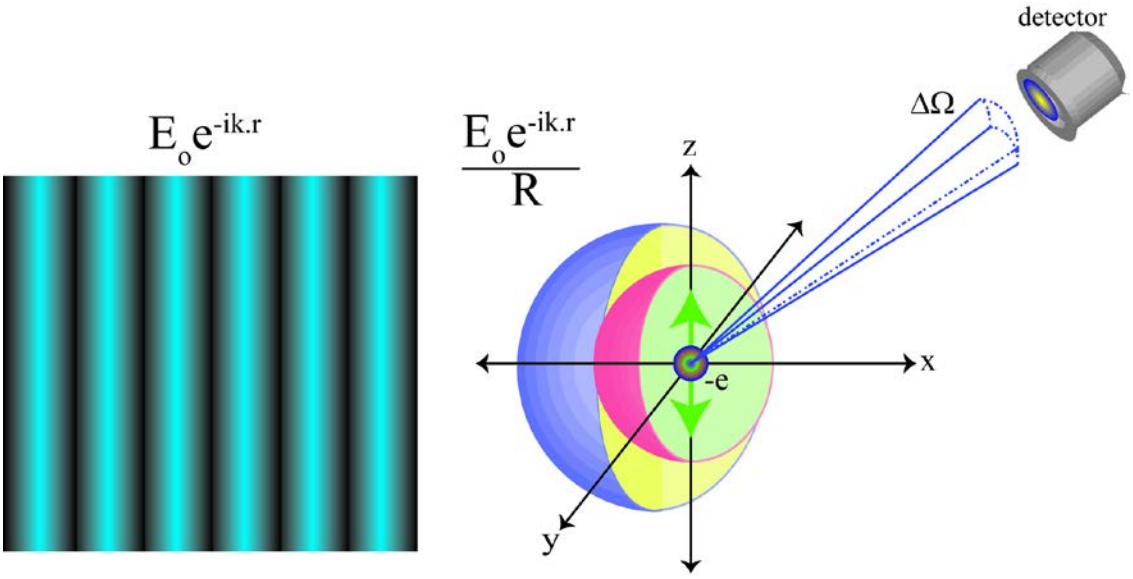

Fig. 2.4 *Thomson scattering; a plane wave hits an electron and scatters spherically. The scattered intensity is measured by a movable point detector.*

The electron oscillates in the z-direction due to the force exerted by the oscillating electric field as:

$$m\ddot{z} = -e\, E_{in} \tag{2.9}$$

The small amplitude oscillations of the electron lead to a localized current which in turn emits a radiation. The resulting scattered amplitude is a spherical wave and can be represented as:

$$E_{sc} = E_{in}\, b\, \frac{e^{ik.r}}{R} \tag{2.10}$$

where b is the scattering length. For a single electron b is equal to r_e = 2.818×10^{-5} Å where r_e is the classical radius of the electron (Thomson radius). If one integrates the scattered intensity $|E_{SC}|^2$ over all directions, one gets the scattering cross section $\sigma = 8\pi r_e^2/3$ = 0.665 barn (1 barn = 10^{-28} m^2). Experimentally, the scattered intensity is measured by a detector within a solid angle $d\Omega$. Therefore, what one practically records is $\frac{d\sigma}{d\Omega}$ i.e. the differential scattering cross section. However, in any scattering experiment with certain geometry, the task is to find a proper theoretical expression for this quantity. Note that b is a measure for the scattering power.

In the case of electrons are bound to nucleus i.e. an atom. The electrons are considered to scatter independently and the scattered amplitudes can be added coherently. What one should consider is the positions of the electrons within the electron cloud and consequently the interference effects. A simple treatment of this problem is derived within the Born approximation in which the total scattering length can be written as $b = r_e . f(q)$ where $f(q)$ is the atomic form factor and it is nothing but the Fourier transform of the electron density $f(q) = \mathrm{F}(\rho(\mathrm{r}))$ where q is the momentum transfer. By introducing a spring constant κ for the binding of the electron to the nucleus and a damping coefficient due the surrounding electrons γ equation 2.9 can be rewritten as:

$$m\ddot{z} + \gamma \dot{z} + \kappa z = -e\ E_{in} \tag{2.11}$$

Solving this differential equation, leads one to write the scattering length as

$$b = r_e(f + f' + if'') . \tag{2.12}$$

The last two terms represent a correction for the anomalous scattering. The first term f is slightly dependent on the momentum transfer q and at q = 0 it is equal to the atomic number Z. f' is a correction to the real part which is wavelength dependent. The term f'' accounts for the absorption and it is also wavelength dependent.

2.2.3 Refractive index

The oscillations of the electron within an atom due to incident X-ray photon alter the polarization of the atom as $P = \rho_e e z$ where ρ_e is the electron density. From electrostatics, the dielectric polarizibility is proportional to the applied electric field ($P = \varepsilon_0 \chi E$) where χ is the dielectric susceptibility. Thus, solving equation 2.11 for z enables one to derive an expression for the dielectric susceptibility:

$$\chi = \frac{\rho_e e^2 E}{\varepsilon_0 m \omega^2} \tag{2.13}$$

The refractive index is defined through the dielectric susceptibility as $n = \sqrt{1+\chi}$. Since χ is smaller than one, then the refractive index can be written as:

$$n = 1 - \frac{\lambda^2 r_e \rho_e}{2\pi}. \tag{2.14}$$

In this case, the absorption is not taken into account. The connection between the electron density and the scattering length density (SLD) can be seen from equation 2.12. If one divides *b* by the unit cell volume, then the refractive index can be written as:

$$n = 1 - \delta + i\beta$$

$$\text{with } \delta = \frac{\lambda^2 r_e \rho_e}{2\pi} = \frac{\lambda^2 SLD}{2\pi} \text{ and } \beta = \frac{\lambda\mu}{2\pi} \tag{2.15}$$

where δ and β are the real and the imaginary part of the refractive index, respectively. μ is the linear absorption coefficient. For example, for water (H_2O) one can estimate the electron density and the SLD from its mass density (1 g/ml) that corresponds to molecular volume of 29.9 $Å^3$ per one H_2O molecule. Therefore, the electron density of water can be determined to be 0.335 è/$Å^3$. Note, that the SLD is related to the electron density by the classical radius of the electron ($SLD_{water} = 9.45\times10^{-6}$ $Å^{-2}$). In general, δ for most material lies in the order of 10^{-5} and $\beta \sim 10^{-8}$. Therefore, the refractive index in X-ray region is slightly less than one for any material and it is equal to unity in vacuum or air. Note that the speed of light inside the matter is c_o/n which is larger than the speed of light in vacuum in this case. However, one has to keep in mind that this is the phase velocity (ω/k) and the group velocity ($d\omega/dk$) which carries the information is indeed smaller than the speed of light in vacuum.

2.3 Specular X-ray reflectivity

2.3.1 Reflection from a single smooth interface

Consider an incident plane wave impinging at a smooth interface between two mediums with refractive indices of n_1 and n_2 as illustrated in Fig. 2.5. The incident beam can be

reflected from the interface back to medium 0 with an exit angle of $\alpha_f = \alpha_i$ and can be refracted in medium 1 with an angle α_t. The refraction is described by Snell´s law as:

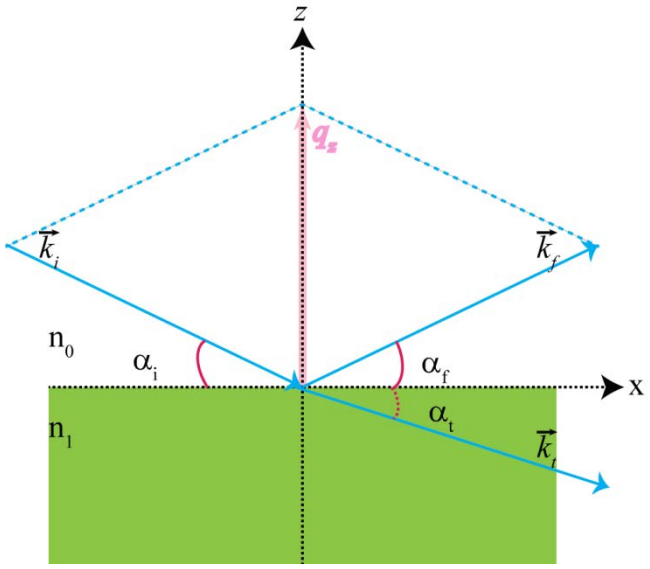

Fig. 2.5 *Reflection and refraction of a wave traveling in the x-z plane.*

$$n_0 \cos\alpha_i = n_1 \cos\alpha_t \tag{2.16}$$

If $n_1 < n_0$ then the refracted beam moves away from the surface normal ($\alpha_t < \alpha_i$). Therefore, by lowering the angle of incidence, the refracted beam becomes closer to the interface. At a certain value of α_i where $\alpha_t = 0$, the wave is totally reflected into medium 0. At this condition, the angle of incidence is called the critical angle α_c. Below α_c the incident beam experiences a total external reflection. From equations 2.5 and 2.4 one can deduce an expression for the critical angle,

$$\alpha_c \approx \sqrt{\frac{2(\delta_2 - \delta_1)}{1-\delta_1}} \approx \left(\frac{\lambda^2 r_e}{\pi}\right)^{\frac{1}{2}} \sqrt{\rho_{e2} - \rho_{e1}} \tag{2.17}$$

Equation 2.17 implies that the critical angle of total external reflection is proportional to the electron density difference between the two mediums (contrast). If medium 0 corresponds to air, then $\alpha_c \approx \sqrt{2\delta_2}$ which lies in the range of milli-radian for most

materials. For example, for silicon with electron density of $\rho_e = 0.71$ e/Å^3 and an incident wave possessing a wavelength of one angstrom the critical angle is $\alpha_c = 0.145°$.

To derive a formula for the reflectivity from the interface one starts from the Helmholtz equation that describes the propagation of waves in a medium with a certain dielectric constant i.e index of refraction as:

$$\left[\nabla^2 + k_0^2 n^2(r)\right] E(r) = 0 \tag{2.18}$$

The solution for a wave impinging at an interface between two mediums is again a plane wave

$$E_j = A_j e^{i(\omega t - k_j . r)} \tag{2.19}$$

where *A* the amplitude and *j* can take i, f and t which refer to the incident, reflected and transmitted waves, respectively.

From the continuity of the electric field and the magnetic field (hence, the first derivative of the electric field) at the interface where z = 0, one can easily show that the amplitudes of the electric field are given by:

$$A_i + A_f = A_t \text{ and } A_i \vec{k}_i + A_f \vec{k}_f = A_t \vec{k}_t \tag{2.20}$$

The reflection coefficient $r_{0,1}$ is defined as the ratio between the reflected amplitude and the incident amplitude ($r_{0,1} = A_f / A_i$) and in the same manner one can define the transmittance coefficient as $t_{0,1} = A_t / A_i$. Using equation 2.20 and the fact that the components of the wave vectors are given by $k_{zj} = k_o n_j \sin\alpha_j$ then we can write:

$$r_{0,1}^F = \frac{k_{iz} - k_{fz}}{k_{iz} + k_{fz}} \ , \ t_{0,1}^F = \frac{2k_{fz}}{k_{iz} + k_{fz}} \tag{2.21}$$

Equation 2.21 is called Fresnel equation. The reflectivity (*R*) from the interface is given by the square modulus of $r_{0,1}$. Note that the polarization of the waves is not taken into account since both polarizations (i.e transverse and perpendicular) lead to the same result

in the X-ray spectrum contrary to the visible region. The reflectivity is usually plotted against the incidence angle or the momentum transfer perpendicular to the sample surface q_z. Therefore, one can write the reflectivity in terms of q_z as,

$$R^F(q_z) = \left| \frac{q_z - \sqrt{q_z^2 - q_c^2}}{q_z + \sqrt{q_z^2 - q_c^2}} \right|^2 \tag{2.22}$$

where q_z from the geometrical consideration is given by

$$q_z = \frac{4\pi}{\lambda} \sin \alpha_i \tag{2.23}$$

When the momentum transfer is very large compared to q_c, then the use of power series expansion, equation 2.22 can be approximated to

$$R^F(q_z) = \frac{q_c^4}{16 q_z^4} \tag{2.24}$$

Some general remarks about Reflectivity can be drawn from equations 2.22 and 2.23. Above q_c the reflectivity exhibits a very steep decrease. Below q_c there is a plateau of total external reflection. Additionally, the reflectivity drops by $1/q_z^4$ power law when $q_z > 3q_c$ as it can be seen in Fig. 2.6.

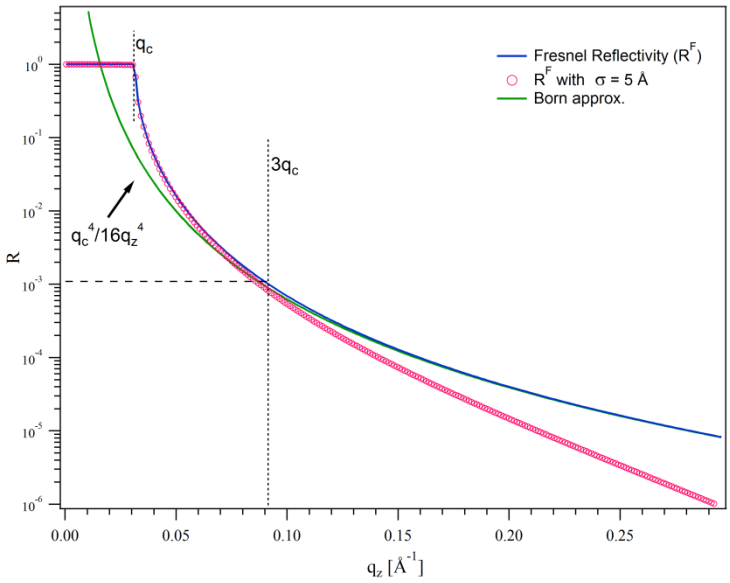

Fig. 2.6 *Simulated intensity of Fresnel reflectivity from air-silicon interface is indicated in blue line (according to eq. 2.22). The green line shows the* $1/q_z^4$ *power law.*

2.3.2 The Born approximation

In the previous sub-sections we considered the reflectivity without any reference to scattering. Basically, reflectivity is a result of scattering from individual particles (electrons or nuclei, in the case of X-ray or Neutron, respectively) followed by interference between the scattered rays. Within the Born approximation, the incident beam intensity is assumed to be unperturbed. Therefore, the scattered intensity within this approximation is nothing but the Fourier transformation of the electron density distribution F(ρ(r)) in the material or the sample (sub-section 2.2.2). In reflectivity measurement one probes the vertical variation of the electron density for a given sample (lets this be the z-axis), so one can represent the electron density as $\rho(r) = X(x)Y(y)\rho(z)$, where X and Y stands for the shape of the illuminated sample area. From geometrical consideration it is straightforward to show that the scattered intensity i.e the reflectivity can be given as

$$R(q_z) = \frac{16\pi^2 r_e^2}{q_z^4}\left|\mathcal{F}\left\{\frac{d\rho(z)}{dz}\right\}\right|^2 = \frac{R^F(q_z)}{\rho_s^2}\left|\mathcal{F}\left\{\frac{d\rho(z)}{dz}\right\}\right|^2 \qquad (2.25)$$

Equation 2.25 is the so called master formula; it shows that the ratio between actual reflectivity and the reflectivity from ideal interface is the absolute square of the Fourier

transformation of the electron density gradient across the sample surface normalized to the substrate electron density. For smooth interface between two mediums equation 2.25 is reduced to equation 2.24. However, as it could be seen in Fig. 2.6 the limit of the Born approximation is indicated by the dashed lines. The Born approximation is invalid in the vicinity of the critical angle where multiple reflections and refractions become significant. It should be noted that despite of these constraints, the Born approximation is the common used model for interpreting most of the scattering experiments.

2.3.3 Rough interface

There are many aspects to describe the rough interfaces with statistical distributions [71-73]. For simplicity, it is more convenient to introduce the effect of roughness on the Fresnel reflectivity within the Born approximation. To do that, the electron density is smeared out by a function to account for the diffusiveness of the interface. The frequently used function is the error function whose first derivative is Gaussian function. Implementing this into equation 2.25 and the fact that the Fourier transform of a Gaussian is again a Gaussian then it follows that the reflectivity from a rough interface is modified to:

$$R(q_z) = R^F(q_z) \cdot e^{-q_z^2 \sigma^2} \tag{2.26}$$

Where σ characterizes the width of the gradual interface and refers to the mean square roughness. The exponential term is known as the Crose-Nèvot factor [74] which indicates that the reflectivity of rough interface falls off more rapidly than for a sharp interface (see Fig. 2.6, open circles).

2.3.4 Reflectivity from stratified layers

Parratt´s recursive method [75] is the most widely used method in calculating reflectivity from stratified layers which is identical to the so called Abelès matrix method [76]. Both methods emerge from the dynamical theory and they represent the exact solution of the problem. In these methods, the films are described by slabs, each with a thickness of homogenous electron density. Here, we discuss the matrix method and one can refer to some text books [77] for a detailed discussion about Parratt´s recursive method. Assume

N-layers between two homogenous bulk mediums as illustrated in Fig. 2.7. Abelès showed that the relation among the incident electric field E_0^+, reflected E_0^- and transmitted E_{N+1}^- amplitudes is given as:

$$\begin{pmatrix} E_0^+ \\ E_0^- \end{pmatrix} = \frac{C_1 C_2 ... C_{N+1}}{t_1^F t_2^F ... t_{N+1}^F} \begin{pmatrix} E_{N+1}^+ \\ 0 \end{pmatrix} \tag{2.27}$$

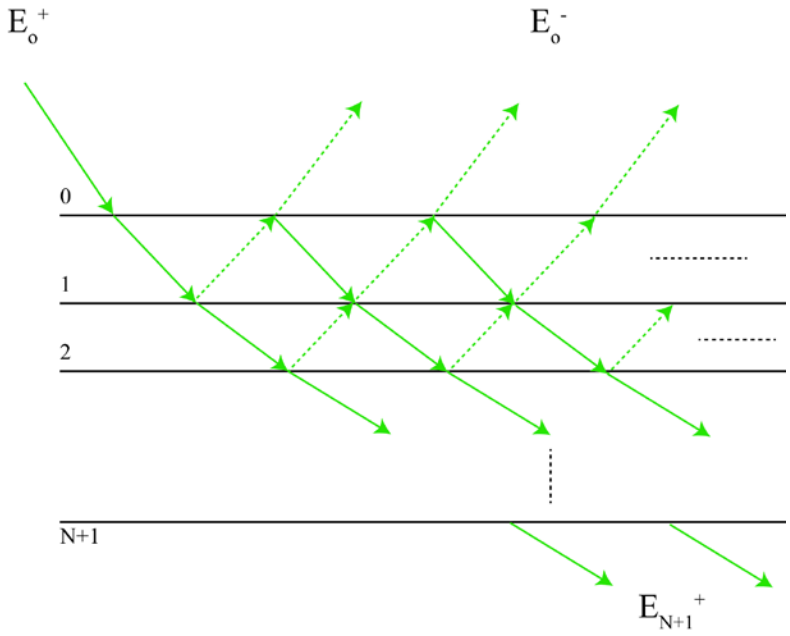

Fig. 2.7 *Illustration showing the multiple reflections and refractions at interfaces of stratified thin films.*

where, C_{j+1} is the propagation matrix expressed as

$$C_{j+1} = \begin{pmatrix} \exp(-ik_{zj}.d_j) & r_{j-1}\exp(-ik_{zj}.d_j) \\ r_{j-1}\exp(ik_{zj}.d_j) & \exp(ik_{zj}.d_j) \end{pmatrix}, \tag{2.28}$$

t_j^F is the Fresnel transmission coefficient, and r_j is the Fresnel reflection coefficient. Since the propagation matrices can be re-written as

$$C_1 C_2 ... C_{N+1} = \begin{pmatrix} a & b \\ c & d \end{pmatrix} \tag{2.29}$$

Then the Reflectivity can be expressed

$$R = |r|^2 = \left| \frac{E_0^-}{E_0^+} \right|^2 = \left| \frac{c}{a} \right|^2 \tag{2.30}$$

Fig. 2.8 shows a simulation for a polymer film deposited into Si-substrate with a thickness of d = 200 Å assuming interfacial roughness of $\sigma_{0,1}$ = 5 Å, $\sigma_{1,2}$ = 3 Å (green curve) or $\sigma_{0,1} = \sigma_{1,2}$ = 0 Å (red curve). From the features of the reflectivity curve one can directly conclude some structural parameters. For instance, the reflectivity curve exhibits oscillations due to the constructive and destructive interference between the reflected rays from the two interfaces. These oscillations are called Kiessig fringes that can be used directly to estimate the thickness of the film $d = 2\pi / \Delta q_z$. In addition, the amplitude difference between the maxima and minima reflects the difference in the electron density between the film and the substrate i.e the contrast. Moreover, the roughness affects the curve at high q_z values by two ways; first, the intensity decay more rapidly than that of a Fresnel reflection, and second, the oscillation diminishes similar to that of a damped oscillator (Fig. 2.8). Note, that the maximum accessible q_z-range determines the minimum film thickness which can be resolved by XRR ($d_{min} \sim \pi / q_{z\text{-}max}$). Practically, the main parameters which define the reachable $q_{z\text{-}max}$ are the level of the background and the flux of the incident beam.

Irrespective of the qualitative structural features that can be concluded from the reflectivity curve, for a quantitative analysis of the reflectivity data one has to refine the experimental data with a proper model which describe the real system especially those composed of many layers. A common way is to represent each layer with a slab of homogenous electron density ρ_j, thickness d_j and roughness σ_j. The condition $\sigma_j < d_j$ "small roughness" must be fulfilled in order to guarantee that the values of the refractive index n_j and n_{j+1} for layers j and j+1 reached within these layers. Otherwise, the system cannot be treated as N-independent layers.

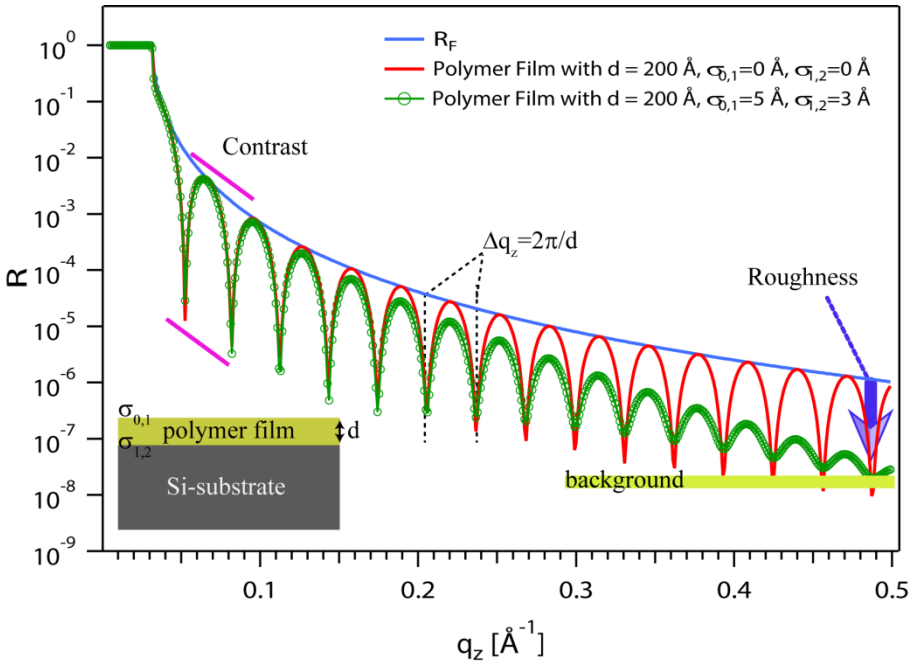

Fig. 2.8 *Simulated XRR of a polymer film deposited onto Si-substrate with a thickness of 200 Å assuming no interfacial roughness (red curve) and by assuming a rough interfaces with $\sigma_{0,1}$ = 5 A and $\sigma_{1,2}$ = 3 A (green). The blue line represents the Fresnel reflectivity. The blue arrow indicates the effect of surface roughness on the reflectivity curves.*

Nevertheless, it is possible to use the Abelès matrix or the Parratt formula to calculate the reflectivity for any system even when the condition $\sigma_j < d_j$ is not fulfilled. The system can be divided into equally thick slices approximately 1 Å. And the starting point is the total film thickness which can be estimated easily from the Fourier transform of the reflectivity curve. The parameters to be refined are the electronic density of each slice and eventually one overall roughness parameter describing the total effective interfacial roughness.

2.4 Grazing incidence small angle X-ray scattering

In this section we will deal with diffuse scattering in a special case where the incident angle occurs in the vicinity of the critical angle. Within this region the effect of multiple reflection and refraction cannot be neglected and the use of the Born approximation (BA) fails. However, in the case of GISAXS experiments, better results are obtained with the semi-dynamical treatment of the scattering within the distorted wave Born approximation

(DWBA). DWBA is a first order perturbation theory that relies on a defined reference state (e.g reference wavefields for flat surfaces) and a perturbation potential caused by the particle [78-81].

2.4.1 Form factor in the DWBA (dilute case)

To understand how one can construct the scattering cross section within this approximation, consider a simple example of randomly distributed particles with shape $S(\mathbf{r})$ and index of refraction n_p on an infinite smooth substrate [78]. The starting point is the solution of the Helmholtz propagation equation (equation 2.6) for smooth flat surface. This can be represented by reflected and refracted plane waves as,

$$E_0(\mathbf{r},\mathbf{k}) = E_0\, \mathrm{e}^{-ik_{\|}.r_{\|}} \begin{cases} \mathrm{e}^{-ik_{z,0}z} + r_{0,1}\, \mathrm{e}^{-ik_{z,0}z} ; & z > 0 \\ t_{0,1}\, \mathrm{e}^{-ik_{z,1}z} ; & z < 0 \end{cases} \tag{2.31}$$

where $k_{||}$ and $k_{z,0/1}$ are the wavevectors parallel and perpendicular to the surface, respectively. The Fresnel coefficients of reflection $r_{0,1}$ or transmission $t_{0,1}$ are given by equation 2.21. To work out the perturbation theory, the refractive index in eq. 2.6 is decomposed to

$$n^2(\mathbf{r}) = n_0^2(z) + \delta n^2(\mathbf{r}) = n_0^2(z) + (n_p^2 - 1)S(\mathbf{r}) \tag{2.32}$$

$n_0^2(z)$ is the index of refraction of the unperturbed system. $\delta n^2(\mathbf{r})$ is the perturbation induced by the particle of refraction index n_p and shape $S(\mathbf{r})$. The value of $S(\mathbf{r})$ is one inside the particle and zero outside. The scattering cross section in this case reads,

$$\frac{d\sigma}{d\Omega} = \frac{k_0^2}{16\pi^2 E_0^2} \times \left| \int \mathrm{d}\mathbf{r}' E_0(\mathbf{r}', \mathbf{k}_\mathrm{i}) \delta n^2(\mathbf{r}) E_0(\mathbf{r}', -\mathbf{k}_\mathrm{f}) \right|^2 \tag{2.33}$$

Carrying out the integral using the expression for the reference wave filed given in equation 2.31 produces

$$\frac{d\sigma}{d\Omega} = \left(\frac{d\sigma}{d\Omega}\right)_{specular} + \left(\frac{d\sigma}{d\Omega}\right)_{diffuse} \tag{2.34}$$

and the diffuse differential cross section is given by

$$\left(\frac{d\sigma}{d\Omega}\right)_{diffuse} = \frac{k_0^2}{16\pi^2}\left|n_p^2 - 1\right|^2 \left|\mathcal{F}(\mathbf{q}_{\|}, \mathrm{k_{zi}}, \mathrm{k_{zf}})\right|^2 \tag{2.35}$$

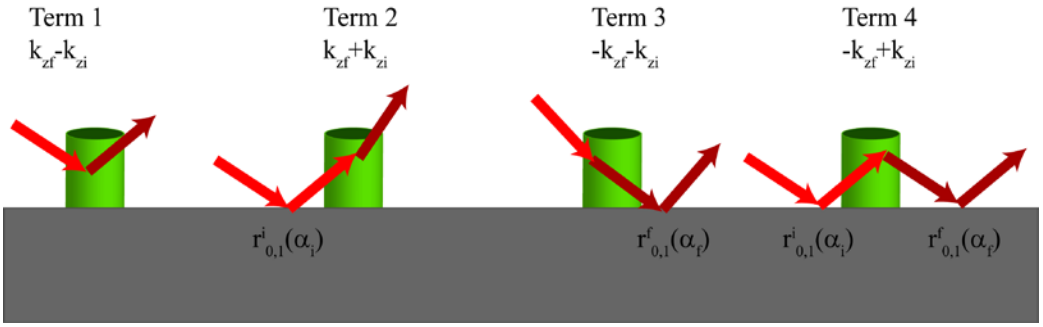

Fig. 2.9 *Schematic of particles on a substrate and the four scattering events with their vertical wavevector transfers within the DWBA.*

Where F is the form factor of the nanoparticle in the DWBA expressed as

$$\begin{aligned}\mathcal{F}(\mathbf{q}_{\|}, \mathrm{k_{zi}}, \mathrm{k_{zf}}) = \mathrm{F}(\mathbf{q}_{\|}, \mathrm{k_{zf}} - \mathrm{k_{zi}}) + r^i_{0,1}\mathrm{F}(\mathbf{q}_{\|}, \mathrm{k_{zf}} + \mathrm{k_{zi}}) + r^f_{0,1}\mathrm{F}(\mathbf{q}_{\|}, -\mathrm{k_{zf}} - \mathrm{k_{zi}}) \\ + r^i_{0,1} r^f_{0,1}\mathrm{F}(\mathbf{q}_{\|}, -\mathrm{k_{zf}} + \mathrm{k_{zi}})\end{aligned} \tag{2.36}$$

Note that the perpendicular momentum transfer can take the values $q_z = \pm \mathrm{k_{zf}} \pm \mathrm{k_{zi}}$. The parallel momentum transfer can be approximated as $|\mathbf{q}_{\|}| = \sqrt{q_y^2 + q_x^2} \cong q_y$ since q_x is very small. F is the Fourier transform of the particle shape given by (see Appendix A.1):

$$\mathrm{F}(\mathbf{q}_{\|}, \mathrm{q_z}) = \int \mathrm{S}(\mathbf{r})\, \mathrm{e}^{-\mathrm{i}\mathbf{q}_{\|}\mathbf{r}_{\|} - \mathrm{i}q_z z}\, \mathrm{d}^3\mathbf{r} \tag{2.37}$$

Fig. 2.9 shows a diagrammatic interpretation of the four terms in equation 2.23 as calculated in the DWBA. These terms represent four possible scattering events on the particle. The first term is the Born term which is a scattering of the incident wave by the particle. The other terms involve reflections of the incident, scattered or both waves from the substrate. Each form factor with an effective momentum transfer ($q_z = \pm \mathrm{k_{zf}} \pm \mathrm{k_{zi}}$) is weighted by the Fresnel reflection coefficients in the incidence or in emergence as depicted in Fig. 2.9. The Fresnel reflectivity drops as $1/q^4$, at well above the critical angle

the first term becomes dominant and the contribution of the other three terms can be neglected i.e the BA becomes valid.

Fig. 2.10 shows a simulated GISXAS intensity in BA (green curves) and DWBA (red curves) for a cylindrical particle on a Si-substrate with a scattering length density of SLD = 12.2×10^{-6} $Å^{-2}$. Along the perpendicular component of the momentum transfer (Fig. 2.10, left panel) the calculated GISAXS intensity in the DWBA does not exhibit sharp minima as those calculated in the BA. This is due to the coherent interference between the four terms of the form factor within the DWBA (equation 2.36). In addition, the position of the minima in DWBA is shifted to higher q_z value in comparison to those calculated in BA. Moreover, the variation of the amplitude and phase of the Fresnel coefficients in equation 2.36 close to the critical angle of total external reflection leads to an enhancement of the scattered intensity known as the Yoneda peak [82].

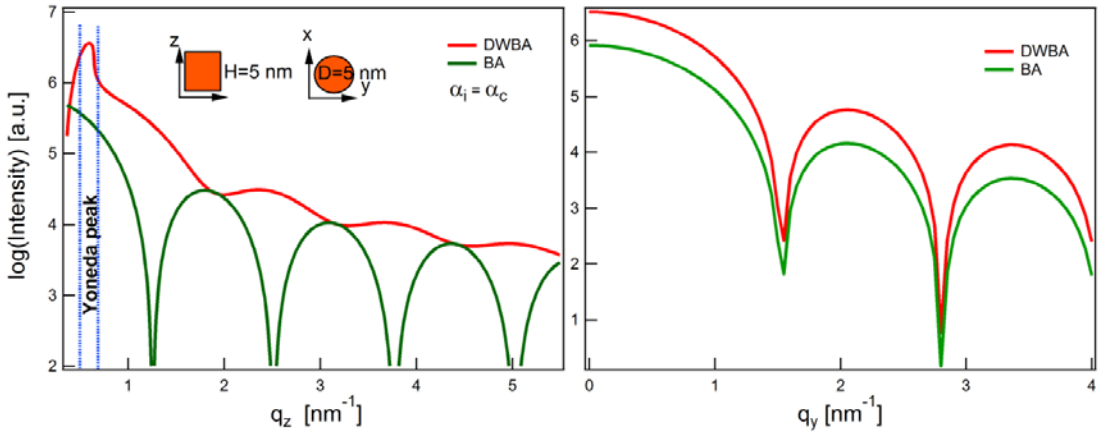

Fig. 2.10 *Simulated GISAXS intensity of randomly distributed cylindrical particles on a substrate with random organization at incident angle equal to the critical angle.(Left) GISAXS intensity as a function of q_z at q_y =0. (Right) GISAXS intensity as a function of q_y at q_z =0.5 nm^{-1}.*

In the dilute case where the particles are randomly distributed onto the substrate, GISAXS signals provide information only about the form factor. The scattered intensity in the parallel direction within the DWBA and BA in this case is similar (Fig. 2.10, right). This enables one to carry out easy estimation about the shape and the average size in the z-direction assuming a monodispersive or a small polydispersive system. If we represent the average radius of the particle in the parallel direction over its height in the z-axis by

$< R >_z$ by plotting the square modulus of the form factor against $q_y < R >_z$, one can deduce a rough estimation about the size and shape of a particle from the position of the first minima. For instance, if the minimum occurs at $q_y < R >_z \approx 3.9$ this indicates isotropic particles like a cylinder or sphere based shapes. For a pyramid based shapes with the beam aligned along a face or an edge their first minima appears at $q_y < R >_z \approx 3.3$ or 4.5, respectively [51].

A treatment of GISAXS signal from particles buried in a substrate or imbedded in thin layer on a substrate etc. can be handled in a similar way, with the only difference is the transmitted waves should be involved. The Fresnel wavefield that represents the reference state is given by a set of upward and downward propagating waves which can be evaluated using the matrix formalism (see equation 2.48).

Moreover, using the same approach for the form factor based on some shapes, the form factor of a core-shell particle can be easily constructed. This case is interesting for its applications in biomolecules which mostly exhibits a hydration shell. The perturbation term induced by the core-shell particle can be written as:

$$\delta n^2(\mathbf{r}) = \delta n_{co}^2 S_{co}(\mathbf{r}) + \delta n_{sh}^2 \left\{ S_{sh}(\mathbf{r}) - S_{co}(\mathbf{r}) \right\} \tag{2.38}$$

Where the perturbation of the particle core or the particle shell is given as $\delta n_{co}^2 = n_{co}^2 - n_m^2$, $\delta n_{sh}^2 = n_{sh}^2 - n_m^2$, respectively. n_m represents the refractive index of surrounding environment of the particle. The deduced expression of the form factor in the DWBA formalism of such perturbation can be written as an effective form factor with the following form:

$$\mathcal{F}(\mathbf{q}_{\|}, \mathrm{k_{zi}}, \mathrm{k_{zf}}) = \mathcal{F}_{co}(\mathbf{q}_{\|}, \mathrm{k_{zf}} - \mathrm{k_{zi}}) + \eta \left[\mathcal{F}_{sh}(\mathbf{q}_{\|}, \mathrm{k_{zf}} - \mathrm{k_{zi}}) - \mathcal{F}_{co}(\mathbf{q}_{\|}, \mathrm{k_{zf}} - \mathrm{k_{zi}}) \right] \tag{2.39}$$

With $\eta = \delta n_{sh}^2 / \delta n_{co}^2$ reflects the contrast between core and shell.

2.4.2 Structure factor (Concentrated case)

In the previous section we dealt with one particle or multiple particles are randomly distributed on a flat substrate. When the particles concentration increases, two phenomena should be taken into account; (1) the interference of the scattered X-rays from different particles which depends on their spatial organization, their size and shape distribution and on the coupling between both, (2) at very small incident angles the scattered wave from a particle can be scattered again by another particle. The later can be dropped out in the case of particles in two dimensions. This leads to a simple hypothesis of additivity in the perturbation term which allows us to write the differential cross section as sum of the form factors of individual particles as

$$\left(\frac{d\sigma}{d\Omega}\right)_{diffuse} = \frac{k_0^2}{16\pi^2}\left|\delta n_C^2\right|^2 \left|\sum_{i=1}^{N} \mathcal{F}_i(\mathbf{q}_{\|}, \mathrm{k_{zi}}, \mathrm{k_{zf}})\, \mathrm{e}^{-\mathrm{i}q_{\|}r_{\|i}}\right|^2 \tag{2.40}$$

where δn_C^2 is the contrast between a particle and its surrounding. Note that the summation is running over the lateral positions of the particles $r_{||}$. In other words, the scattered intensity contains information about the lateral ordering of the nanoparticles. However, carrying out the summation over N particles needs a massive calculation power. Approximations are required to reduce the calculation power for realistic analysis of experimental GISAXS patterns. Among these approximations, that is most widely used in SAXS / GISAXS analysis is the local monodisperse approximation (LMA) which was introduced by Pedersen et al. [83-84]. LMA assumes local monodiperse domains with sizes larger than the coherence length of X-ray beam (Fig. 2.11). The waves are assumed to be scattered coherently from each domain and interfere incoherently from different domains. Another useful approximation is the decoupling approximation (DA) which assumes no correlation between particle sizes and their location, for more details about the DA one can refer to [51, 85]. Under the LMA approximation a nearly perfect correlation between size and shape of particles is assumed. Using this assumption equation 2.40 reduces to

$$\left(\frac{d\sigma}{d\Omega}\right)_{diffuse} = \frac{k_0^2}{16\pi^2}\left|\delta n_C^2\right|^2 \left\langle \left|\mathcal{F}_i(\mathbf{q}_{\|}, \mathrm{k_{zi}}, \mathrm{k_{zf}})\right|^2 S(q_{\|}) \right\rangle_D \tag{2.41}$$

Where $\langle \cdots \rangle_D$ indicates the ensemble average over domains i.e over the size distribution of the nanoparticles. $S(q_{\|})$ is the interference function or the structure factor. For a monodisperse system the average over size distribution is dropped out and equation 2.41 becomes

$$\left(\frac{d\sigma}{d\Omega}\right)_{diffuse} = \frac{k_0^2}{16\pi^2}\left|\delta n_C^2\right|^2 \left|\mathcal{F}_i(\mathbf{q}_{\|}, \mathrm{k}_{zi}, \mathrm{k}_{zf})\right|^2 S(q_{\|}) \tag{2.42}$$

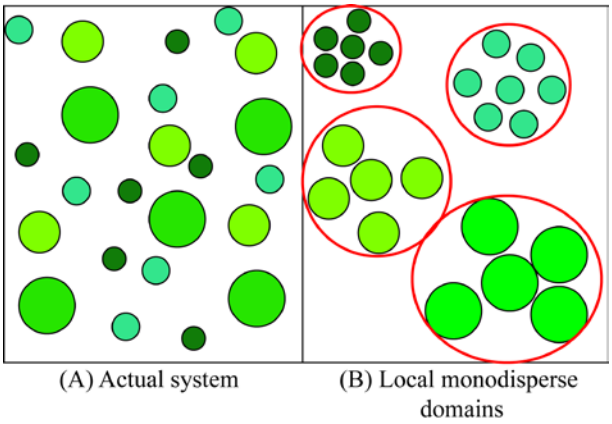

Fig. 2.11 *Schematic illustrations of (A) actual sample with particles having different sizes (indicated in different colors) and (B) local monodisperse domains with identical particles surrounded by red circles.*

However, there are many simple models for the structure factor which can be summed up in three useful cases; disordered system, ordered lattice and lattice losses the long-range order in one or two directions. For a detailed discussion about the models for the structure factor one can refer to many text books [51, 85]. For a system with short-range order the structure factor within the Percus-Yevick approximation for hard spheres (particles interacting with hard core potential) with diameter D_{hs} and volume fraction η_{hs} is given by [86]:

$$S(q_{\|}) = \left\{1 + 24\frac{\eta_{hs} G(q_{\|} D_{hs})}{q_{\|} D_{hs}}\right\} \tag{2.43}$$

Where G is a function composed of set of cosine and sine functions (see Appendix A.2)

2.5 Grazing incidence X-ray fluorescence

As mentioned in section 2.2.1 one consequence of X-ray interactions with matter is the emission of characteristic X-ray fluorescence lines which depends on the type of the chemical element. Such lines can be used as a fingerprint to identify different elements within an unknown sample. However, the intensity of the emitted fluorescence from a certain atom depends on its absorption cross-section i.e in the X-ray region it depends on the atomic number. The penetration depth of the evanescent field under grazing incidence depends on the angle of incidence [87-89]:

$$\Lambda(\alpha_i) = \frac{\lambda}{\sqrt{8}\pi}\left[\sqrt{\left(\alpha_i^2 - \alpha_c^2\right)^2 + 4\beta^2} - \left(\alpha_i^2 - \alpha_c^2\right)\right]^{-\frac{1}{2}} \tag{2.44}$$

where β is the imaginary part of the refractive index $n = 1 - \delta + i\beta$. Fig. 2.12 shows an example of X-ray penetration depth into water subphase. At incident angles above the critical angle, this is about a few micrometers. However, at incident angles well below the critical angle the X-ray penetrates to about 46 Å into water and increases rapidly upon reaching the critical angle (inset, Fig. 2.12).

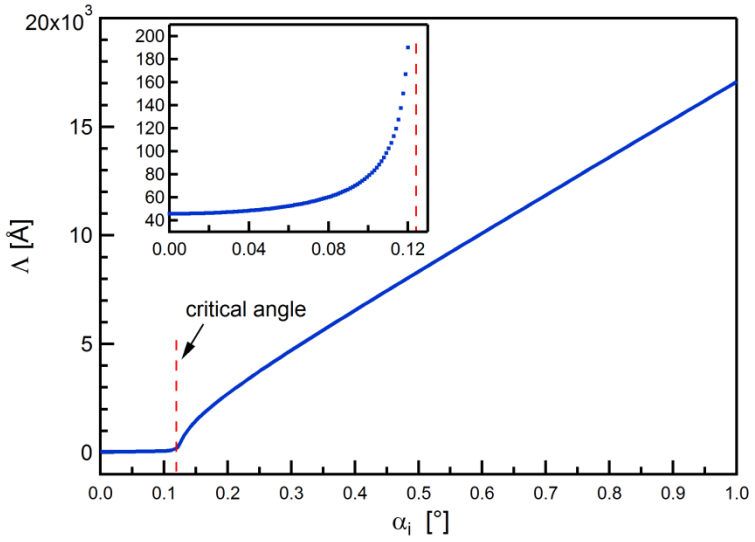

Fig. 2.12 *The penetration depth into water subphase as a function of incidence angle at X-ray energy of 10 keV. The inset shows the penetration depth below the critical angle.*

The fluorescence intensity $I_i^f(\alpha)$ from a chemical element *i* at a distance *z* from the air-water interface at an incidence angle α can be written as:

$$I_i^f(\alpha) = S\int_0^\infty I^{ill}(z,\alpha)\, c_i(z) \exp(-z/L_i)\, dz\,. \tag{2.45}$$

S is a proportional constant which is scaled out in our experimental system by the normalization to the fluorescence signal from the corresponding blank buffer, $c_i(z)$ is the concentration of element *i* at a depth *z*. The exponential term represents the attenuation of the fluorescence emission between the position *z* and the detector, where L_i is the attenuation length of water at the characteristic fluorescence line, e.g. $L_{\text{K-K}\alpha}$ = 68.14 µm and $L_{\text{Ca-K}\alpha}$ = 93.7 µm.

The illumination profile $I^{ill}(z,\alpha)$ can be determined by the matrix propagation technique [90] using slabs model. The electron densities and the thicknesses of the slabs are obtained from the XRR analysis. The illumination profile is given by $\left|E^+(z)+E^-(z)\right|^2$ where $E^+(z)$ and $E^-(z)$ are the forward and backward propagating waves with respect to the sample surface, respectively. To obtain the exact expression for $E^+(z)$ and $E^-(z)$, the Abelès matrix formalism [76, 91] for stratified layers (equation 2.27) can be split into two parts in layer *j* in order to determine the electric field amplitudes E_j^+ and E_j^- in layer *j*:

$$\begin{pmatrix} E_0^+ \\ E_0^- \end{pmatrix} = \frac{C_1 C_2 \ldots C_j}{t_1 t_2 \ldots t_j} \begin{pmatrix} E_j^+ \\ E_j^- \end{pmatrix}, \quad \begin{pmatrix} E_j^+ \\ E_j^- \end{pmatrix} = \frac{C_{j+1} C_{j+2} \ldots C_{N+1}}{t_{j+1} t_{j+2} \ldots t_{N+1}} \begin{pmatrix} E_{N+1}^+ \\ 0 \end{pmatrix} \tag{2.46}$$

where E_0^+ the incident wave , E_0^- the reflected wave, E_{N+1}^+ the transmitted wave after layer *N* and C_{j+1} is the propagation matrix expressed as

$$C_{j+1} = \begin{pmatrix} \exp(-ik_{zj}.d_j) & r_{j-1}\exp(-ik_{zj}.d_j) \\ r_{j-1}\exp(ik_{zj}.d_j) & \exp(ik_{zj}.d_j) \end{pmatrix} \tag{2.46}$$

where k_{zj} is the z-component of the wave vector at the interface between layers j and $j + 1$, d_j the thickness of layer j, t_j and r_j are the Fresnel transmission and reflection coefficients, respectively. Since the matrices can be re-written as

$$C_1 C_2 ... C_{N+1} = \begin{pmatrix} a & b \\ c & d \end{pmatrix}, \; C_{j+1} C_{j+2} ... C_{N+1} = \begin{pmatrix} a_j & b_j \\ c_j & d_j \end{pmatrix}, \tag{2.48}$$

E_j^+ and E_j^- can then be given by the following equations:

$$E_j^+ = t_1 t_2 ... t_j \frac{a_j}{a} E_0^+ \text{ and } E_j^- = t_1 t_2 ... t_j \frac{c_j}{a} E_0^+ . \tag{2.49}$$

Finally, $E^+(z)$ and $E^-(z)$ can be expressed as:

$$\begin{aligned} E^+(z) &= E_j^+ \exp(ik_{zj}(z - \sum_{i=1}^{j-1} d_i)), \\ E^-(z) &= E_j^- \exp(-ik_{zj}(z - \sum_{i=1}^{j-1} d_i)) \end{aligned} \tag{2.50}$$

Fig. 2.13 shows simulated electric filed intensity distribution at the air-water interface. The calculations were split around the critical angle to preserve high resolution and to reduce the calculation power (see the z-range below and above the critical angle, in Fig. 2.13A and B, respectively).

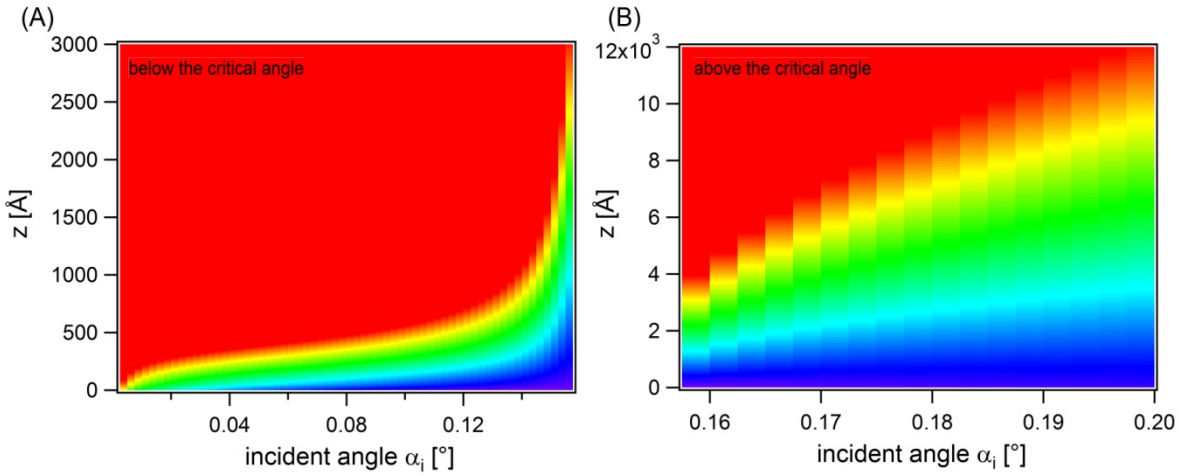

Fig. 2.13 *The electric field intensity distribution at the air-water interface. In order to reduce the calculation power and preserve the high spatial resolution the determination of the electric field intensity was split around the critical angle (α_c = 0.15°). (A) The electric field intensity distribution below the critical angle. (B) The electric field intensity distribution above the critical angle.*

The concentration profile of the ion species condensed at the carbohydrate head group of LPS Ra was parameterized as [40]

$$c_i(z) = c_0 + c_{\max} \frac{\sqrt{e}\,(z - z_{HC})}{z_{\max}} \exp\left(-\frac{(z - z_{HC})^2}{2z_{\max}^2}\right), \qquad (2.51)$$

where c_0 is the bulk concentration, z_{HC} is the position which defines the starting point of the concentration profile. This enabled us to model ion distributions that possess a concentration maximum with a smooth decay to the bulk concentration with only two free parameters: (i) the concentration maximum $c_{\max}$ and (ii) the *z*-position of this maximum $z_{\max}$. Throughout the GIXF analysis, the Levenberg-Marquardt nonlinear least square optimization [92] was used for the refinement of the model. Fig. 2.14 shows an example of experimental data taken form measurements on lipopolysacchride monolayer at the air-water interface (blue open circles). The simulations for various values of $z_{\max}$ are shown in solid lines. Form the chi-square plot one can determine the z-resolution to be ± 3 Å (inset, Fig. 2.14).

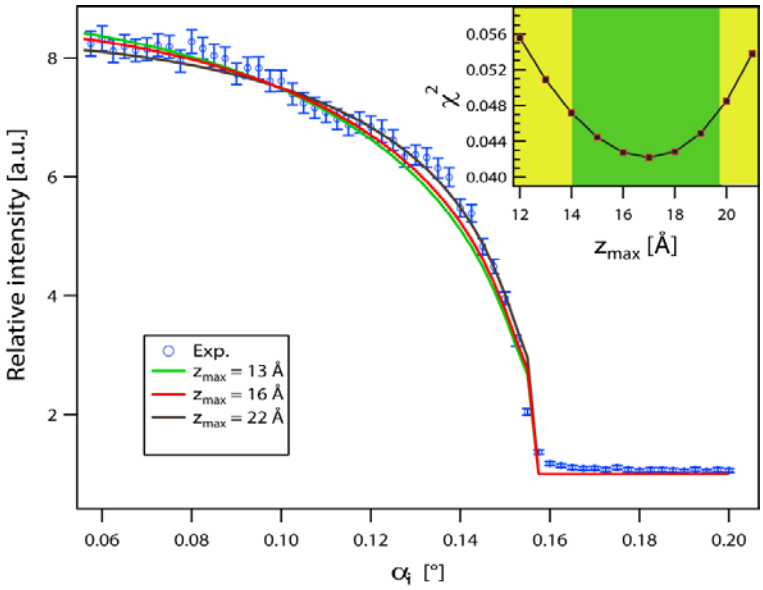

Fig. 2.14 *Experimental relative fluorescence intensity of Ca K_α from LPS Ra on Ca-loaded buffer (blue open circles) corresponding to Fig. 6.5A in section 6.1.2. The solid lines correspond to simulations at different z_{max} values followed by least square fit of c_{max}. The inset shows the chi-square plot versus z_{max}. The z- resolution is defined as variations within 10% as indicated by green area which corresponds in this case to ± 3Å.*

3. Materials and Methods

3.1 Materials

3.1.1 Lipids

SOPC: The structure of SOPC (1-Stearoyl-2-oleoyl-sn-glycero-3-phosphocholine) is shown in Fig. 3.1A. It consists of two hydrocarbon chains with one unsaturated carbon bond and a zwitterionic moiety of phosphocholine as a head group. The molecule has a molecular weight of 788.13 g/mol with a transition temperature of T_m = 6° C. SOPC was purchased from Avanti Polar Lipids (Alabaster, AL, USA).

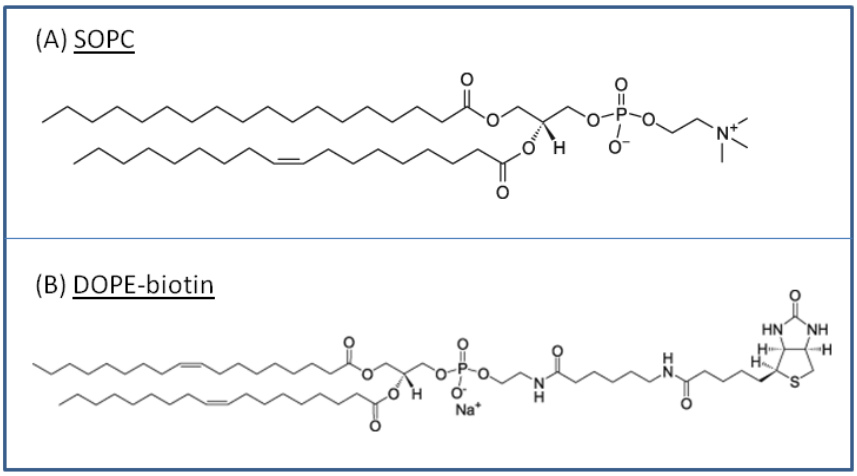

Fig. 3.1 (A) *The chemical structure of SOPC and (B) the chemical structure of DOPE-biotin.*

DOPE-biotin: The structure of DOPE-biotin (1,2-dioleoyl-sn-glycero-3-phosphoethanolamine-N-cap biotinyl) is shown in Fig. 3.1B. It consists of two hydrocarbon chains with two unsaturated carbon bonds and a phosphoethanolamine head group functionalized with biotin. DOPE-biotin has a molecular weight of 1105.5 g/mol with a transition temperature of T_m ~ -16° C. DOPE-biotin was purchased from Avanti Polar Lipids (Alabaster, AL, USA).

3.1.2 Lipopolaysaccarides

The chemical structure of the wild type lipopolysacchrides is shown in Fig. 3.2. This molecule consists of six hydrocarbon chains and a carbohydrate head group. In general,

the carbohydrate head group consists out of three parts, the inner core, the outer cores and the O-polysaccharide. The inner core consists of two negatively charged phosphorylated glucosamines (together with hydrocarbon chains it called Lipid A) and two negatively charged 2-keto-3-deoxyoctonoic acid (KDO) units (LPS Re). The outer core has three heptose units (two of them are phosphorylated), four glucose and N-acetylglucosamine units (LPS Ra) [93]. In addition to the LPS Ra, the wild-type has O-polysacchride which is highly polydispersive [94]. LPS Ra was purified from the bacterial strain R60 of *Salmonella enterica* sv. Minnesota and were kindly provided by U. Seydel and K. Brandenburg (Forschungszentrum Borstel, Hamburg, Germany).

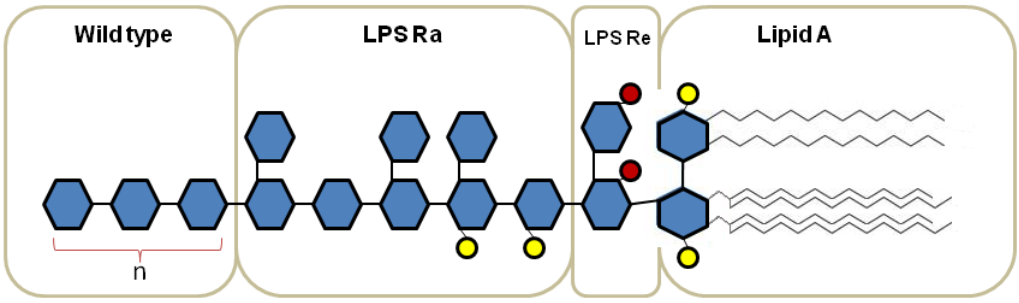

Fig. 3.2 *The chemical structure of lipopolysacchride molecule. Yellow and red circles denote the phosphate and carboxylate groups, respectively.*

3.1.3 Proteins and peptides

Neutravidin: The three dimensional structure of NA is shown in Fig. 3.3. NA is a deglycosylated form of avidin that has a strong affinity to biotin with a dissociation constant of $K_d \sim 10^{-15}$ M which is the strongest known noncovalent bond [95-96]. In contrast to commonly used avidin and streptavidin that tend to form two-dimensional crystals on the membrane surface [97-98], NA possesses a much lower isoelectric point (pI = 6.3) compared to avidin and streptavidin, showing no tendency to crystallize. NA was purchased from Invitrogen Molecular Probe (Darmstadt, Germany).

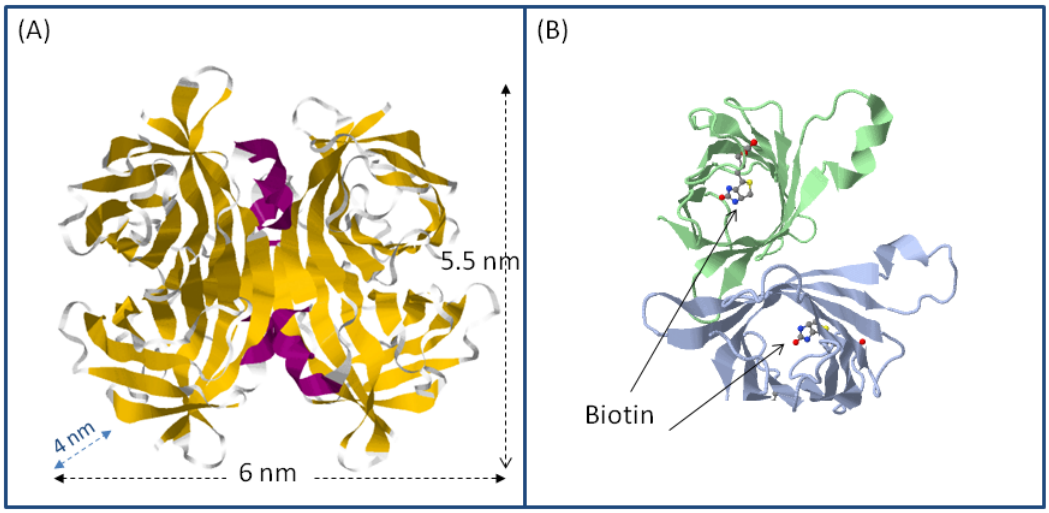

Fig. 3.3 *(A) The three dimensional structure of the tetramer neutravidin molecule.(B) Two subunits of the NA showing the binding pockets of NA with the biotin molecules are pointed by the arrows. [PDB: 2avi].*

Variant Surface Glycoprotein: the structure of VSG is shown in Fig. 3.4. VSG are covalently linked at its C-terminal to glycerophosphatidylinositols (GPIs). The core structure of the GPI-anchor consists of phosphodiester-linked inositol, glucosamine, three mannose sugars and a phosphoethanolamine (P-EtN). The protein is attached to the GPI-anchor with amide bond between the carboxyl-terminal residue of the protein and the amino group of the P-EtN. VSG (MITat1.2) was kindly provided by A. Hartel and M. Engstler (Würzburg University, Germany).

Protamine: The structure of herring protamine is shown in Fig. 3.5. Protamine is arginine rich peptide with an amino acid sequence:

RRRRGARRRRTTRRRPRRRRIPRSSSRRRRA

Protamine has a molecular weight of M_w = 4112 Da, isoelectric point of pI ~ 13.3 and carries a positive charge of Q ~ + 19.8 at pH 7.4. Protamine (chloride salt) was purified by the method reported in [99].

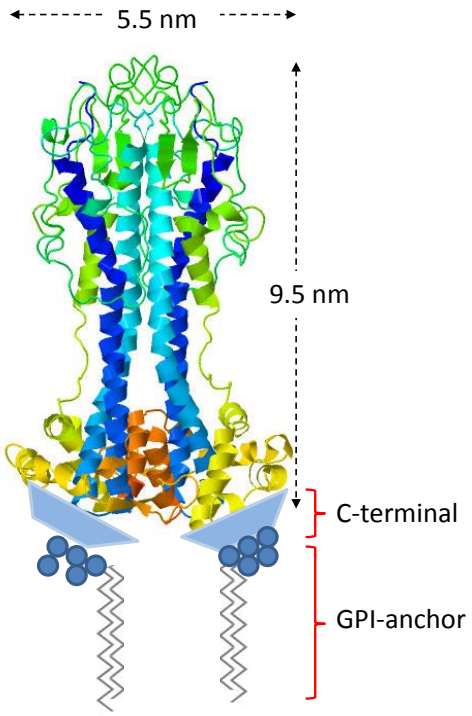

Fig. 3.4 *The three dimensional structure of VSG which consists of two identical subunits [PDB: 2vsg].*

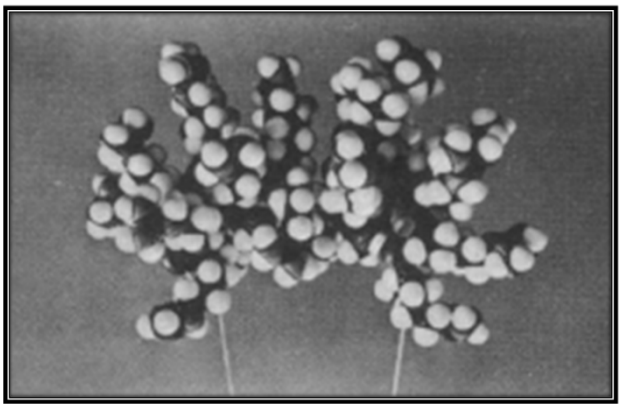

Fig. 3.5 *The three dimensional structure of protamine from herring as proposed by dark field electron microscopy experiment (the image was taken from [100]).*

Anti-sepsis peptide (Pep 19-2.5): Pep 19-2.5 is a small peptide consists of 19 amino acids with a sequence given as:

GCKKYRRFRWKFKGKFWFWG

Pep 19-2.5 has a molecular weight of M_w = 2712 Da, isoelectric point of pI ~ 11.2 and carries a positive charge of Q ~ + 7.7 at pH 7.4. Pep 19-2.5 was synthesized as described

by Kowalski et al. [101-102] and was kindly provided by K. Brandenburg (Forschungszentrum Borstel, Hamburg, Germany).

3.1.3 Fluorophores

In fluorescence microscopy experiments a number of different dyes were used for protein conjugation. In the following table a list of the dyes which were used throughout this study. The fluorophores were purchased from Invitrogen Molecular Probe (Darmstadt, Germany).

Table 3.1. List of the dyes that were used in protein labeling with their absorption and emission maxima. These values were taken from company sources.

Dye	Absorption max. [nm]	Emission max. [nm]
TAMRA	540	565
Alexa-Fluor 555	555	565
Rhodamine Red	570	590

3.1.3 Chemicals and buffers

Double deionized water (MilliQ, Molsheim) with a specific resistance of $\rho > 18$ MΩcm was used throughout this study. Unless stated otherwise, chemicals were purchased from Sigma-Aldrich (Munich, Germany) and used without further purification. The following buffers were used:

Phosphate buffered saline (PBS): 137 mM NaCl, 2.7 mM KCl, 10 mM $Na_2HPO_4H_2O$, and 1.76 mM KH_2PO_4 at pH 7.4.

Ca-free buffer: 100 mM KCl, 5 mM Hepes at pH 7.4.

Ca-loaded buffer: additionally contained 50 mM $CaCl_2$ at pH 7.4.

Hepes buffer: 100 mM KCl, 5 mM Hepes, and 1 mM $CaCl_2$ at pH 7.4.

Tris buffer: 100 mM NaCl, 10 mM Tris, and 1 mM $CaCl_2$ at pH 7.4.

Sodium bicarbonate buffer: 100 mM NaCl, 1 mM $CaCl_2$, 100 mM Na_2CO_3 titrated with 100 mM $NaHCO_3$ to pH 8.3.

3.2 Preparations

3.2.1 Suspensions and solutions

SOPC / DOPE-biotin: SOPC and DOPE-biotin were dissolved in chloroform. The mixtures were prepared by mixing the pure solutions of SOPC and DOPE-biotin with a desired molar fraction of DOPE-biotin (e.g. 5 mol%, 2 mol% etc.).

Neutravidin: NA solution made by dissolving the NA powder in Hepes buffer with a concentration of 1 mg/ml. Depending on the type of the experiment, dilutions with concentrations in the range 10-100µg/ml were made. For single particle tracking experiments a mixture of unlabeled NA and labeled NA were prepared from pure solutions with a molar ratio of ($1:10^6$, $1:10^7$, $1:10^8$ labeled-NA:unlabeled-NA).

Variant Surface Glycoprotein: VSG powder was dissolved in bicarbonate buffer or in Hepes buffer with a concentration of 1-2 mg/ml.

LPSs: The lyophilized powder was dissolved in liquid phenol (90%), chloroform, and petroleum ether (2:5:8 by volume). The mixture appeared cloudy and could be made clear by the addition of solid phenol [103]. The stock solution was adjusted to a final concentration of 1 mg/ml.

Pep 19-2.5: The powder was dissolved in phosphate buffered saline (PBS) containing 137 mM NaCl, 2.7 mM KCl, 10 mM $Na_2HPO_4H_2O$, and 1.76 mM KH_2PO_4 at pH 7.4 with a concentration of 2.5 mg/ml.

Protamine: The lyophilized powder was dissolved in PBS at a concentration of 0.1 g/ml.

3.2.2 Preparation methods

3.2.2.1 Substrates

Si-wafers with native oxide (SiMat, Landsberg, Germany) or glass cover slides (Karl Hecht, Sondheim, Germany) have been used as substrates throughout this study. The substrates were cleaned with successive sonication for 15 minutes with acetone, ethanol, methanol and deionized water to remove any organic substances from their surfaces. Afterwards, they were incubated more than 30 min at 60 °C with a solution made of H_2O_2, NH_3, H_2O with a volume ratio of 1:1:5 (RCA cleaning) [104]. This step increases the SiO-layer and therefore increases the surface hydrophilicity. Then, the substrates were rinsed about 10-20 times with deionized water and dried in oven at 70 °C for 30 min. Eventually, the substrates were placed in a vacuum chamber to remove the remaining residual water molecules.

3.2.2.2 *Solid supported membrane bilayer*

The lipid bilayer was prepared by vesicle fusion method. The vesicle suspension was added into a Si-substrate with native oxide or glass cover slides. The lipids were dried in a glass tube under a stream of nitrogen gas and placed in a vacuum chamber overnight to insure the removal of the organic solvent. The dried lipids were suspended in a buffer followed by vortex to form giant multi-lamellar vesicles. To make small uni-lamellar vesicles (Fig. 3.6), the lipid suspension was sonicated with a tip-sonicator made out of titanium for ~ 30 min. Afterwards, the suspension was centrifuged at 10^4 rpm to separate the titanium particles. Finally, the lipid suspension was added into the substrate and incubated at room temperature for more than 3 hours or at 40 °C for more than 1 hour to insure a full coverage of the substrate (Fig. 3.6).

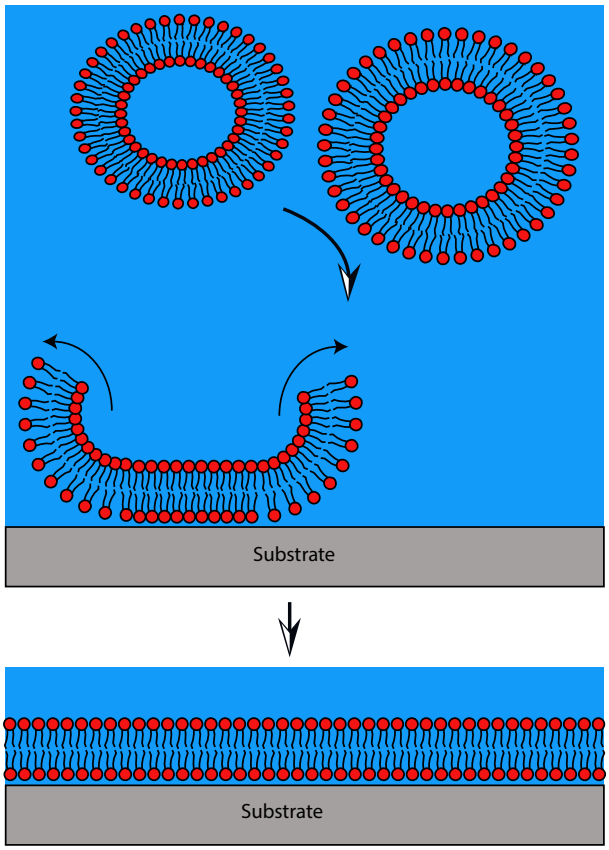

Fig. 3.6 *Lipid bilayer is deposited into a substrate by vesicle fusion.*

3.2.2.1 VSG reconstitution into lipid vesicles

Prior to reconstituting VSGs into lipid vesicles, VSGs were dissolved in bicarbonate buffer with a concentration of 2 mg/ml and were labeled with TAMRA or Alexa-Fluor dyes according to a company protocol (Invitrogen Molecular Probe, Darmstadt, Germany). The reconstitution of VSG into lipid vesicles was done through a detergent mediated method [105-106]. SOPC was dried in vacuum overnight and then suspended in Tris-buffer containing 0.2% w/v Na-deoxycholate with a concentration of 1 mg/ml. the labeled VGSs were mixed with SOPC solution at protein / lipid ratio of 1:500. The suspension was stirred for 30 min at 30 °C followed by incubation at 37 °C for 90 min. the detergent was removed by incubating the solution with bio-beads for 1-3 hours under shaking. Non-incorporated VSGs was separated with a four steps sucrose gradient (2 M, 1.2 M, 0.8 M, 0.4 M) by ultracentrifugation at 275000 g for 24 hours. The collected proteoliposomes were dialyzed against Hepes buffer overnight at 4° C. The final protein

to lipid ration was determined using phosphate assay [107] and by the absorption at 280 nm.

3.2.2.3 *Langmuir lipid monolayer*

Langmuir lipid monolayer is made by spreading the lipids from their stock solutions gently on the surface of a buffered subphase using Hamilton syringe. The monolayer is incubated for about 20 min to allow for the evaporation of the organic solvent from the interface. Afterwards the monolayer is compressed using a movable barrier to a certain surface pressure. Protein or peptide solutions can be injected underneath the monolayer from the other side of the barriers without deforming or disturbing the monolayer (Fig. 3.7).

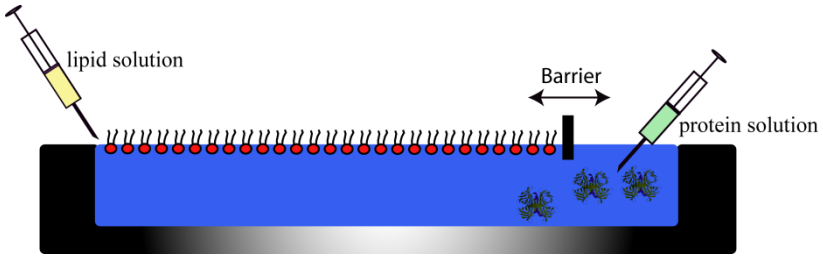

Fig. 3.7 *Lipid monolayer on a Langmuir film balance was spread by injecting lipids into the air-water interface. The barrier can compress the monolayer to a desired surface pressure. Proteins or peptides can be injected underneath the monolayer from the other side of the barrier.*

3.2.2.4 Sample environment

For microscopy experiments a self-made sample chamber was used as shown in Fig. 3.8. The sample chamber was used both in fluorescence recovery after photobleaching and single particle tracking experiments. The cover slide has dimensions of 24×24×0.1 mm. prior to experiments the sample chamber components were cleaned with a successive 2% Hellmanex and deionized water under sonication for 15-30 min (except the substrate) followed by 10 times rinsing with deionized water.

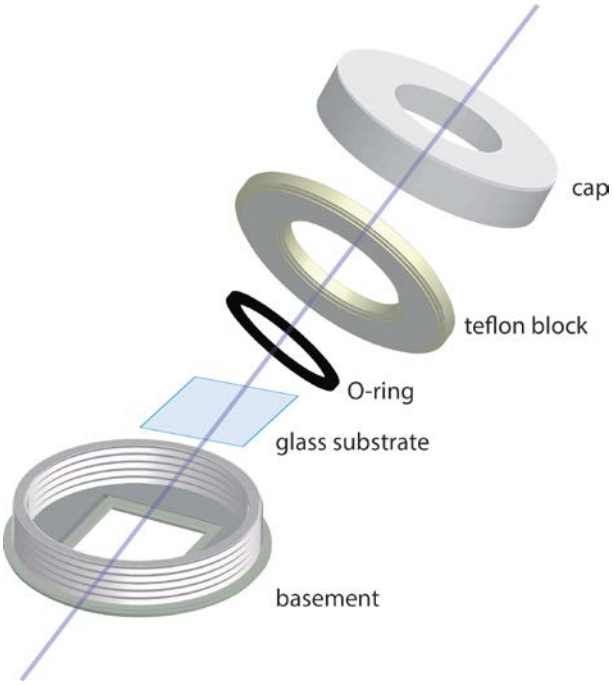

Fig. 3.8 *Self-made sample chamber was used for microscopy experiments.*

In X-ray scattering experiments a self-made sample chamber was developed with short optical path length (2 cm) in order to increase the transmission of the X-ray beam. The chamber consists mainly of silicon substrate, Kapton windows and main body made out of Teflon (Fig. 3.9). This chamber was used in X-ray experiments that have been carried out at the solid-liquid interface.

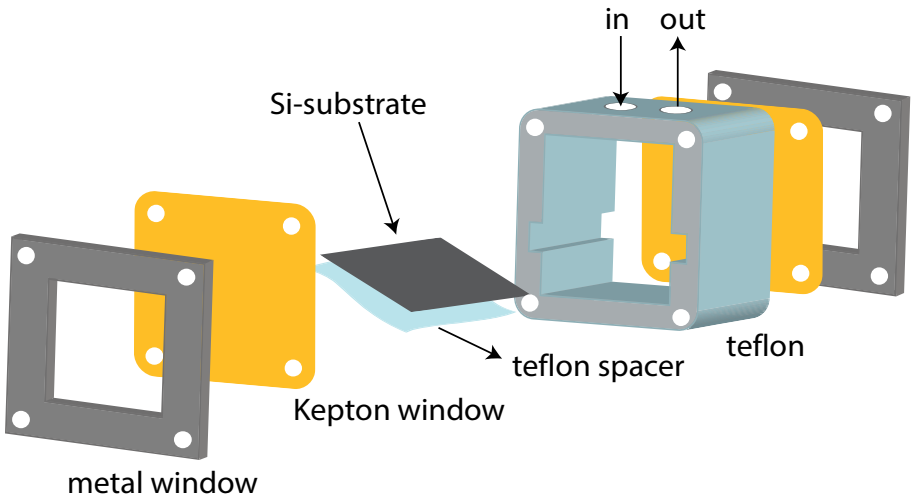

Fig. 3.9 *Illustration of the liquid cell which was used in X-ray scattering experiments at the solid-liquid interface.*

In addition, for experiments which were carried out at the air-water interface, either a self-made small film balance (with a total volume of ~ 40 ml) or a Langmuir film balance developed at the ID10B beamline (total volume of ~ 380 ml) have been used as shown in Fig. 3.6 in the previous section. All Experiments were carried out at room temperature.

3.2 Methods

3.2.1 Specular X-ray reflectivity

All X-ray scattering experiments including XRR were carried out at the beamline ID10B of the European Synchrotron Radiation Facility (ESRF, Grenoble).

The samples were irradiated with a monochromatic synchrotron beam either with an energy of 8 keV (λ = 1.55 Å), 10 keV (λ = 1.24 Å) or 22 keV (λ = 0.56 Å). For experiments at the air-water interface the film balance was kept in a He atmosphere to preserve identical conditions for all measurements. Fig. 3.8 represents a schematic drawing of the experimental setup and the scattering geometry for XRR experiments. From geometrical considerations, the momentum transfer perpendicular to the sample surface can be written as:

$$q_z = \frac{4\pi}{\lambda}\sin(\alpha_i) \tag{3.1}$$

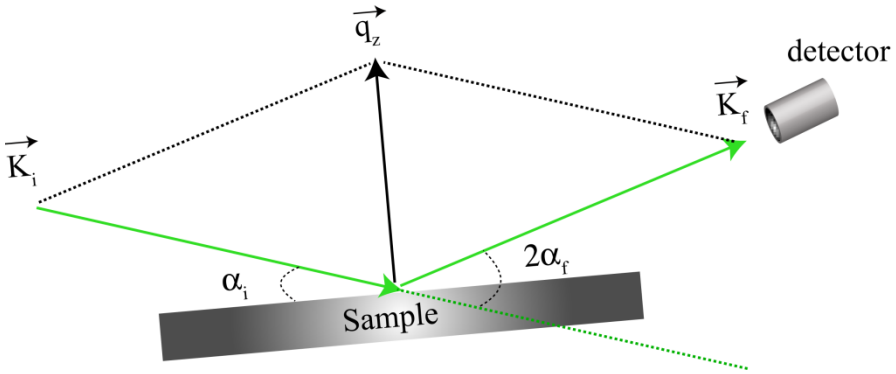

Fig. 3.8 *Geometry of the specular X-ray reflectivity experiments at the beamline ID10B (ESRF, Grenoble, France)*

XRR was measured with a linear detector (Vantec-1, Bruker AXS, USA). However, it should be stressed out that there are three main essential steps for the data treatment that should be done before XRR refinement. Fig. 3.9 illustrates these steps and their influence on the reflectivity curve which can be summarized as:

1. Normalization of the detector readout to the incident beam flux which could influence some features in the XRR curve (Fig. 3.9A).
2. Subtraction of the diffuse intensity background at $\alpha_f \neq \alpha_i$ (Fig. 3.9B). This step affects the overall layers roughness.
3. Correction due to the illumination area i.e footprint correction. This can be done by multiplying the measured intensity by a factor from geometrical considerations given by $F = h/d \sin(\alpha_i)$, where h is the slit height and d is the sample size (Fig. 3.9C). Ignoring this correction will lead to underestimation of the layers electron density. Note, that the footprint correction can be skipped (e.g film balance experiments) if the sample dimension along the incident beam is very large i.e $d \sin(\alpha_c) > h$.

After the pre-analysis of the XRR data, the specular reflectivity was analyzed using the Parratt formalism [75, 108]. with a genetic minimization algorithm implemented in the MOTOFIT software package [109].

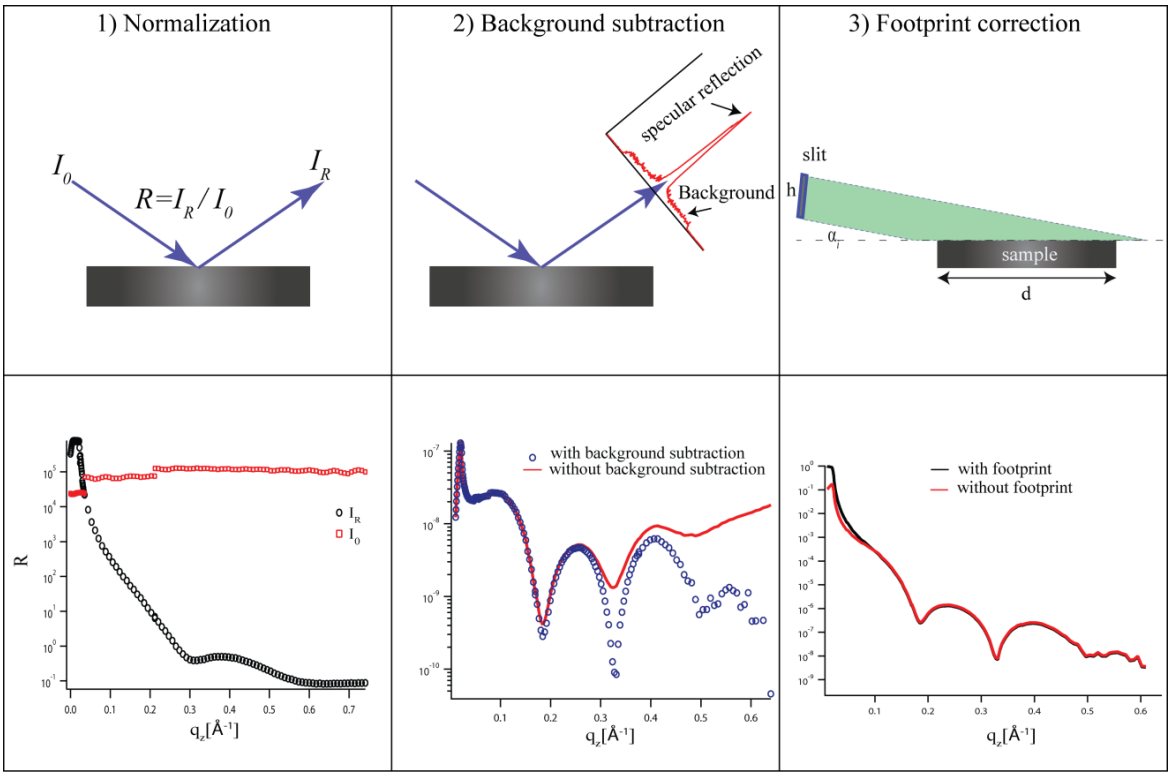

Fig. 3.9 *The upper panel shows the main three corrections that should be done for every XRR raw data. The lower panel illustrates the influence of these corrections on the XRR curves. To highlight the desired features in the XRR-curves, the plots are viewed in log(R)-scale or in log(R.q_z^4)-scale.*

3.2.2 Grazing incidence small angle scattering

For GISAXS experiments at the air-water interface, the sample was illuminated at an incident angle of $\alpha_i = 0.11°$, which is slightly below the critical angle of total reflection, $\alpha_c = 0.125°$ (beam footprint: 1.8 × 42 mm^2). The scattering signal was collected through a Soller collimator and a cross-slit (0.3 × 15 mm^2) in front of the linear detector. The GISAXS signal was recorded by collecting the intensity from an off-specular position ($q_y \geq$ 0.02 Å^{-1}) with a resolution of $\delta q_y \approx$ 0.0018 Å^{-1}. In additional experiments a two dimensional detector (Maxipix, ESRF, based on a developed Medipix at CERN) was used. A correction for the non-linearity of the detector readout was done due to the dead time of the pixel readout as described in reference [110].

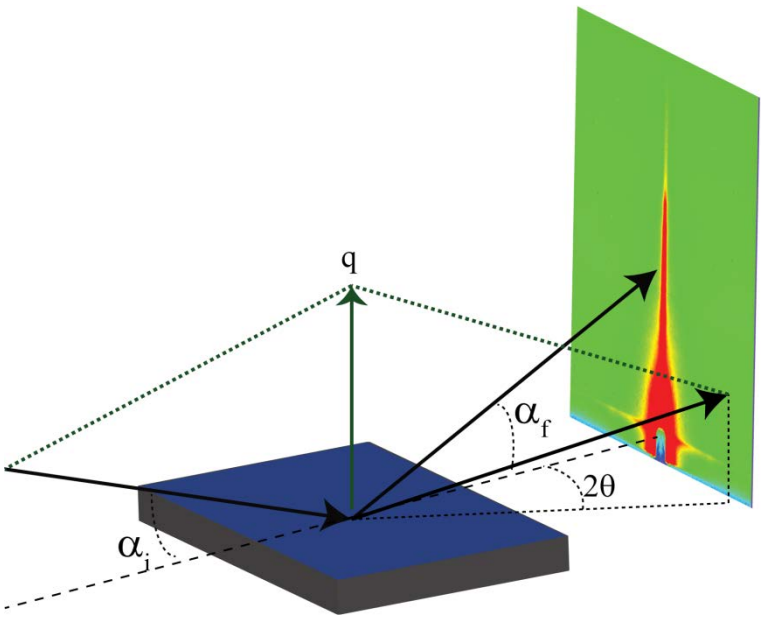

Fig. 3.10 *Geometry of the GISAXS experiments at the beamline ID10B (ESRF, Grenoble, France)*

After the background subtraction, GISAXS signal was normalized to the incoming beam. The two dimensional detector readout in angular coordinate (α_f, θ) can be transferred to a reciprocal space map (q_z, q_y) map by

$$q = \begin{pmatrix} q_x \\ q_y \\ q_z \end{pmatrix} = \frac{2\pi}{\lambda} \begin{pmatrix} \cos(\alpha_f)\cos(2\theta) - \cos(\alpha_i) \\ \cos(\alpha_f)\sin(2\theta) \\ \sin(\alpha_f) + \sin(\alpha_i) \end{pmatrix}, \tag{3.2}$$

where the weak q_x-dependence ($q_x << q_z$) is neglected. The measured GISAXS signals have been fitted by the program FitGISAXS [86].

3.2.3 Grazing incidence X-ray fluorescence

GIXF measurements were carried out at incident angles α_i below and above the critical angle of total reflection, α_c. The experimental setup is shown in Fig. 3.11. X-ray fluorescence signals from elements in the illuminated volume were recorded with an energy sensitive detector (Vortex, SII NanoTechnology, USA) and normalized by the detector counting efficiency. Subsequently, the intensities were normalized by the

elastically scattered beam intensity to compensate systematic differences between the experiments. Fig. 3.11 shows a typical fluorescence spectrum taken at an incident angle of 0.3° from Hepes buffer containing KCl salt.

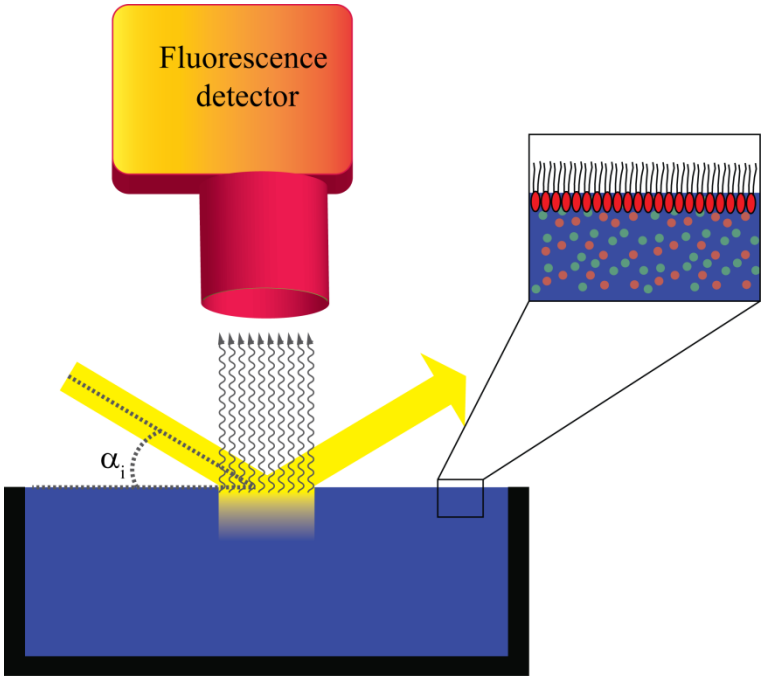

Fig. 3.11 *Geometry of the GIXF experiments at the beamline ID10B (ESRF, Grenoble, France)*

The fluorescence contribution from each characteristic line was extracted using a multiple-Gaussian peak fitting routine with a self-written code For Igor Pro (WaveMetrics, Portland, OR, USA). For direct comparison between the experimental results and the theoretically modeled fluorescence signals, the incident angle α_i was transformed into the scattering vector component normal to the interface using equation 1. In the last step, the fluorescence signals in the presence of monolayers were normalized by the signals from the blank buffer. This procedure avoids artifacts arising from the experimental geometry, such as the size of beam footprint and the fluorescence detector aperture.

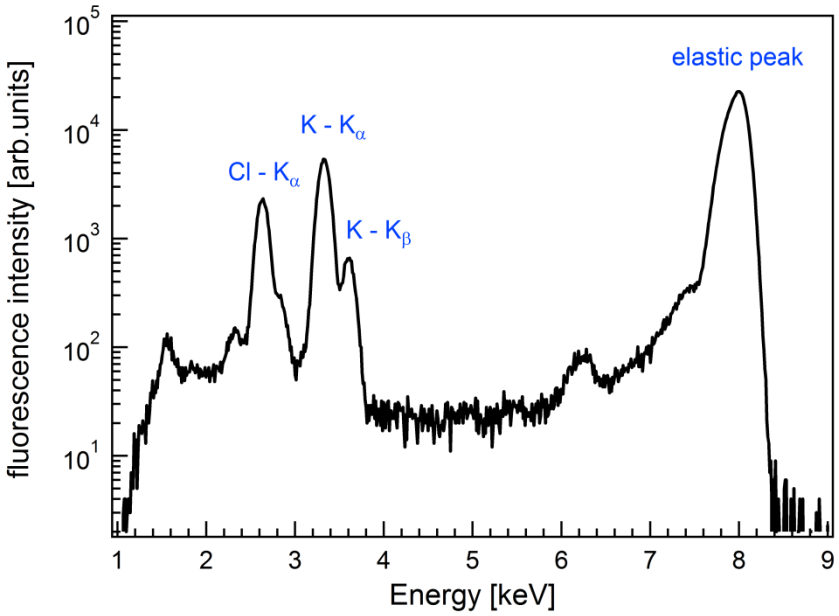

Fig. 3.10 *Fluorescence spectrum of Hepes buffer containing 100 mM KCl at an incident angle of 0.3°. The plot shows the elastically scattered X-ray waves and the characteristic fluorescence lines.*

3.2.4 Fluorescence recovery after photobleaching

FRAP experiments were carried out using spinning disk confocal microscope (PerkinElmer, USA) at Nikon imaging center (bioquant, university of heidelberg). The microscope consists of inverted microscope (Nikon TE-2000), confocal scanning unit (Yokagawa CSU-22) and EMCCD camera (Hamamatsu C9100-02). An oil immersion 60 magnification objective was used with a numerical aperture of NA = 1.4. The setup is equipped with five excitation laser lines with wavelengths of 405, 440, 488, 515 and 561 nm. The sample is bleached with a circular spot with a diameter of 8.9 µm. depending on the sample properties a video was recorded with a rate of 0.5-2 frame/s. The recovery curve was extracted from the video combined with reference curve (Fig. 3.12A). The FRAP intensity is normalized to its reference to exclude the bleaching effect during the recovery (Fig. 3.12B). For the case of a homogenous circular bleaching, the recovered fluorescence intensity *F(t)* is given as [111-112]:

$$F(t) = F_{\infty} - (F_{-} - F_0)\{1 - \exp(-2\tau_D / t)\left[I_0(2\tau_D / t) + I_1(2\tau_D / t)\right]\} \qquad (3.3)$$

Where τ_D is the characteristic diffusion time, F_- is the initial fluorescence intensity, F_0 is the intensity directly after the bleaching and F_∞ is the saturation intensity after infinite limit. I_0 and I_1 are modified Bessel functions of the zero and first order, respectively.

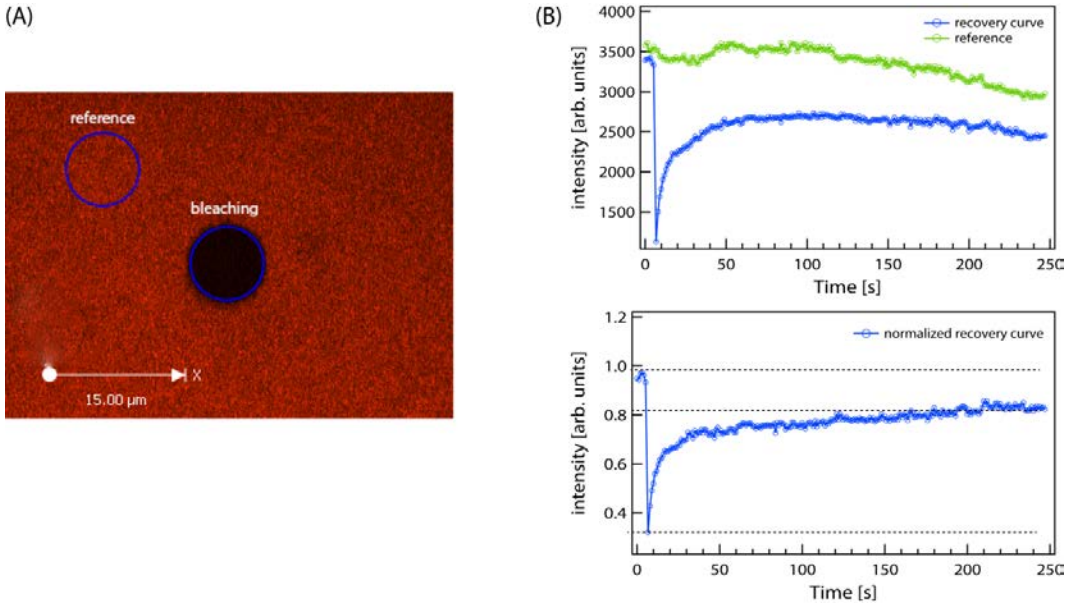

Fig. 3. 11 *(A) FRAP image showing the bleached spot and a reference spot. (B) The recorded FRAP intensity and the reference intensity (upper panel). The normalized FRAP intensity (lower panel).*

Fitting the experimental intensity with equation 3.3 allows the calculation of the diffusion coefficient *D* and the recovery rate *R* as:

$$D = r/4\tau_D \text{ and } R = (F_\infty - F_0)/(F_- - F_0) \tag{3.4}$$

where *r* is the radius of the bleached spot.

3.2.4 Single particle tracking

The SPT experimental setup consists of a conventional inverted fluorescence microscope (Zeiss Axiovert 200), 80 mW Nd-YAG laser with a wavelength of 532 nm and EMCCD camera. EMCCD is an electron multiplying charge-couple device with 512 × 512 pixels which is cooled with Peltier and water (iXon BV887, Andor, Dublin, Ireland). A schematic drawing of the SPT-setup is shown in Fig. 3.13.

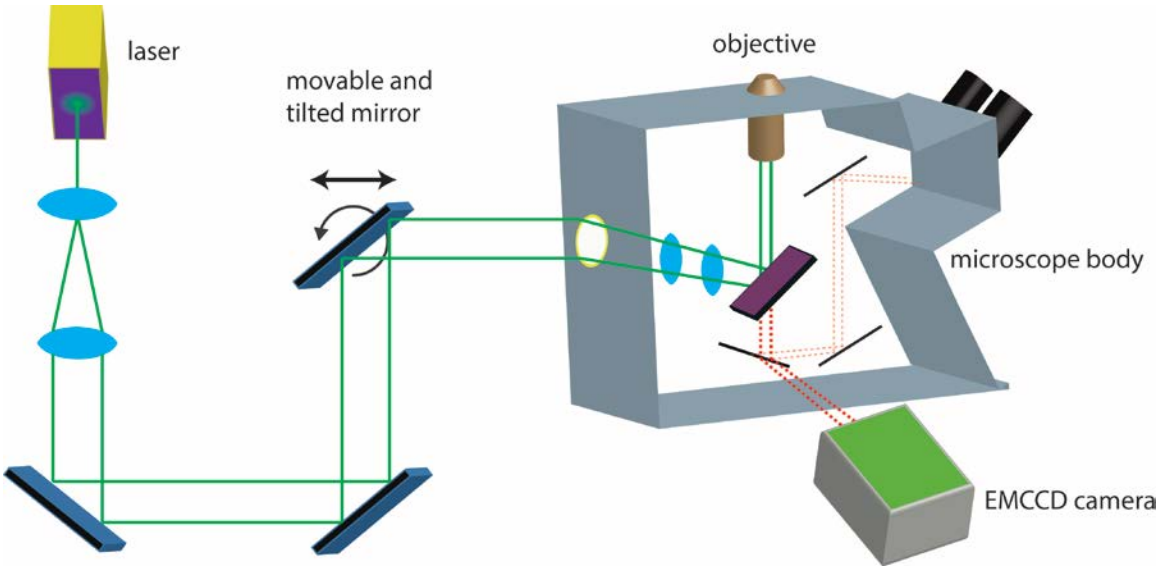

Fig. 3.12 *Illustration shows the main components of single particle tracking instrument. The illumination can be switched between TIRF and EPI using a movable and tilted mirror.*

An objective with 100× magnification, oil immersion and numerical aperture of NA = 1.45 has been used. In all SPT experiments that have been performed in this thesis, videos were recorded at an exposure time of 50 ms corresponding to 19.3 frames/s including the dead time of the EMCCD camera. Using the movable and tilted mirror prior the microscope body one can vary the laser beam angle, so that the angle of total internal reflection (TIRF) at the sample i.e glass-buffer interface can be achieved. This allows for the evanescent field to penetrate only few nanometers into the sample i.e only the particles or molecules near the glass-water interface are probed similar to the principle of GIXF and GISAXS in the previous sections.

The position of the particle was determined by fitting the diffraction spot with two-dimensional Gaussian function (Fig. 3.14A). Tracing a fluorescent particle over a certain time period yields a xy-trajectory as shown in Fig. 3.14B. The trajectory is transformed into a mean square displacement (MSD) plot by using the total internal averaging method (Fig. 3.14C) [113].

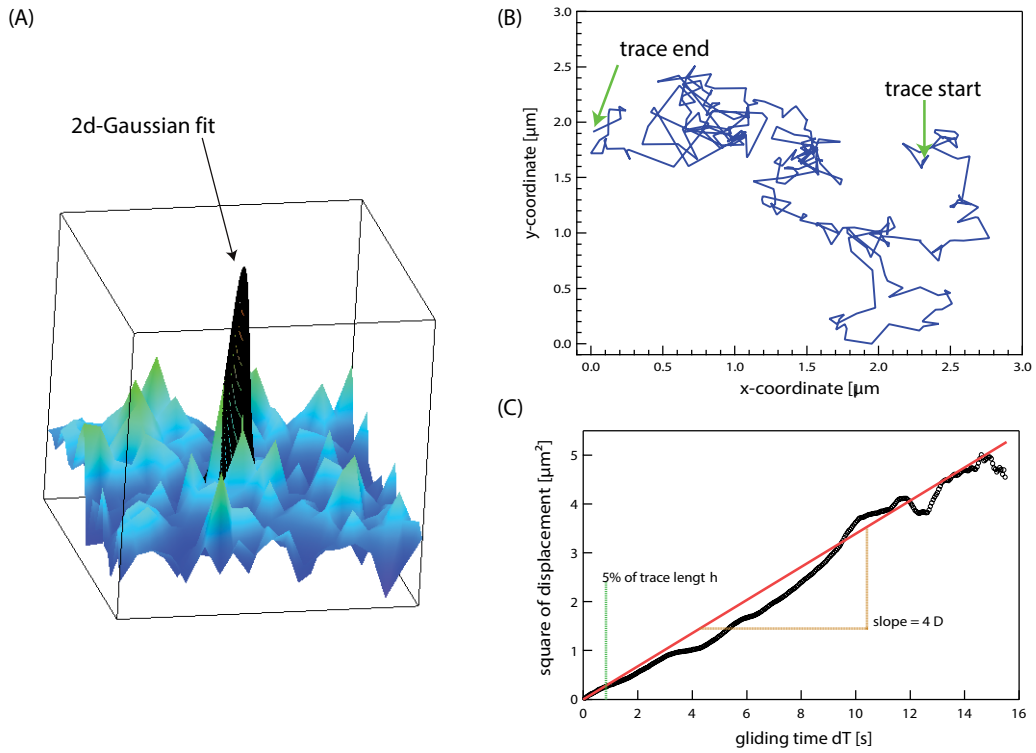

Fig. 3.13 *(A)2D Gaussian fit of the fluorophor peak intensity. (B) A typical diffusion trace of neutravidin bound to SOPC/1 mol% DOPE-biotin membrane bilayer. (C) The corresponding mean square displacement plot (black) and the linear fit to the first 5% data points of the trace length (red line).*

To exclude the effect of low statistics at large gliding time, the diffusion coefficient was determined from the slope of linear fit to the first 5-10 % of the trace length as $MSD = 4Dt$. The type of the diffusion can be determined from the shape of the MSD plot against the gliding time. The analytical forms of the curves of MSD versus time for different types of diffusion are given as:

$$\begin{aligned} &< r^2 >= 4Dt, && \text{, free diffusion} \\ &< r^2 >= 4Dt^{\alpha}, && \text{, anomalous diffusion} \\ &< r^2 >=< r_c^2 > 4Dt(1 - A\exp(-4BDt / < r_c^2 >)), && \text{, confined diffusion} \end{aligned} \qquad (3.5)$$

4. Lateral Correlation between Membrane-Anchored Proteins

Lateral distributions of intrinsic membrane proteins are frequently observed. For instance, densely packed patches of proteins were found in the eukaryotic gap junctions [114-115] and in the purple membranes of halophile bacteria [116]. As stated in section 2.1.1, the driving force of membrane self-assembly is the hydrophobic effect. On other side, the characteristics of the protein assemblies at interfaces in general and at the cell membranes in special case are still unknown. The responsible forces for the lateral protein assemblies may range from nonspecific interactions such as electrostatics or specific interactions to complementary binding sites [117]. Many theoretical attempts were developed to extract information on protein-protein interactions from freeze-fracture electron micrographs [118-120]. For example, Pearson et al. used a model based on the free energy as a function of protein separation to determine the correlation length of proteins on the *Acholeplasma laidlawii* membranes [121]. However, the reliability of the extracted information from these models relies mainly on two things; (i) one has to insure that the electron micrographs represent the proteins distribution in the native membrane and no rearrangement occurred upon freezing, and (ii) to insure that the particles in the micrograph represent one kind of proteins and one kind of interactions. Nevertheless, a direct measurement of the correlation between membrane proteins is still missing.

Recently, the correlation of self-assembled tobacco mosaic viruses (TMVs), a rod-like particle that is 300 nm long and 18 nm in diameter, was determined by grazing incidence X-ray small angle scattering (GISAXS) at the oil-water interface [122] and on lipid monolayer at the solid-liquid interface [123]. More recently, Fukuto et al characterized the structure of 2D streptavidin crystals on the lipid monolayer using grazing incidence X-ray diffraction [124]. In contrast to diffraction studies on protein crystals, this study focuses on the lateral correlation between non-crystalline neutravidin (NA) proteins on the membrane surface by GISAXS.

In this chapter, a model system for the surface of cells coated with densely packed non-crystalline proteins is created by functionalizing the surface of phospholipid membranes with biotinylated lipid anchors that bound to NA proteins (see Section 3.2.2.3). In principle, the structure of the system perpendicular and parallel to membrane surface at

the air-water interface is studied using specular X-ray reflectivity (XRR) and GISAXS. In the first step, the vertical structure of the membrane before and after NA coupling is characterized by XRR. In the second step, GISAXS measurements are carried out to probe the lateral structure and the inter-molecular correlation of membrane-anchored proteins. In the last step, grazing incidence X-ray fluorescence (GIXF) is utilized to determine the surface density of proteins on the membrane surface from the sulfur fluorescence emission.

4.1 Structure of proteins anchored on membrane surfaces

Prior to X-ray experiments, the pressure-area isotherm of SOPC doped with 5 mol% DOPE-biotin lipids was recorded (Fig. 4.1, left). X-ray scattering measurements were performed at the surface pressure of π = 20 mN/m (green dashed line in Fig. 4.1, left) where the area per lipid molecule is A_l = 75 Å^2. The global shape of the pressure-area isotherm indicates that the lipid monolayer is in the liquid-expanded phase (π ~ 5-40 mN/m). However, the compressibility modulus κ^{-1} (inverse of the isothermal compressibility) can be used to characterize the actual phase of the lipid monolayer. The compressibility modulus is given as [125],

$$\kappa^{-1} = -A_l\left(\frac{\partial \pi}{\partial A_l}\right)_T \tag{4.1}$$

For liquid-expanded phase the compressibility modulus takes the values within the range from 12.5 to 50 mN/m, while for liquid-condensed phase it ranges from 100 to 250 mN/m [126-127]. The compressibility modulus is plotted versus the surface pressure in Fig. 4.1 (right bottom). κ^{-1} resches the value of 50 mN/m at a surface pressure of π ~ 25 mN/m and stays below 100 mN/m for the whole presented range indicating that the lipid monolayer is in the liquid-expanded phase.

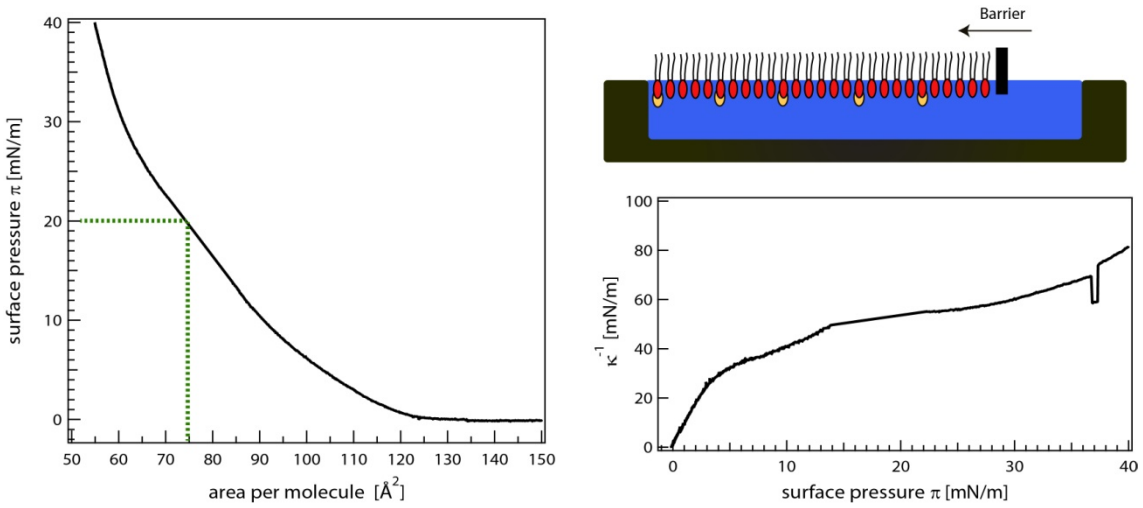

Fig. 4.1 *(Left) the pressure- area isotherm of SOPC / % mol% DOPE-biotin monolayer. The green dashed line indicates the average are per lipid molecules where XRR, GISAXS and GIXF measurements have been carried out. (Right top) Schematic illustration of lipid monolayer deposited onto Langmuir film balance. (Right bottom) compressibility modulus is plotted versus surface pressure.*

The lipid monolayer was spread into a self-made Langmuir film balance and compressed to a surface pressure of π = 20 mN/m. XRR was carried out after incubating the lipid monolayer for more than 20 min to allow the evaporation of organic solvents (see section 3.2.2.3). The XRR curve of the monolayer of SOPC doped with 5 mol% DOPE-biotin is shown in Fig. 4.2A together with best fit matching the experimental data represented in solid red line. The electron density profile perpendicular to the sample surface reconstructed from the fit is presented in Fig. 4.2A. In the reflectivity analysis the slab model was used to represent the system of study with two slabs; hydrocarbon chains and head group. During the refinement of the reflectivity analysis, the electron density of the bulk buffer is set constant to ρ_{Buff} = 0.336 è.Å^{-3}. The parameters corresponding to the best fit results are summarized in table 4.1. The hydrocarbon chains layer has a thickness of d_A = 10.9 Å with rms roughness at the air-chain interface, $\sigma_{air/A}$=3.1 Å. The head group layer has a thickness of d_H = 8.6 Å and the roughness at the head group/water interface is $\sigma_{H/w}$ = 3.4 Å. The obtained electron density of unsaturated and thus disordered hydrocarbon chain ρ_A = 0.233 è.Å^{-3} is lower than those reported for phospholipids with saturated chains, ρ_A = 0.32 – 0.33 è.Å^{-3} [128] [129].

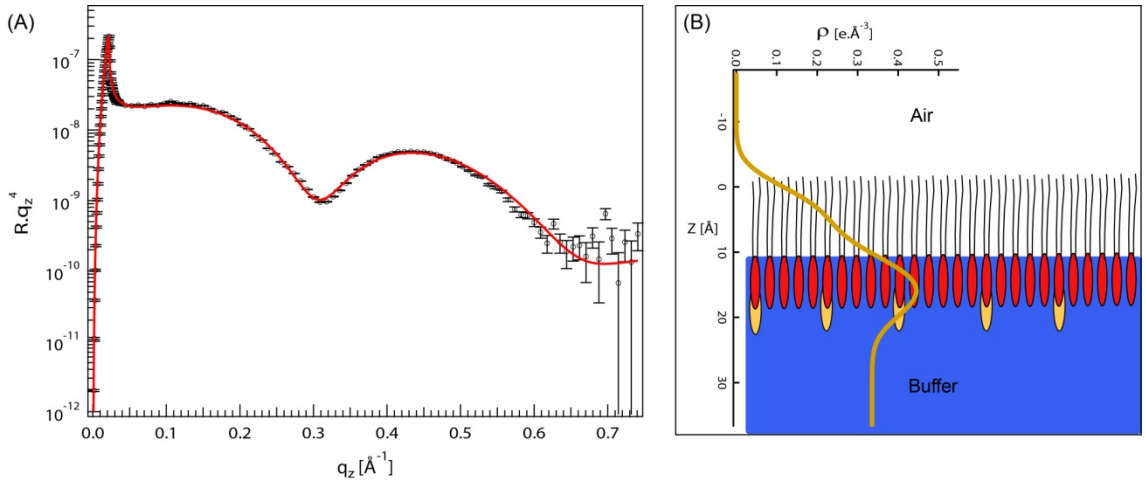

Fig. 4.2 *(A) XRR of SOPC monolayer doped with 5 mol% DOPE-biotin at the air/water interface (points). The best fit is shown as a solid red line. (B)The reconstructed electron density profile perpendicular to the sample surface is shown together with a sketch of the lipid monolayer.*

In fact, our results are in good agreement with the previous report on pure SOPC monolayers measured at π = 24 mN/m [130], d_A = 10.6 Å and $\sigma_{air/A}$ = 3.3 Å for hydrocarbon chain and d_H = 8.7 Å and $\sigma_{H/w}$ = 3.6 Å for head group, respectively. Moreover, the obtained total monolayer thickness (19.5 Å) is also fully consistent with one half of the thickness of phospholipid bilayers, 19.5 – 19.8 Å [131-132]. Furthermore, the average number of electrons N_e per one phospholipid molecule can be calculated as

$$N_e = A_l(d_A.\rho_A + d_H.\rho_H) \tag{4.2}$$

Substituting the values from the parameters in table 4.1 yields N_e = 498 è which is comparable with average calculated one of 445 è from the molecular formula of SOPC and DOPE-biotin. The XRR curve 5 hours after the injection of NA and the best fit result are presented in Fig. 4.3A, and the reconstructed electron density profile is given in Fig. 4.3B. As presented in the figure, the binding of NA to the membrane resulted in a significant change in the global shape of the XRR curve. It should be noted that the change in the global shape of reflectivity curves is not caused by the non-specific adsorption of NA to the interface, because: (i) in the absence of a lipid monolayer, the surface pressure of a NA solution remained zero, and (ii) in the presence of a lipid monolayer doped with DOPE-biotin, the increase in the surface pressure after NA injection is less than 1 mN/m. This

confirms that the amount of NA at the air-water interface is negligibly small in the absence of lipid monolayer.

However, to evaluate the change in the membrane fine structure caused by NA binding, the parameters of the membrane lipid monolayer obtained from the fit prior to the protein injection (table 4.1) were used as starting values during the fitting. Constrains were made with reasonable margin (~ ± 1 Å) to detect the protein binding on the lipid monolayer. The parameters corresponding to the best fit results are summarized in table 4.1.

The thickness of the NA layer was found to be d_{NA} = 47.8 Å perpendicular to the sample surface with an interfacial roughness of $\sigma_{NA/w}$ = 7.4 Å at the NA / water interface. This value is reasonable, based on the value which was measured by X-ray crystallography for dry NA with d_{NA} ~ 40 Å [133]. The higher value obtained here can be understood in terms of the hydration of the NA protein. The binding of NA resulted in a decrease in the thickness of alkyl chains (Δd_A = -1.4 Å) and an increase in the electron density (3 %). The latter can be attributed to the displacement of water molecules by the protein. It should be noted that the roughness of the hydrocarbon chains / head group interface is 3.4 Å and 3.8 Å in the absence and presence of NA, respectively.

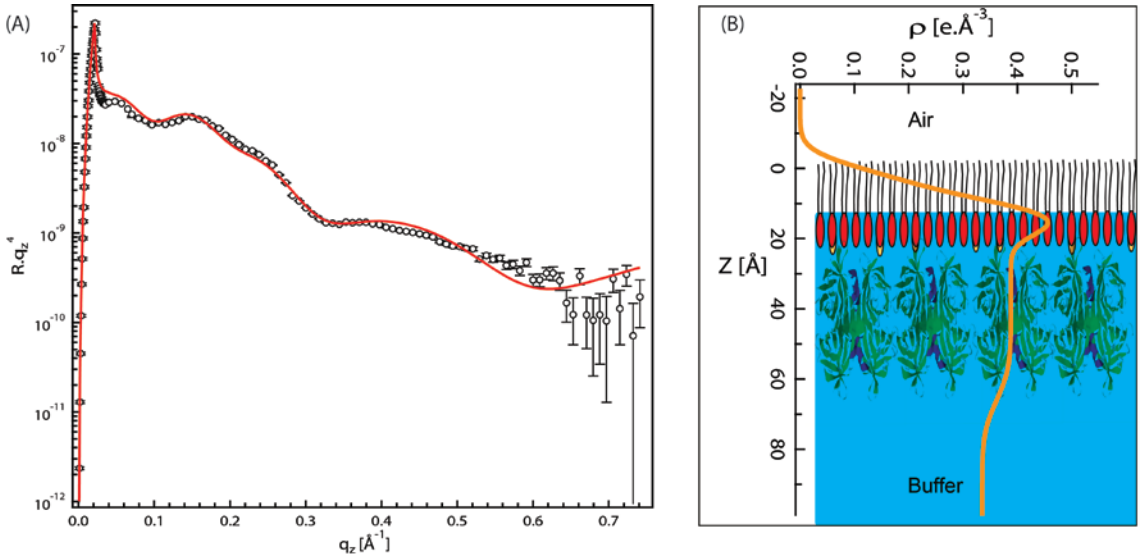

Fig. 4.3 *(A) XRR of the SOPC/ 5 mol% DOPE-biotin monolayer after the coupling of NA proteins. The best fit is shown in a solid red line. (B The reconstructed electron density profile perpendicular to the sample surface is shown together with a sketch of the studied system.*

The volume fraction of the protein within the layer can roughly be estimated from the measured electron density of the protein layer (ρ_{tot} = *0.388* è. Å^{-3}, table 4.1):

$$\rho_{tot} = \rho_{dryNA}\phi + (1-\phi)\rho_{H_2O} \tag{4.2}$$

where ϕ is the volume fraction of protein, ρ_{tot} the total electron density of the protein layer, ρ_{dryNA} the electron density of the dry protein with no hydration water and ρ_{H_2O} the electron density of water. The volume of the protein can be well estimated from its amino acid sequence by summing up the volume of individual amino acids, since the volume change upon folding is less than 0.5% [134-135]. Taking the sequence from crystallographic data (PDB:1AVE), the volume of NA can be estimated to be around 69300 Å^3 , which enables one to assume the electron density of dry protein to be $\rho_{dry} = 0.441$ è.Å^{-3}. This yields the volume fraction of NA $\phi = 50\%$ within the protein layer. The calculated volume fraction of NA is smaller than that of bacterial surface (S-layer) proteins that crystallize on lipid monolayer surfaces, $\phi \geq 60\%$ [129]. Nevertheless, it should be noted that the volume fraction estimated from the reflectivity may be overestimated due to the large roughness of the protein / water interface.

Table 4.1. Parameters for SOPC monolayer doped with 5 mol% DOPE-biotin in the absence [Fig. 4.2] and presence of NA [Fig. 4.3].

SOPC with 5 mol% DOPE-biotin

	d [Å]	ρ [è. Å^{-3}]	σ (Å)
Hydrocarbon chains	10.9	0.233	$\sigma_{air/A} = 3.1$
Head group	*8.6*	*0.478*	$\sigma_{H/w} = 3.4$

SOPC with 5 mol% DOPE-biotin in the presence of NA

	d [Å]	ρ [è. Å^{-3}]	σ [Å]
Hydrocarbon chains	9.5	0.234	$\sigma_{air/A} = 4.4$
Head group	8.8	0.493	$\sigma_{H/NA} = 3.3$
Neutravidin	*47.8*	*0.388*	$\sigma_{NA/w} = 7.4$

4.2 Correlation between membrane-anchored proteins

After the confirmation of NA binding to the lipid monolayer by XRR, GISAXS experiments were carried out as described in section 3.2.2. The 2-dimensional detector readout of GISAXS intensities from the membrane before and after NA coupling are shown in Fig. 4.4(left) and (right), respectively. Fig. 4.5A represents GISAXS signals around at α_f = 0.2 ° integrated along q_z (between the black dashed lines, Fig. 4.4). The GISAXS signals from lipid monolayer before and after NA binding are indicated in solid squares and circles, respectively. In contrast to the signal in the absence of NA showing no characteristic in-plane features, the GISAXS signal in the presence of NA exhibited a prominent shoulder at around q_y = 0.092 Å^{-1} corresponding to a characteristic distance of < d > = 68 Å. Fig. 4.5B shows the GISAXS signal of the sample with NA surface after the background subtraction.

The GISAXS intensity is given by the combination of the structure (green line, Fig. 4.5B) and form factor (blue line, Fig. 4.5B), and according to equation 2.42 the GISAXS intensity can be written as:

$$I(q) = A\left|F(q,D,H)\right|^2 . S(q,D_{hs},\eta_{hs}) . \qquad (4.3)$$

A is a scale factor, *F(q,D,H)* the form factor of NA which is approximated by a cylinder shape with a diameter *D* and height *H*. *F(q,D,H)* is calculated within the distorted wave Born approximation (DWBA) (see section 2.4 and Appendix A.1) [79, 81]. $S(q,D_{hs},\eta_{hs})$ is the structure factor expressed by a two dimensional Percus-Yevick function (equation 2.43) [136]. Within the framework of this model, a protein is described as a hard sphere with a diameter $D_{hs} = C \times D$, where *C* is constant. η_{hs} is the volume fraction of the hard spheres and related to the volume fraction of NA molecules by $\phi = \eta_{hs} / C^3$. Here, the protein "layer" is assumed by sandwiched by two continua using a local monodispersive approximation (see section 2.4.2) [83, 137].

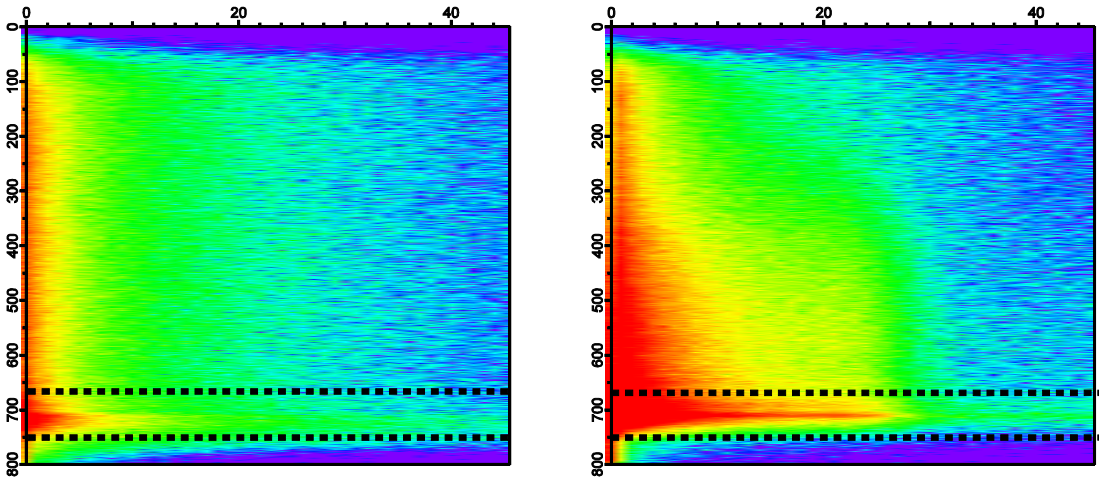

Fig. 4.4 *2-dimensional detector readout of GISAXS intensities from the SOPC/ 5mol% DOPE-biotin monolayer before (left) and after (right) NA binding. The axis labels are given in pixels. The GISAXS signal as a function of q_y is integrated between black dashed lines.*

The parameters which describe the layers were taken from the reflectivity results in table I and fixed during the GISAXS modeling. The diameter of a cylindrical particle (NA) obtained from the GISAXS fit is *D* = 57 ± 1 Å, which shows good agreement with that obtained from dry NA crystals, *D* ~ 53 Å [133]. Moreover, the height of a NA molecule calculated from the GISAXS, *H* = 52 ± 2 Å, is close to the thickness of NA layer determined by XRR in this study, d_{NA} = 47.8 Å.

The peak position of the combined structure- and form factors can be found at $q_{y\text{-}p}$ = 0.085 $Å^{-1}$, corresponding to an inter-particle distance of < d > = 74 Å. Revenant et al. [42] suggested that the exact mean inter-particle distance lies between this value and the one calculated directly from the peak position of the measured GISAXS signal (68 Å).

Table 4.2. Summary of the parameters for the GISAXS fit results [Fig. 4.5B].

D [Å]	H [Å]	$q_{y\text{-}p}$ [$Å^{-1}$]	< d > [Å]
57 ± 1	52 ± 2	0.085	74

In the case of commonly studied inorganic nanoparticles, the width of the Bragg peak can be attributed to the polydispersity of the particles and/or to the structure factor. In our system, the width of the Bragg peak is dependant on the structure factor, as the size (and thus molecular weight) of the protein molecules is highly monodisperse. Therefore, the full width at half maximum δq_y of the peak obtained from the subtraction of the GISAXS signal in the presence and absence of NA (in the inset of Fig. 4.5A) can be used to calculate the correlation length ξ. This is the characteristic length scale over which the correlation between particles can reach and can be calculated using the Scherrer formula $\xi = 2\pi/\delta q_y$ [138]. The obtained value from the inset of Fig. 4.5A, ξ = 20 nm, suggests that the correlation between non-crystalline NA molecules can reach a distance that is about three times larger than the average intermolecular distance.

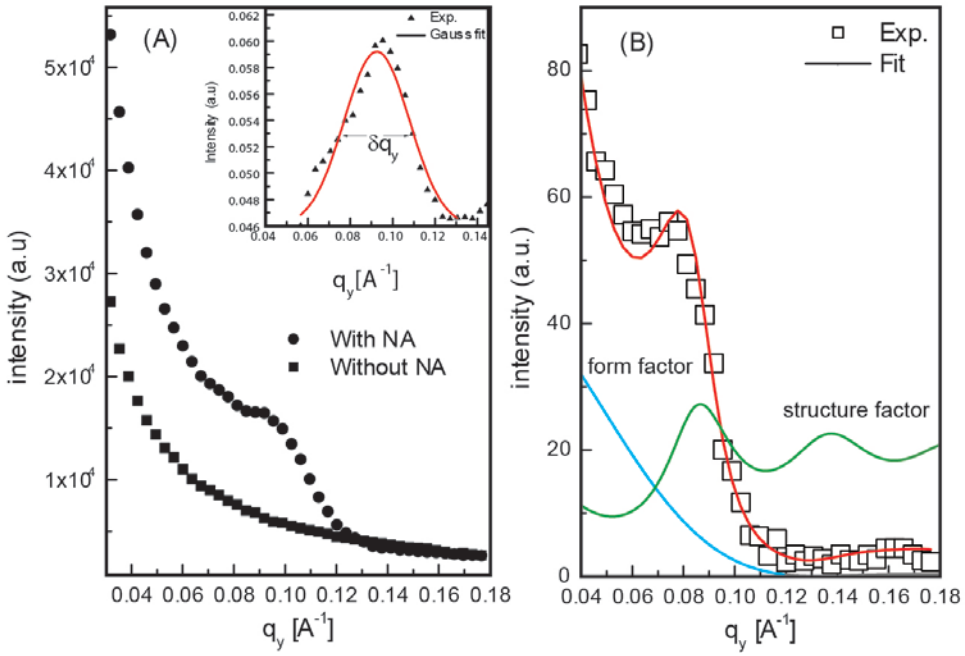

Fig. 4.5 *(A) The measured GISAXS signals of the SOPC/DOPE-biotin monolayer before (solid squares) and after (solid circles) the NA binding. The inset shows the Gaussian fit (red line) of the difference in the GISAXS signals. (B) The GISAXS intensity of the same monolayer with NA after subtraction of the background (open squares). The combined fit (red line) coincides with the combination of the form factor (blue lines) and the structure factor (green line).*

4.3 Lateral density of membrane-anchored proteins

In order to confirm and support the obtained results from GISAXS experiments, GIXF experiments were performed to determine the lateral density of NA proteins bound to lipid monolayer at the air-water interface through the fluorescence emission from their sulfur contents (Fig. 4.6). Fig. 4.7 shows the X-ray fluorescence spectra of the blank buffer (top) and the SOPC/DOPE-biotin after the NA binding (bottom). For each dataset, the fluorescence spectra measured below and above the critical angle α_c = 0.125° are presented as solid and dotted lines, respectively. As indicated by arrows, two characteristic spectral features can be found for the monolayer functionalized with NA; sulfur K_α peak at 2.3 keV, and phosphorus K_α peak at 2.0 keV. The former signal is from the amino acid containing sulfur, while the latter from phosphate head groups of lipids. The fluorescence contribution from S K_α line was extracted using a multiple-Gaussian peak fitting routine with a self-written code For Igor Pro (see section 3.2.3). In the inset,

the fluorescence intensities from S K_α line are plotted as a function of q_z. The open circles represent the signal from the blank buffer, while the solid circles the S K_α signal from the membrane with NA. The global shape of the plot of S K_α from the blank buffer is similar to the ones of K K_α recorded from blank buffers [40, 139].

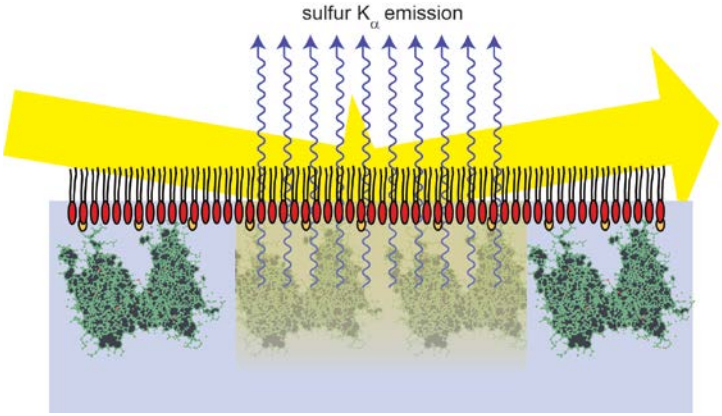

Fig. 4.6 *Sulfur K_α fluorescence emission from NA proteins bound to lipid monolayer at the air-water interface. The sulfur atoms within NA proteins are indicated by red dots.*

The normalization of the measured fluorescence intensity by the signal from the blank buffer enables one:

1) To detect small changes in ion concentration near the interface [139].

2) To gain a higher spatial resolution [40].

3) To eliminate undefined geometrical effects.

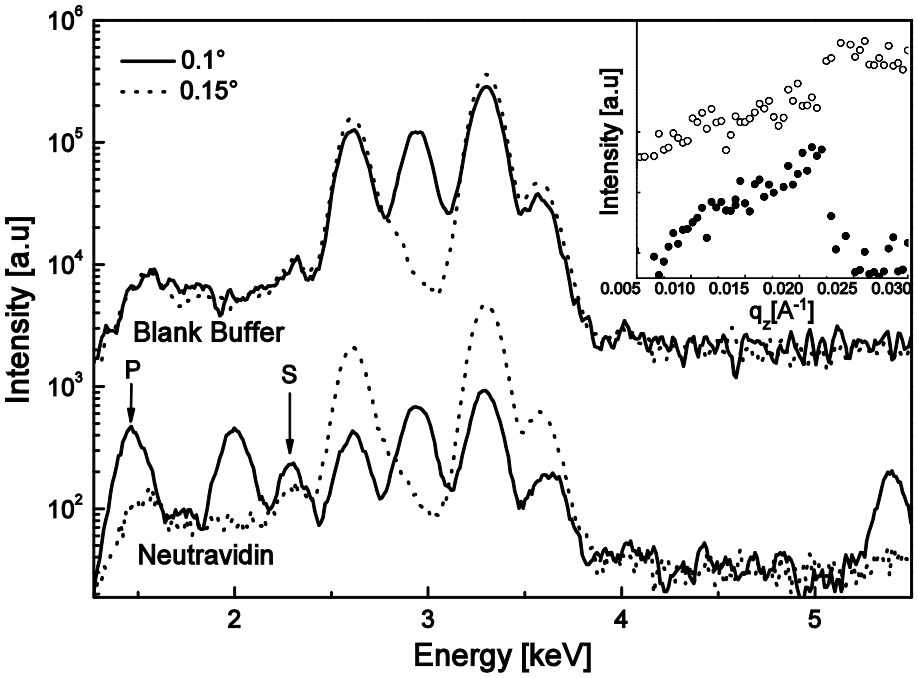

Fig. 4.7 *GIXF spectra of blank buffer (top) and monolayer with NA (bottom) recorded at angles of incidence below (solid lines) and above (dotted lines) the critical angle of incidence $\alpha_c = 0.125°$. The spectra from the blank buffer are shifted vertically for clarity. NA molecules coupled to the lipid head group can be detected by S K_α peak at 2.3 keV. The inset shows the fluorescence intensities of S K_α peak as a function of q_z., The signal from the blank buffer and that from the lipid monolayer with NA are presented as open and solid curcles, respectively.*

Fig. 4.8 represents the S K_α fluorescence signal from the lipid monolayer with NA after the normalization by the intensity from the blank buffer (open circles). The intensity of S K_α is remarkably higher than the bulk level below the critical edge (q_c = 0.022 Å^{-1}). A significantly higher intensity below the critical angle of incidence (4 – 6 times higher than the bulk level) implies the enrichment of sulfur near the air-water interface, which can be attributed to cysteine and methionine in NA. To model the fluorescence signal we assumed an asymmetric Gaussian profile [40] for the sulfur distribution in NA attached to the head group of the lipids (equation 2.51). Here, the concentration profile starts from the Alkyl chains / head group interface, $z_{HC} = d_A$ = 9.5 Å, which is determined by XRR (table 4.1). The bulk concentration was set constant to 5 mM, corresponding to the concentration of Hepes in the subphase. The variation of sulfur concentration near the interface (solid lines)

results in a clear shift in the intensity below the critical edge q_c = 0.022 Å^{-1}. The concentration profile corresponding to the best matching fit to the experimental results is presented in the inset of Fig. 4.8. Integrating the concentration under the curve yields a lateral concentration of sulfur atoms of (4.7 ± 0.2) × 10^{-11} mole/cm^2. If one takes the area per lipid molecule A_{lipid} = 75 Å^2 (see the pressure-area isotherm in section 4.1) and the fact that NA is a tetrameric protein with four sulfur atoms per subunit [140], one can estimate the lateral concentration of NA to be (2.2 ± 0.2) × 10^{-12} mole/cm^2. The area per one NA molecule calculated from the surface concentration A_{NA} = 7510 ± 350 Å^2 yields an intermolecular distance of 86.5 ± 2 Å. This value is in a good agreement with the interparticle separation calculated from the GISAXS analysis, 68 – 74 Å.

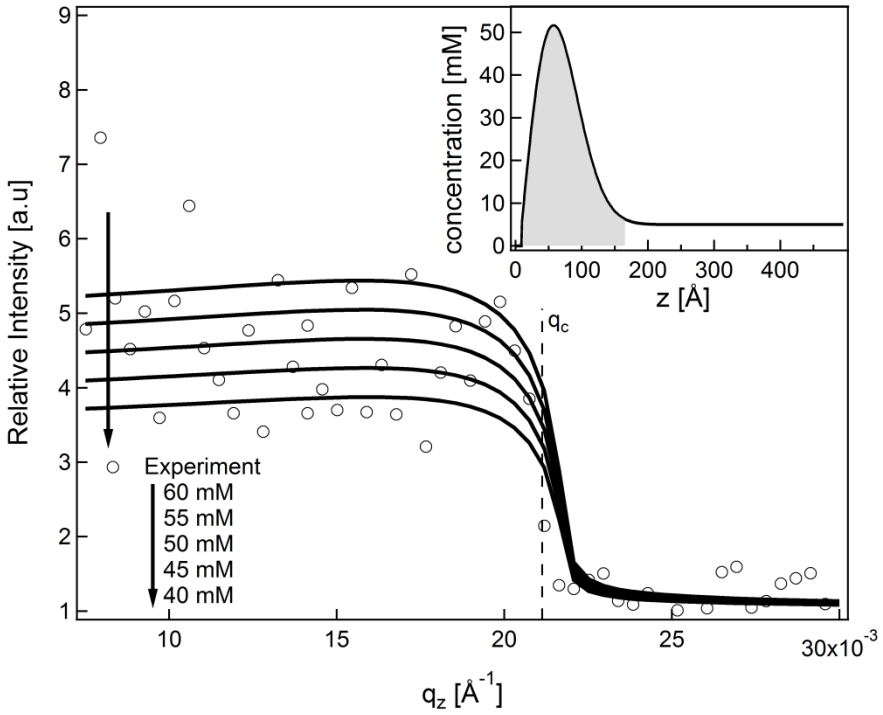

Fig. 4.8 *The normalized S Kα signal (2.3 keV) from the monolayer functionalized with NA plotted as a function of q_z (open circles). The modeled fluorescence intensities corresponding to different lateral concentrations are presented by solid lines according to equation 2.45. The inset shows the concentration profile corresponding to the best fit.*

5. Lateral Diffusion of Membrane-Anchored Proteins

As motivated in chapters 1 and 2 that in lower eukaryotes, GPI-anchored proteins are among the most abundant cell-surface proteins that are responsible for cell viability and defense against the host immune system [16]. Recently a study suggested that the swimming of trypanosome causes directional movement of antibody-VSG complex in the plasma membrane. This cellular motility enables the clearance and sorting of antibody-VSG complex at the posterior cell [23].

For this reason a two models for GPI-anchored proteins were created in this chapter. The first system is made by binding of neutravidin (NA) proteins into solid-supported lipid bilayer. In second system, the variant surface glycoprotein (VSG) which forms a dense coat for the *Trypanosoma brucei* is incorporated into solid-supported bilayer. In the first step, each system is characterized by X-ray reflectivity to confirm the coupling / incorporation of the proteins into the lipid bilayer and to investigate their structure. In the next step, the ensemble diffusion coefficient and mobile fraction as a function of proteins lateral density are determined by fluorescence recovery after photobleaching (FRAP). Eventually, the diffusion coefficient of individual protein molecules on the membrane surface is investigated by single particle tracking (SPT) on sub-micron length scale.

5.1 The structure of membrane-anchored protein

5.1.1Structure of neutravidin proteins bound to membrane lipid bilayer

The membrane bilayer was prepared by depositing SOPC doped with 5 mol% DOPE-biotin lipids as described in section 3.2.2. The membrane bilayer is then characterized by XRR. In the next step, NA proteins were injected into the system and incubated for more than 12 hours. Fig. 5.1A shows the XRR results of the membrane bilayer of SOPC doped with 5 mol% DOPE-biotin together with best matching fit indicated by solid red line. For the refinement of the experimental data the slab model was used with five slabs; outer headgroup, hydrocarbon chains, inner head group, water layer and Si-oxide layer.

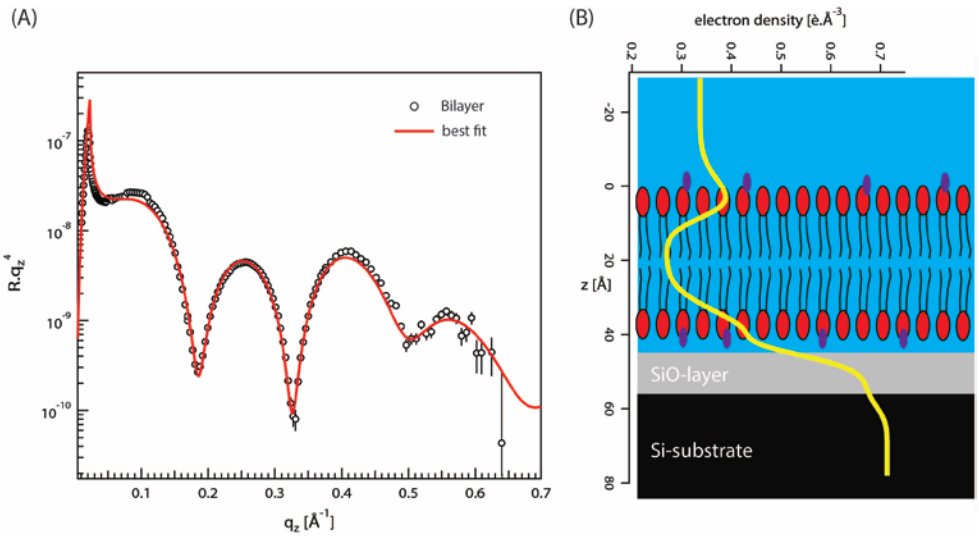

Fig. 5.1 *(A) XRR of SOPC / 5 mol% DOPE-biotin bilayer at the solid-liquid interface (black open circles). The best fit is shown as a solid red line. (B)The reconstructed electron density profile perpendicular to the sample surface is shown together with schematic illustration of the solid-supported membrane bilayer.*

Fig. 5.2B shows the reconstructed electron density profile normal to the membrane surface together with an illustration of the solid-supported bilayer indicating each slab. The parameters corresponding to the best fit results are summarized in table 5.1. The total membrane thickness (d_{tot} = 40.9 Å) and electron density of each layer (ρ_{oh} = 0.426 è.Å^{-3}, ρ_{ih} = 0.46 è.Å^{-3}, ρ_{chains} = 0.27 è.Å^{-3}) is fully consistent with corresponding values reported for phospholipid bilayers; d_{tot} = 39 - 41.2 Å, $\rho_{oh} = \rho_{ih}$ = 0.43 – 0.45 è.Å^{-3} and ρ_{chains} = 0.23 – 0.25 è.Å^{-3},respectively [132, 141-143]. In addition, the thickness of the thin water layer (d_w = 3.7 Å) between the membrane and the solid substrate is consistent with previously reported values (d_w ~ 4 Å) [132, 142-143]. The inner head group has electron density (ρ_{ih} = 0.46 è.Å^{-3}) is higher than that of the outer head group (ρ_{oh} = 0.426 è.Å^{-3}) indicative of lower water content in the inner head group. The thickness of the outer head group (d_{oh} = 8.3 ± 0.5) is found to be larger than that of the inner head group (d_{ih} = 7.3 ± 0.6). This finding is in agreement with the reduction of fluctuations of the inner leaflet of the bilayer due to interactions with the substrate [144-145]. However, using the parameters in table 5.1 for the membrane bilayer and the chemical formula of SOPC and DOPE-biotin molecules one can determine the average area per lipid molecule A_l in the bilayer as:

$$A_l = 2N_e / (d_{oh} \cdot \rho_{oh} + d_{chains} \cdot \rho_{chains} + d_{ih} \cdot \rho_{ih}) \qquad (5.1)$$

Substituting the values from table 5.1 and the fact that the average number of electrons per lipid molecule is N_e = 445 è, yields an area per lipid of A_l = 65 Å^2. This value is known for phospholipid bilayers in the liquid expanded phase [54-55]. These findings indicate the full coverage and homogeneity of the membrane lipid bilayer deposited into solid support.

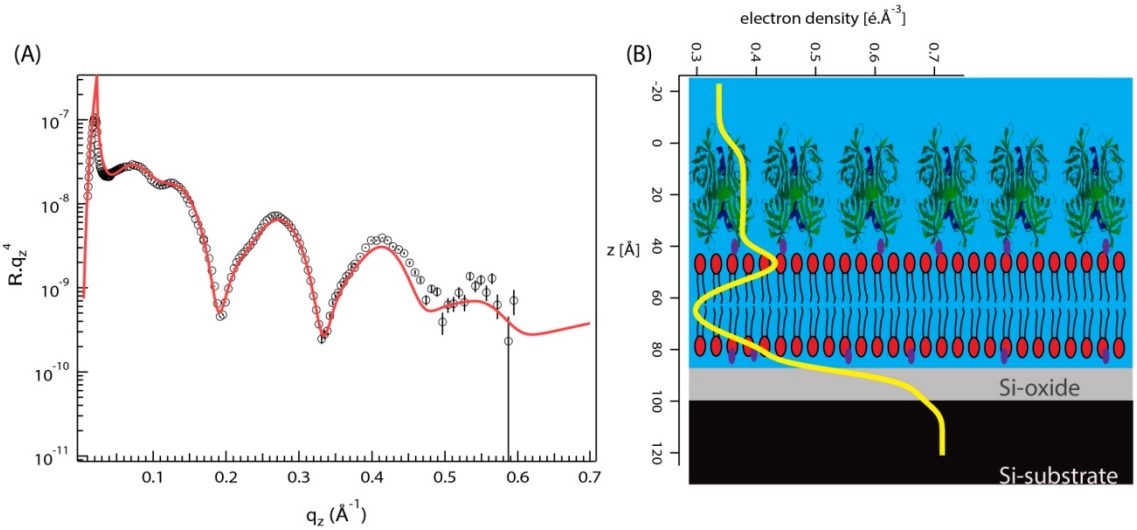

Fig. 5.2 *(A) XRR of NA bound to SOPC / 5 mol% DOPE-biotin bilayer at the solid-liquid interface (black open circles) together with the best fit is shown as a solid red line. (B) The reconstructed electron density profile perpendicular to the sample surface.*

The XRR curve after the coupling of NA onto membrane bilayer is shown in Fig. 5.2A. The best fit is represented by solid red line. The corresponding electron density profile normal to the membrane surface is shown together with a drawing of the studied system. The parameters corresponding to the best matching fit to the experimental data are summarized in table 5.1. As it can be seen from Fig. 5.2A, the binding of NA to the membrane resulted in a significant change in the global shape of the XRR curve compared to Fig 5.1A prior NA injection. The thickness of the NA layer was found to be d_{NA} = 48.3 Å perpendicular to the sample surface which is consistent with the value reported for NA bound to lipid monolayer at the air-water interface in the previous chapter (d_{NA} = 47.8 Å).

Table 5.1. *Summary of the thickness d, electron density ρ and interfacial roughness σ corresponding to the best fits of the XRR data of Fig. 5.1 and Fig. 5.2. The errors are standard deviations from the error propagation of the fit.*

	d [Å]	ρ [è.Å^{-3}]	σ [Å]
Before neutravidin binding			
Outer head group	d_{oh} = 8.3 ± 0.5	ρ_{oh} = 0.426 ± 0.009	5.6 ± 0.8
Hydrocarbon chains	d_{chains} = 25.3 ± 0.5	ρ_{chains} = 0.270 ± 0.006	3.5 ± 0.9
Inner head group	d_{ih} = 7.3 ± 0.6	ρ_{ih} = 0.460 ± 0.014	5.4 ± 0.3
Water layer	d_w = 3.7 ± 0.3	ρ_w = 0.334	2.4 ± 0.4
After neutravidin binding			
neutravidin	d_{NA} = 48.3 ± 6.3	ρ_{NA} = 0.380 ± 0.014	4.5 ± 1.5
Outer head group	d_{oh} = 7.8 ± 0.8	ρ_{oh} = 0.532 ± 0.019	4.2 ± 0.7
Hydrocarbon chains	d_{chains} = 25.1	ρ_{chains} = 0.278 ± 0.014	4.9 ± 0.1
Inner head group	d_{ih} = 7.2	ρ_{ih} = 0.460	6.4 ± 0.8
Water layer	d_w = 4	ρ_w = 0.334	3
Substrate			
SiO-layer	*14.9*	*0.670*	*3.8*
Si-substrate	∞	*0.713*	*3.4*

The parameters of the membrane bilayer after NA injection stayed similar to the values prior NA injection except an increase in the electron density of the outer head group after NA injection. The later is attributed to the displaced water molecules from the outer head group upon NA binding. However, these findings confirm the binding of NA to the outer leaflet of the membrane. The volume fraction of NA within the protein layer can be estimated from the measured electron density of the protein layer using equation 4.3. This yields the volume fraction of NA $\phi = 42\%$ within the layer. The calculated volume fraction of NA is smaller than the value found for NA in the previous chapter $\phi = 50\%$. This difference is expected since the volume fraction estimated from the reflectivity is overestimated due to the roughness of the protein/water interface. In this case, NA has an interfacial roughness of $\sigma_{NA/W}$ = 4.5 Å and $\sigma_{NA/W}$ = 7.4 Å for NA at the air-water interface. However, The volume fraction of NA in both cases is smaller than that of bacterial surface (S-layer) proteins that crystallize on lipid monolayer surfaces, $\phi \geq 60\%$ [129]

5.1.2 Structure of VSG incorporated into membrane lipid bilayer

The membrane bilayer was prepared by depositing SOPC lipids into Si-substrate. In the second step, VSG proteins were added to membrane bilayer and incubated for more than 12 hours to allow the incorporation of VSGs with high lateral density (see section 3.2.2). In each step, XRR measurements were performed to study the fine-structure perpendicular to the sample surface. The XRR results for SOPC membrane bilayer before (black solid triangles) and after the injection of VSG proteins (green solid squares) are presented in Fig 5.3A together with their best fits indicated in solid lines.

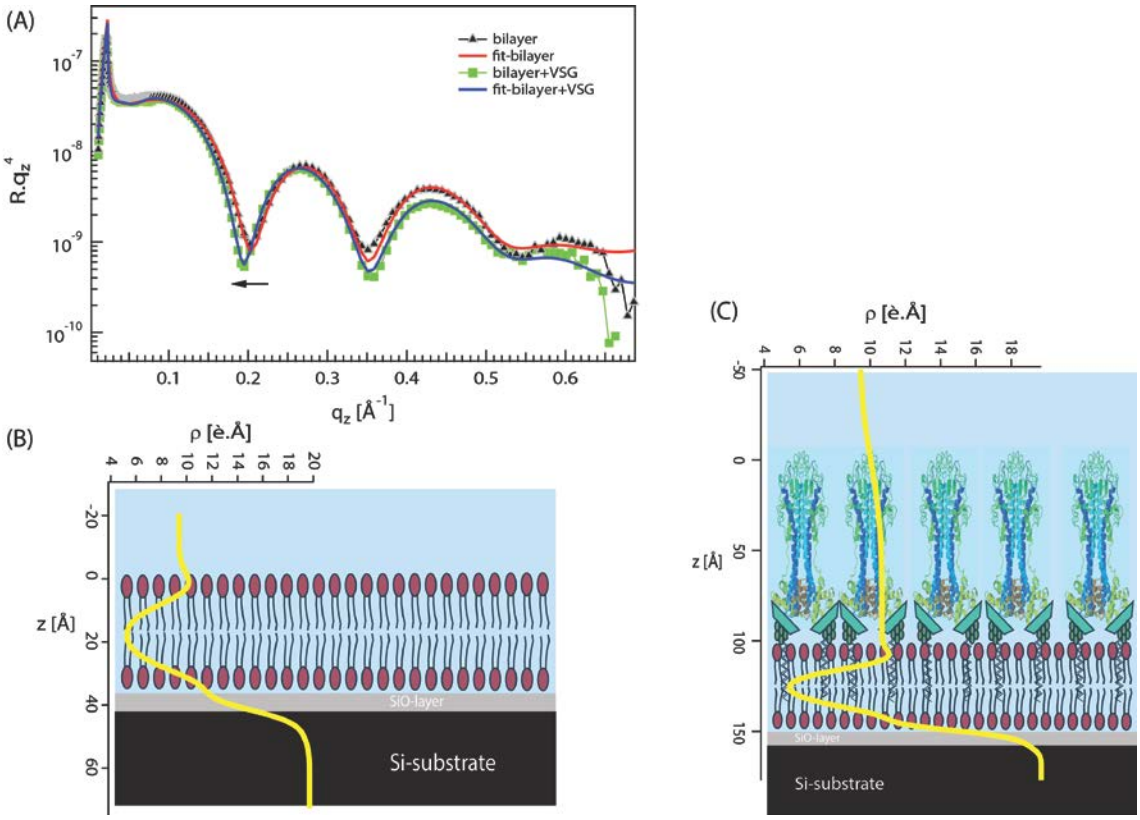

Fig. 5.3 *(A) XRR curves of SOPC bilayer before (black solid triangles) and after (green solid squares) VSG injection together with the best fits represented in red and blue solid lines, respectively. (B) The reconstructed electron density profile normal to the membrane surface before VSG injection. (C) The reconstructed electron density profile perpendicular to the membrane surface after VSG incorporation into SOPC bilayer.*

The reconstructed electron density profiles of the membrane before and after the incorporation of VSG proteins are shown in Fig. 5.3B and Fig 5.3C, respectively. The parameters corresponding to the best fit results are summarized in table 5.2. Using equation 5.1 in the previous section yields an area per SOPC lipid of A_l = 75 Å^2. Comparing the bilayer parameters in table 5.1 and the corresponding values in the previous section confirms the full coverage of the solid substrate with SOPC bilayer. The incorporation of VSG proteins into the membrane resulted in a shift of the first minima toward lower q_z value as indicated in the arrow in Fig 5.3A.

Table 5.2. *Summary of the thickness d, electron density ρ and interfacial roughness σ corresponding to the best fits of the XRR data of Fig. 5.3. The errors are standard deviations from the error propagation of the fit.*

	d [Å]	ρ [è.Å^{-3}]	σ [Å]
Before VSG incorporation			
Outer headgroup	d_{oh} = 8.2 ± 0.5	ρ_{oh} = 0.398 ± 0.011	3.2 ± 0.8
Hydrocarbon chains	d_{chains} = 21.5 ± 0.6	ρ_{chains} = 0.213 ± 0.023	4.8 ± 0.4
Inner headgroup	d_{ih} = 7.7 ± 0.6	ρ_{ih} = 0.486 ± 0.028	5.1 ± 0.5
Water layer	d_w = 3.7 ± 0.5	ρ_w = 0.334	2.9 ± 0.5
After VSG incorporation			
VSG	d_{VSG} = 107 ±18.7	ρ_{VSG} = 0.379 ± 0.007	29.4 ± 5.2
Outer headgroup	d_{oh} = 7.1 ± 2.6	ρ_{oh} = 0.453 ± 0.048	4 ± 0.2
Hydrocarbon chains	d_{chains} = 22 ± 2.4	ρ_{chains} = 0.213 ± 0.043	5.2 ± 0.1
Inner headgroup	d_{ih} = 8.3 ± 0.8	ρ_{ih} = 0.429 ± 0.017	5.6 ± 0.5
Water layer	d_w = 3.8 ± 1.1	ρ_w = 0.334	2.9 ± 0.1
Substrate			
SiO-layer	9.9 ± 2.1	0.660	3.4 ± 0.5
Si-substrate	∞	0.699	3.3 ± 0.3

The volume fraction of VSG incorporated in the SOPC membrane can be estimated from the measured electron density of the protein layer in table 5.2 (ρ_{NA} = 0.379 ± 0.007) using equation 4.3. The electron density of non-hydrated VSG can be calculated from it amino acid sequence similar to the method used for NA in section 4.2. The volume of VSG is determined to be $V_{VSG} = 64124 \pm 110$ Å^3, which enables one to assume the electron density of dry protein to be $\rho_{dry} = 0.444$ è.Å^{-3}. This yields the volume fraction of VSG $\phi = 41\%$ within the layer. The calculated volume fraction of VSG in this case is overestimated due to the large roughness of the VSG / water interface ($\sigma_{VSG/w}$ = 29.4 ±

5.2 Å). However, This values is comparable to the one found for NA at the air-water interface (section 4.2) indicating the VSG proteins are incorporated into the membrane with high lateral density.

5.2 Lateral diffusion of membrane-anchored proteins in crowded systems

5.2.1 Molecular crowding threshold of membrane-anchored proteins

In order to control the lateral density between NA proteins, membrane bilayer consisting of SOPC and a certain fraction of DOPE-biotin was deposited into a glass substrate (see section 3.2.2). This allows one to control the separation between NA proteins with nm accuracy. The average distance between DOPE-biotin molecules can be estimated by $d \sim \sqrt{A_l / \chi}$, where A_l is the average area per lipid molecule and χ is the fraction of DOPE-biotin in the SOPC bilayer. After the addition of fluorescently labeled NA proteins into the solid-supported membrane, the diffusion coefficient and the mobile faction were measured by fluorescence recovery after photobleaching (FRAP). Fig. 5.4A shows typical FRAP curves of NA proteins for selected cases where NA was bound to SOPC bilayer doped with 0.1 mol%, 1 mol% and 2 mol% DOPE-biotin. The red line represents the fit to the experimental data according to equation 3.3. The obtained values for the mobile fraction and the diffusion coefficient from the fits are plotted against $1/d$ in Fig. 5.4B and Fig. 5.4C, respectively. The dashed red lines in Fig. 5.4B and Fig. 5.4B represent the fit according to:

$$f(c) \sim \frac{1}{1+\exp(c - c_p)} \tag{5.2}$$

Where c is the lateral concentration of NA proteins being proportional to $1/d$ and c_p is the percolation threshold or molecular crowding threshold. The fit to the mobile fraction and diffusion coefficient data yielded a molecular crowding threshold of $c_p \sim 0.145 \pm 0.003 \text{nm}^{-1}$ and $c_p \sim 0.056 \pm 0.003\ \text{nm}^{-1}$ corresponding to an intermolecular separation of d = 6.9 nm and d = 17.9 nm, respectively. Surprisingly, the value found from fit to the mobile fraction curve d = 6.9 nm is surprisingly consistent with the intermolecular separation between NA proteins determined from GISAXS in section 4.3 (d = 6.8 nm).

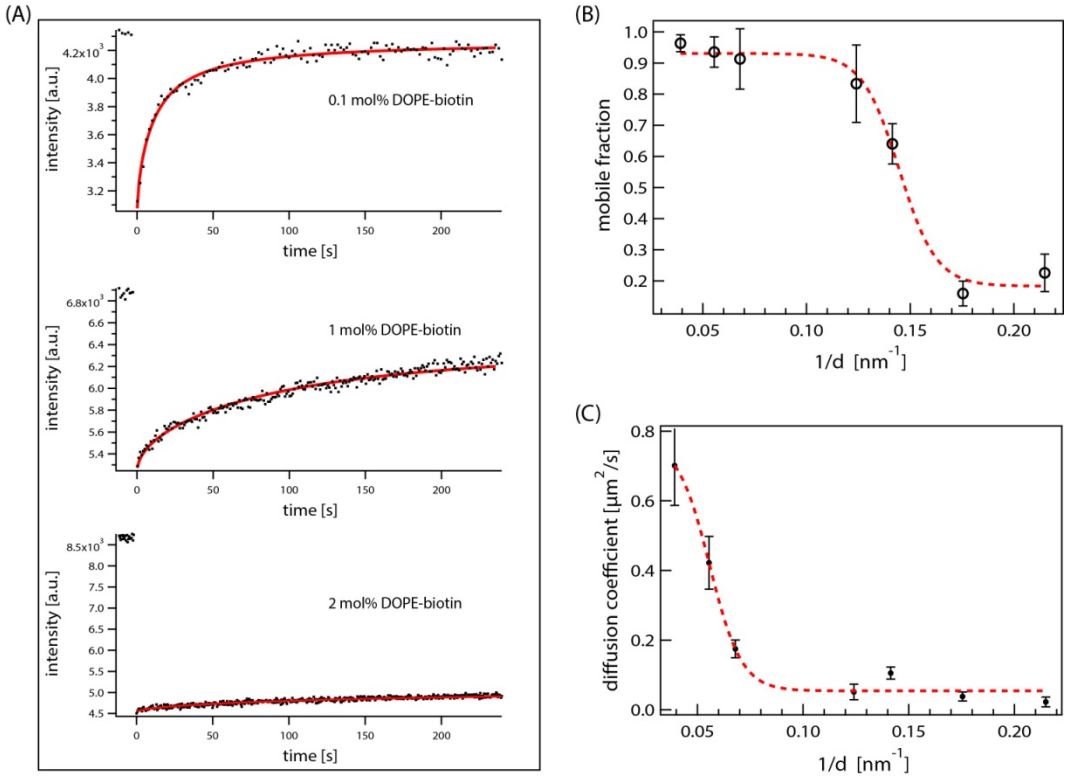

Fig. 5.4 *(A) Typical FRAP curves of NA bound to SOPC doped with 0.1 mol%, 1 mol% and 2 mol% DOPE-biotin (black dots). The red lines indicate the fit of the experimental data according to equation 3.3. (B) The mobile fractions of NA proteins are plotted against the reciprocal average separation between DOPE-biotin molecules. The dashed red line represents a sigmoidal fit to the data (equation 5.2). (C) The diffusion coefficient of NA proteins are plotted against the reciprocal average separation between DOPE-biotin molecules. The dashed red line represents a sigmoidal fit to the data (equation 5.2). The error bars are standard deviations from the experimental errors.*

However, the molecular crowding threshold estimated from the diffusion coefficient data here is not accurate due to the detection limit of FRAP (as it will be shown later in section 5.3.1 that). The value of D drops to below 0.1 μm^2/s at $1/d \sim 0.06$ nm^{-1} (Fig. 5.4C) which is at the detection limit of FRAP. The reduction in the diffusion coefficient upon increasing the lateral density of NA proteins can be understood in terms of the frictional drag exerted to NA molecules. The dimensionless mobility m can be determined from the measured diffusion coefficient D via $m = 4\pi\eta_m D/k_B T$. Since the NA proteins are anchored to the DOPE-biotin lipid at outer leaflet of the membrane, the viscosity of the membrane η_m can be assumed to be one-half of a free lipid bilayer (η_m =

$\eta_{bi}/2$ = 0.08 nN.m^{-1}.s) [65-66, 146]. This enables one to obtain the dimensionless radius ε analytically from Fig. 2.2. Finally, the frictional coefficient b_s can be calculated by the membrane viscosity η_m and the ratio between ε and R_p: $b_s = \eta_m \left(\varepsilon / R_p\right)^2$ where $R_p \sim 5$ Å is the radius of the transmembrane part of the anchored-protein that can be estimated from the area per lipid molecule ($A_l \sim 65$ Å^2). The obtained results for the frictional coefficient were summarized in table 5.3. The calculated frictional coefficient on NA proteins in a crowded state (χ = 2-3 mol%) is $b_s \sim 2\times 10^{11}$ N.s.m^{-3} which is two orders of magnitude higher than NA proteins in diluted state (χ = 0.1 mol%) $b_s \sim 4\times 10^{9}$ N.s.m^{-3}. Therefore, the suppression of free area upon increasing the lateral density of proteins results in a significant increase in the frictional stress exerted on NA proteins.

Table 5.3. Diffusion coefficient D, mobile fraction and the frictional coefficient b_s of NA proteins bound to lipid bilayer doped with χ mole fraction of DOPE-biotin and the corresponding average separation d between DOPE-biotin molecules.

χ [mol%]	d [nm]	D [μm^2/s]	Mobile fraction [%]	b_s [N.s.m^{-3}]
3	4.7	0.023 ± 0.014	23 ± 6	2.37×10^{11}
2	5.7	0.038 ± 0.013	16 ± 4	1.37×10^{11}
1.3	7.1	0.105 ± 0.018	64 ± 7	4.33×10^{10}
1	8.1	0.051 ± 0.022	83 ± 12	9.89×10^{10}
0.3	14.7	0.175 ± 0.026	91 ± 10	2.34×10^{10}
0.2	18.0	0.422 ± 0.076	94 ± 5	7.45×10^{9}
0.1	25.5	0.701 ± 0.114	96 ± 3	3.58×10^{9}

The calculated values of b_s for NA proteins bound to membrane bilayer doped with 0.1 – 1.3 mol% DOPE-biotin lie in the range of $b_s \sim 0.4 - 4 \times 10^{10}$ N.s.m^{-3} which are consistent to the those reported for integrin incorporated into polymer supported membranes ($b_s \sim 3 \times 10^{10}$ N.s.m^{-3}) and about one order of magnitude higher than the values reported for His-tagged proteins ($b_s \sim 5 \times 10^{8}$ N.s.m^{-3}) [65-66].

5.2.2 N-linked glycans reduce the molecular crowding threshold of membrane-anchored proteins[1]

To study the influence of protein glycosylation on it is diffusivity, N-glycosylation have been removed from the wild type VSG proteins (mutant VSG). The VSG proteins (wild type VSG or mutant VSG) were incorporated into solid-supported membrane bilayer as described in section 3.2.2.1. The determined diffusion coefficients and the mobile fractions of wild type VSG (open squares) and mutant VSG (solid squares) as a function of their reciprocal average separation ($1/d$) are shown in Fig. 5.5A and Fig. 5.5B, respectively. The diffusion coefficient of mutant VSG drops to ~ 0 at intermolecular separation of d = 8.7 nm while wild type VSG has a diffusion coefficient at intermolecular separation of d = 5.8 nm (table 5.4 and Fig. 5.5A). This suggests that the molecular crowding threshold for VSG is reduced due to the missing N-glycosylation. The reduction in VSG diffusivity by increasing their lateral density can be understood in terms of the increase of the frictional stress exerted on VSG proteins. The calculated values of the frictional coefficients b_s for VSG proteins are summarized in table 5.4. The diffusivity of VSGs is reduced by removing the N-linked glycans (Fig. 5.5A). In addition, wild type VSGs exhibit higher mobile fraction than that of mutant VSGs (Fig. 5.5B). For instance, at a molecular separation of d = 8.7 nm between mutant VSGs the frictional coefficient is $b_s = 9.35 \times 10^{10}$ N.s.m^{-3}. This value is larger than the frictional coefficient ($b_s = 1.7 \times 10^{10}$ N.s.m^{-3}) for wild type VSGs with an intermolecular distance of d = 5.8 nm. These findings indicate that the N-glycosylation facilities the VSG mobility probably by minimizing the attractive interactions between VSG proteins.

[1] FRAP measurements were performed in cooperation with Andreas Hartel (Department of Cell and Developmental Biology, University of Würzburg)

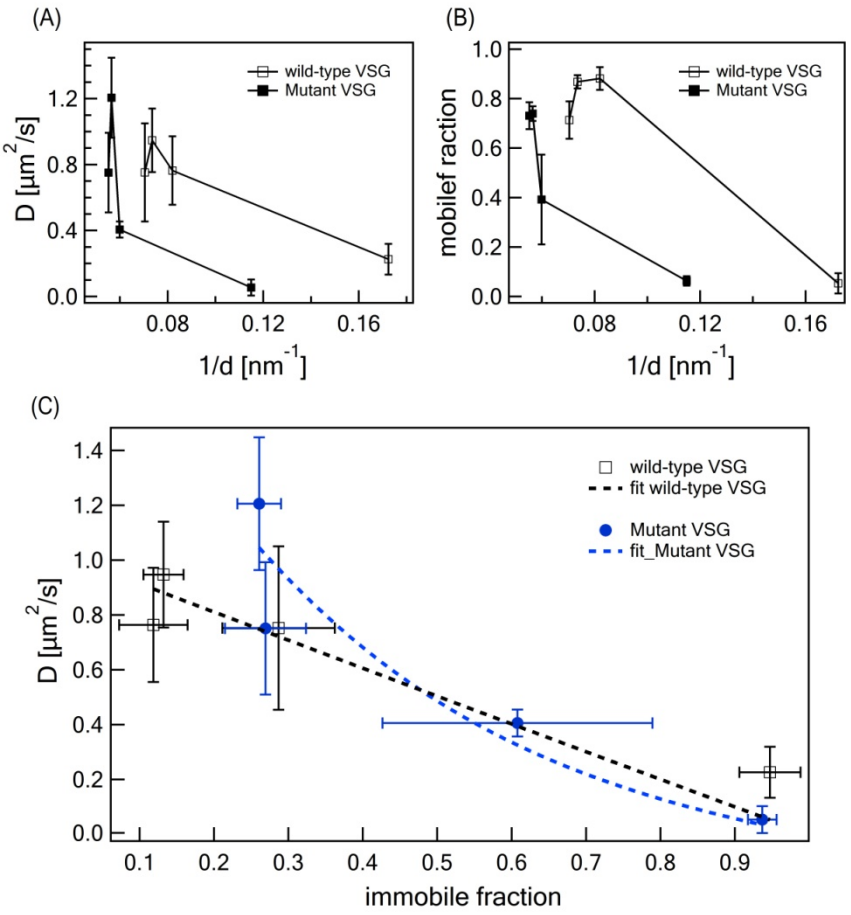

Fig. 5.5 *(A) The diffusion coefficients of wild type VSG (open squares) and mutant VSG (solid squares) are plotted against the reciprocal average separation between DOPE-biotin molecules. (B) The mobile fractions of wild type VSG (open squares) and mutant VSG (solid squares) are plotted against the reciprocal average separation between DOPE-biotin molecules. (C)The diffusion coefficients of wild type VSG (open squares) and mutant VSG (blue solid circles) are plotted against their immobile fractions. The blue and black dashed lines represent the fit according to equation 2.8. The error bars are standard deviations from the experimental errors.*

Fig. 5.5C shows the diffusion coefficients of wild type VSG (open squares) and mutant VSG (blue solid circles) given as a function of their immobile fractions. The blue and black dashed lines represent the fit according to equation 2.8. The best fit results imply distinctly different γ values; $\gamma \sim 0$ for wild type VSG and $\gamma \sim 2$ for mutant VSG (refer to section 2.1.3.2 for more details about γ). This finding suggests that removing N-glycosylation increases the obstacles to VSG diffusion which could be due to VSG aggregates or crystallization. Moreover, FRAP experiments on living trypanosomes showed that the diffusion coefficients and the mobile fraction remained constant until the

lateral protein density is reached at 1.5-fold concentration of VSG coat density indicating the VSG proteins can operate close to a molecular crowding threshold (see appendix A.3).

Table 5.4. The intermolecular separation *d*, diffusion coefficient *D*, mobile fraction and the calculated frictional coefficient b_s of VSG proteins incorporated into lipid membrane bilayer.

d [nm]	*D* [μm^2/s]	Mobile fraction [%]	b_s [N.s.m^{-3}]
Wild type VSG			
5.8	0.23 ± 0.09	5 ± 4	1.70×10^{10}
12.2	0.76 ± 0.21	88 ± 5	3.14×10^{9}
13.6	0.95 ± 0.19	87 ± 3	2.23×10^{9}
14.2	0.75 ± 0.30	71 ± 8	3.21×10^{9}
Mutant VSG			
8.7	0.05 ± 0.05	6 ± 3	9.35×10^{10}
16.7	0.41 ± 0.05	39 ± 18	7.87×10^{9}
17.7	1.21 ± 0.24	74 ± 3	1.49×10^{9}
18.1	0.75 ± 0.24	73 ± 6	3.22×10^{9}

5.3 Lateral diffusion of membrane-anchored proteins on sub-micron length scale

5.3.1 SPT revealed transition from free to confined diffusion for membrane-anchored proteins

The lateral diffusion coefficient of NA proteins at different lateral density were investigated with SPT technique. Fig. 5.6A shows typical diffusion traces of NA proteins at an intermolecular separation of $d \sim 18$ nm (trace 1, with trace length of 5 s) and at $d \sim 6$ nm (trace 2, with trace length of 16 s). Fig. 5.6B and 5.6C present the mean square displacement (black lines) together with a linear fit (red lines) of trace 1 and trace 2,

respectively. Due to the long-range fluctuations caused by low statistics in the MSD plot, the diffusion coefficient was determined from a linear fit to the first 5-10% of the trace length. The MSD plots clearly indicate that the lateral diffusion of NA proteins is normal at $d \sim 18$ nm and becomes confined at $d \sim 6$ nm.

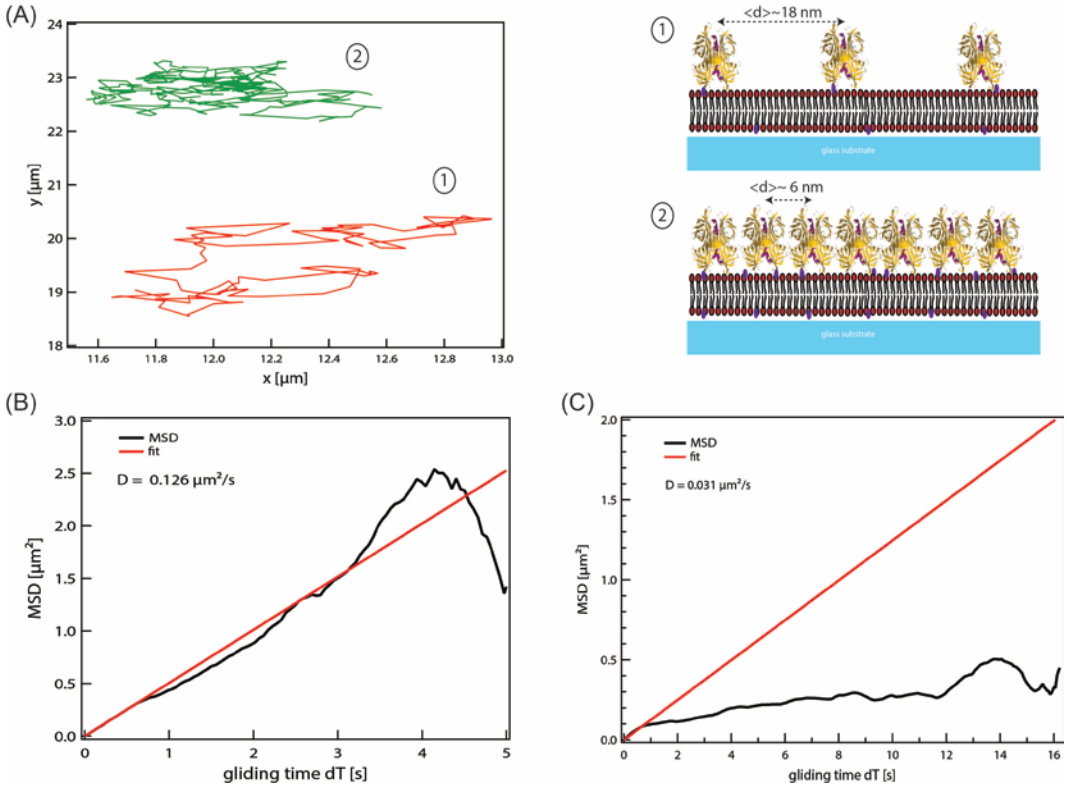

Fig. 5.6 *(A) Typical diffusion traces of NA proteins on membrane bilayer with intermolecular separation of d = 18 nm (trace 1, red line) and d = 6 nm (trace 2, green line) together with schematic illustration showing the corresponding situations where NA proteins are bound to the membrane bilayer. (B) The mean square displacement of trace 1 with a trace length of 5 s (black line). The diffusion coefficient was determined from slop of a linear fit to the first 10% of the of the MSD data points (red line). (C) The mean square displacement of trace 2 with a trace length of 16 s (black line). The red line represents a linear fit to the first 5% of the trace length.*

However, the determined distributions of diffusion coefficients of NA proteins at different lateral densities are represented in Fig. 5.7. The distribution is shifted toward small D values by increasing the lateral density of NA proteins. The mean values of the diffusion coefficients and the calculated frictional coefficients are summarized in table 5.5. The average diffusion coefficient of NA bound to membrane bilayer doped with 0.2 mol% DOPE-biotin lipids is found to be $D = 0.34 \pm 0.17$ µm^2/s which is in good

agreement with the corresponding value found from FRAP measurements (D = 0.422 ± 0.076 μm^2/s, table 5.3). In addition, the measured diffusion coefficients of NA at high lateral density (corresponding to χ = 1-3 mol%, table 5.3) were below or close to the detection limit of FRAP technique while in SPT measurements a clear discrimination between these cases could be observed. It should be noted that background measurements (before addition of NA) showed fluorescence signals of diffusive molecules that is similar to NA diffusion in diluted state which is most probably due to contamination of the sample chamber with NA proteins (see Appendix A.4)

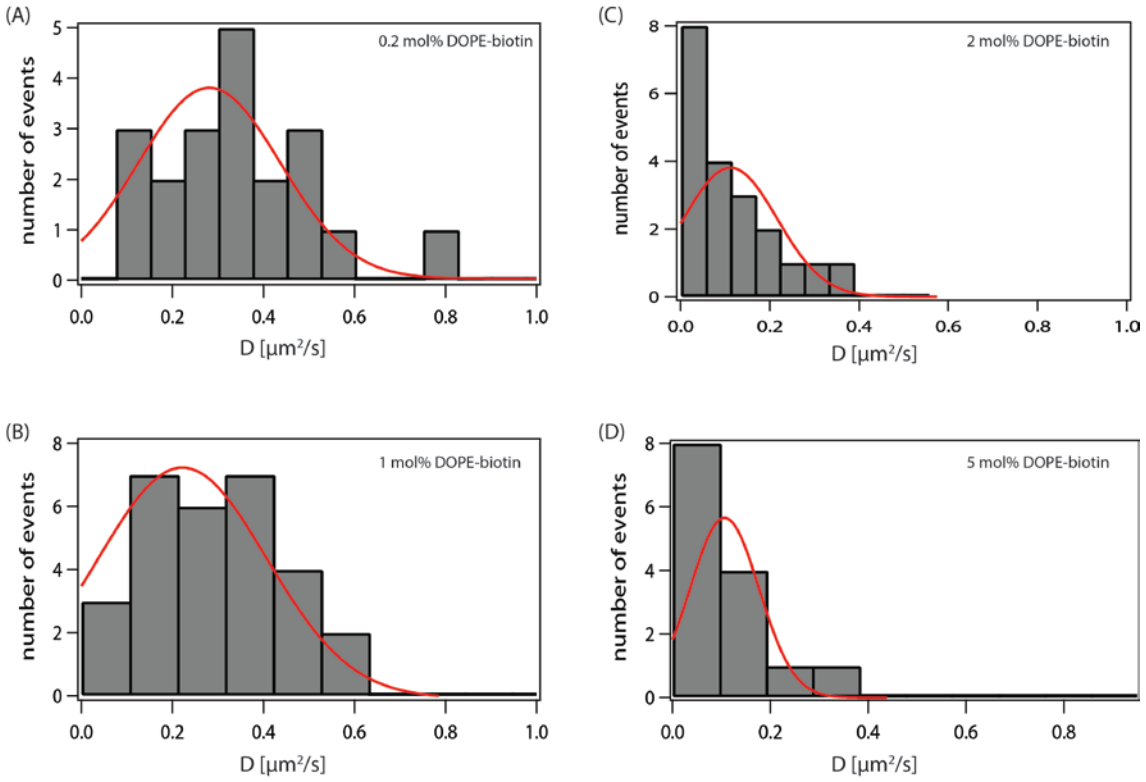

Fig. 5.7 *Distribution of diffusion coefficients of NA proteins bound to membrane bilayer doped with (A) 0.2 mol%, (B) 1 mol%, (C)2 mol% and (D) 5 mol% DOPE-biotin. The red line represents a fit to a Gaussian function in (A) and (B). In (C) and (D) are Gaussian functions plotted from the average value and standard deviation of data to point out the shift in the mean value.*

Table 5.5. Mean diffusion coefficient D and the frictional coefficient b_s of NA proteins bound to lipid bilayer doped with χ mole fraction of DOPE-biotin and the corresponding average separation d between DOPE-biotin molecules.

χ [mol%]	d [nm]	D [µm^2/s]	b_s [N.s.m^{-3}]
5	3.6	0.11 ± 0.07	4.09× 10^{10}
2	5.7	0.12 ± 0.13	3.69 × 10^{10}
1	8.1	0.28 ± 0.14	1.29 × 10^{10}
0.2	18	0.34 ± 0.17	9.9 × 10^{9}

Fig. 5.8 shows the mean diffusion coefficients (corresponding to Fig. 5.7) plotted against the reciprocal separation (blue solid triangles) that determined from the mole fraction of DOPE-biotin lipids within the membrane bilayer. The red line represents the fit according to equation 5.2. The obtained results from the fit yielded a percolation threshold at c_p ~ 0.139 ± 0.009nm^{-1} corresponding to an intermolecular separation of d = 7.2 nm. This value and the one found from mobile factions data (d = 6.9 nm, section 5.2.1) are consistent with the intermolecular distance found by GISAXS and GIXF (d = 6.8-8.9 nm, section 4.2)

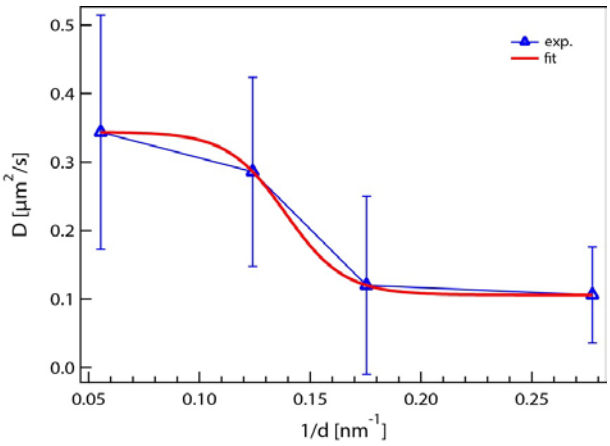

Fig. 5.8 *The mean diffusion coefficients corresponding to Fig. 5.7 are plotted against the reciprocal separation (blue solid triangles) that determined from the mole fraction of DOPE-biotin lipids within the membrane bilayer. The red line represents the fit according to equation 5.2.*

5.3.2 Non-VSG proteins hamper the VSG lateral diffusion on the surface of Trypanosoma brucei.

In living trypanosomes besides VSGs proteins that densely coat the parasite surface, there is about 5-10% from other proteins that populate the plasma membrane of trypanosomes. In order to investigate the influence of non-VSG proteins on the diffusivity of VSGs on the trypanosomes cell surface, VSG proteins were incorporated into solid-supported membrane bilayer doped with 5 mol% DOPE-biotin lipids followed by addition of NA proteins. The distributions of the diffusion coefficients of individual VSG proteins were determined by SPT technique before and after the addition of NA proteins.

Fig. 5.9A shows typical diffusion traces of VSGs incorporated into membrane bilayer before (trace 1, red line) and after the addition of NA proteins (trace 2, green line). The corresponding mean square displacement of trace 1 with a trace length of 14 s is shown in Fig. 5.9B (black line). The mean square displacement of trace 2 that has a trace length of 20 s is indicated in black line in Fig. 5.9C. From the shape of trace 1 and trace 2 and their corresponding MSD plots one can see that VSGs diffusion exhibit a transition from normal diffusion to confined diffusion upon the addition of NA proteins. However, Fig. 5.10A-C shows the distributions of diffusion coefficients of VSG proteins before (Fig. 5.10A) and after the addition of NA proteins where the membrane bilayer is doped with 0.5 mol% (Fig. 5.10B) or 5 mol% DOPE-biotin lipids ((Fig. 5.10C). The distributions show a clear shift toward lower diffusion coefficient values.

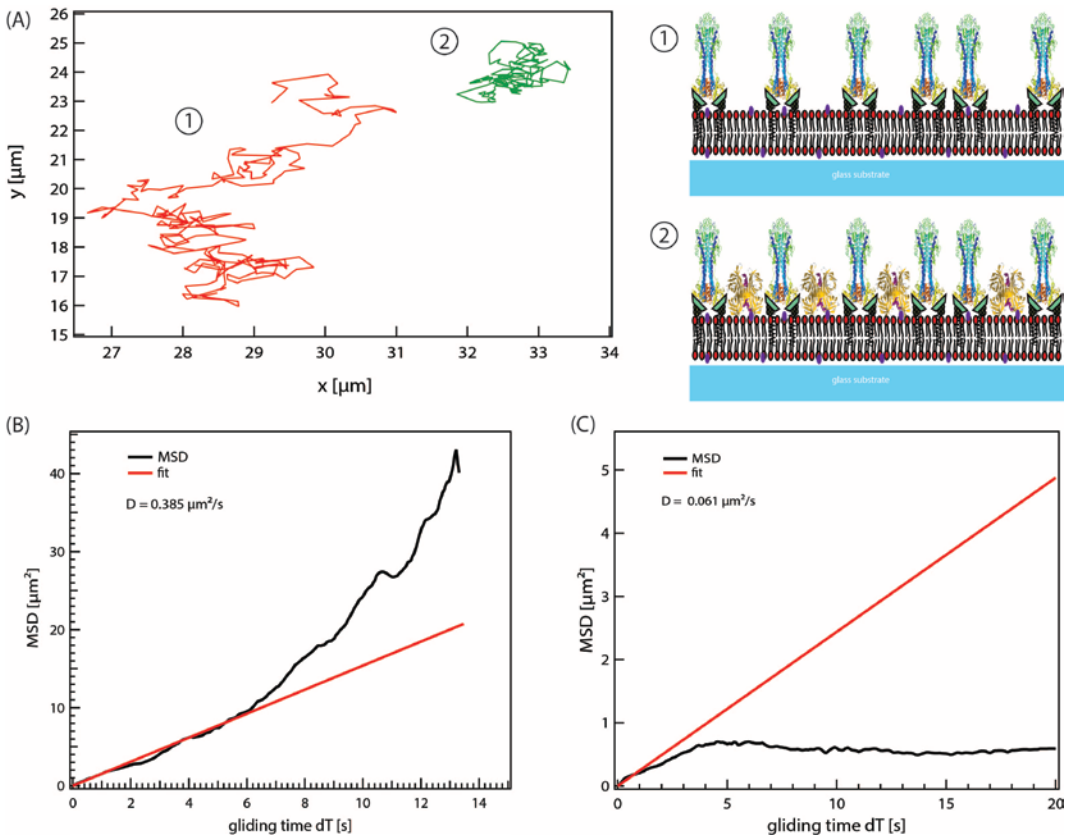

Fig. 5.9 *(A) Typical diffusion traces of VSG proteins incorporated into membrane bilayer before (trace 1, red line) and after the addition of NA proteins (trace 2, green line) together with schematic illustration showing the corresponding situations. (B) The mean square displacement of trace 1 with a trace length of 14 s (black line). The red line represents a linear fit to the first 5% of the trace length. (C) The mean square displacement of trace 2 with a trace length of 20 s (black line). The red line represents a linear fit to the first 5% of the trace length.*

The mean values of the distribution of the diffusion coefficients are summarized in Fig. 5.10C. The calculated frictional coefficient for VSG proteins before b_s = 6.22 × 10^9 N.s.m^{-3} and after b_s = 2.61 × 10^{10} N.s.m^{-3} the addition of NA proteins (bilayer doped with 5 mol% DOPE-biotin). This indicates that the reduction of the VSG diffusivity is due to the frictional stress exerted on VSGs from NA proteins. Moreover, FRAP results of VSGs after the addition of NA showed that NA proteins act as “obstacles” to VSG diffusion within the membrane bilayer (see Appendix A.5).

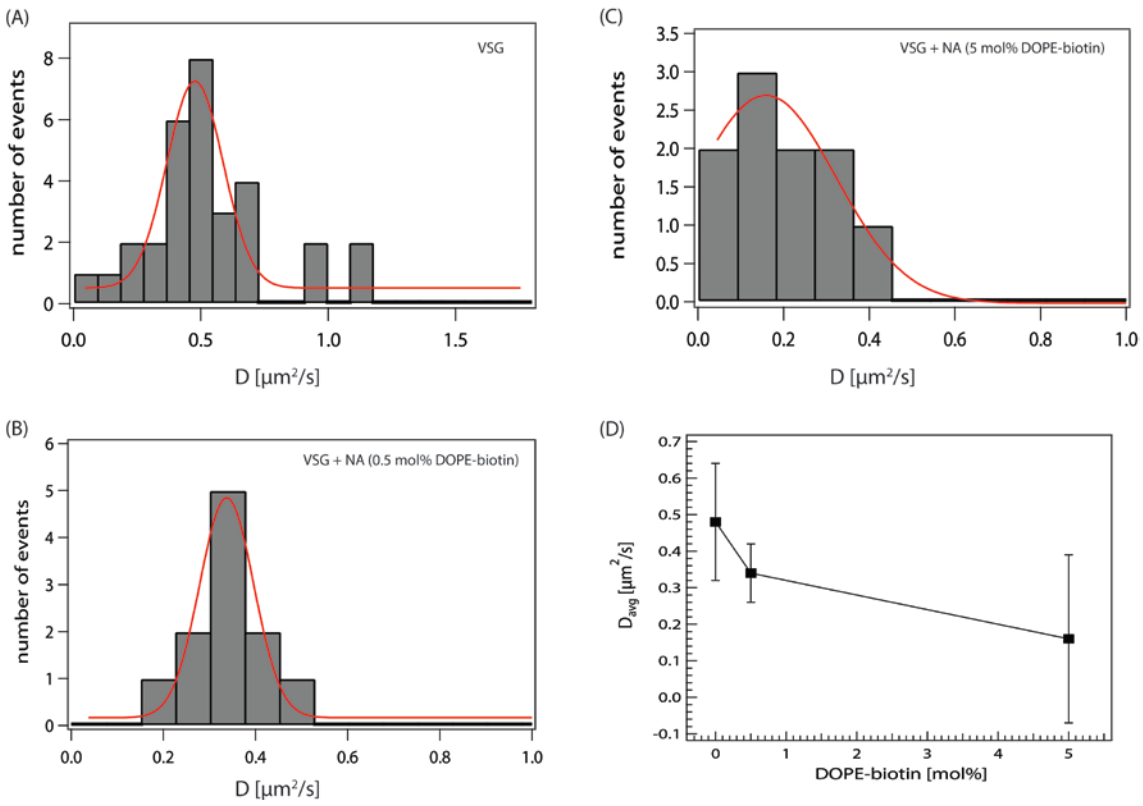

Fig. 5.10 *Distribution of diffusion coefficients of VSG proteins incorporated into membrane bilayer before (A) and after the addition of NA proteins where the bilayer doped with (B) 0.5 mol% and (D) 5 mol% DOPE-biotin. The red lines represent fit to a Gaussian function. (D) The average diffusion coefficients are plotted against the mole fraction of DOPE-biotin.*

6. Physical Interactions of Peptides with Bacterial Cell Membranes

As introduced in chapter 1, The outer surface of gram negative bacteria displays a dense layer of lipopolysaccharides (LPSs) [24] which protects the bacteria against the surrounding. LPSs are also known as endotoxins inducing a strong immune response upon binding to the receptor complex that promotes the secretion of pro-inflammatory cytokines [27]. A number of in vivo studies demonstrated that LPSs prevent the intrusion of cationic antimicrobial peptides (CAPs) into the cell membrane in the presence of divalent ions (Ca^{2+}, Mg^{2+}) [30-32], which inspire the design of peptide-based antibiotics [147]. Therefore, as defined model of outer membranes of gram negative bacteria, we investigated the interaction of monolayers of lipopolysacchrides from *Salmonella enterica* rough strains R90 (LPS Ra) with natural and synthetic peptides. In the first step, the pressure-area isotherms of LPS Ra monolayers were recorded on calcium free and calcium loaded buffers. Next, the fine structures of LPS Ra monolayers perpendicular to the membrane plane were determined by specular X-ray reflectivity (XRR). In addition, the ion distributions near the interface were determined by grazing incidence X-ray fluorescence (GIXF). In the last step, natural (fish protamine) and synthetic (anti-sepsis peptide, Pep 19-2.5) peptides were injected underneath LPS Ra monolayers followed by XRR and GIXF measurements to determinate the fine structures and ion distributions in the vicinity of the LPS Ra monolayer.

6.1 Influence of Ca^{2+} ions on bacterial membrane

6.1.1 Pressure-area isotherms of LPS Ra monolayers

Prior to X-ray experiments, the pressure-area (π-A) isotherms of LPS Ra monolayers were recorded (Fig. 6.1, left). The pressure-area isotherms of LPS Ra monolayers on Ca-free buffer and on Ca-loaded buffer are indicated in black and blue lines, respectively. The onset of the pressure increase in the presence of Ca^{2+} ions appears at an area per LPS Ra molecule of $A \sim 250$ Å^2 which is smaller than the corresponding value in the absence of Ca^{2+} ions ($A \sim 300$ Å^2). This suggests that the range of repulsive interactions between LPS Ra carbohydrate head groups is suppressed by Ca^{2+} ions. The LPS Ra monolayer collapses at a surface pressure of $\pi \sim 45$ mN/m and at $\pi > 55$ mN/m in the absence and

presence of Ca^{2+} ions, respectively. Fig. 6.1 (right) shows the calculated compressibility modulus κ^{-1} (equation 4.1) for LPS Ra monolayers on Ca-free (black line) and Ca-loaded buffers (blue line). The κ^{-1} curve in the presence of Ca^{2+} ions is below the one in the absence of Ca^{2+} ions (up to $\pi \sim 40$ mN/m). This demonstrates that the Ca^{2+} ions make the LPS Ra carbohydrate head groups less compressible and thus increases the intermolecular interactions between the molecules. The value of the compressibility modulus reaches $\kappa^{-1} \sim 100$ mN/m at surface pressure of $\pi \sim 30$ mN/m indicating the LPS Ra monolayer in both cases (on Ca-free or on Ca-loaded buffers) are in the liquid-expanded phase. Above a surface pressure of $\pi \sim 30$ mN/m, the value of κ^{-1} becomes > 100 mN/m suggesting a transition to liquid-condensed phase (see section 4.1). The drop of the compressibility modulus at high surface pressures to zero value indicates the collapse of the LPS Ra monolayer. However, these findings suggest that the interactions between LPS Ra molecules are significantly altered by Ca^{2+} ions.

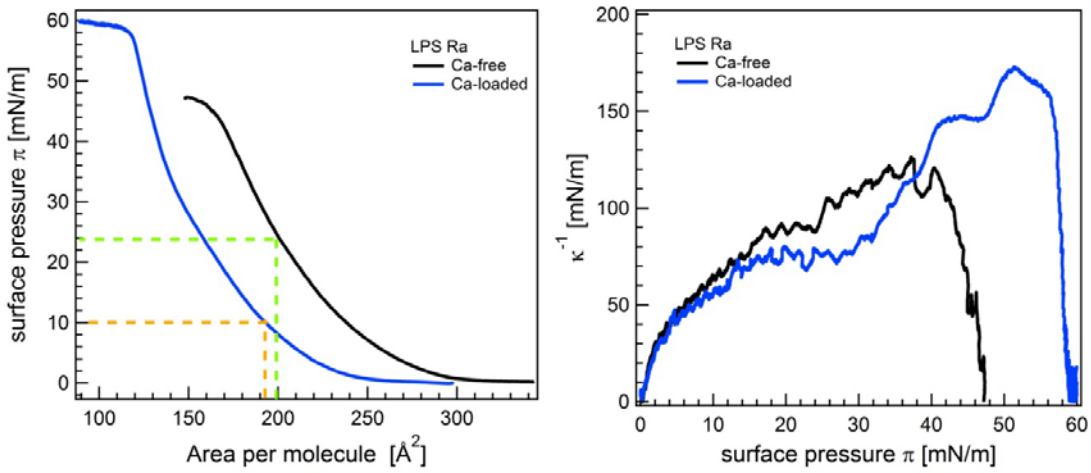

Fig. 6.1 *(Left) the pressure-area isotherms of LPS Ra on Ca^{2+}-free (red) and on Ca^{2+}-loaded (black) buffers. The green and orange dashed lines indicate the average are per molecules where XRR and GIXF measurements have been carried out. (Right) the corresponding compressibility modulus κ^{-1} is plotted versus surface pressure π.*

XRR and GIXF measurements were carried out at an area per LPS Ra molecule of $A \approx 200$ Å^2, which coincides with a surface pressure of π(free) = 24 mN/m and π(loaded) = 10

mN/m on Ca^{2+}-loaded (orange dashed line, Fig. 6.1, left) and Ca^{2+}-free (green dashed line, Fig. 6.1, left) subphases, respectively.

6.1.2 Influence of Ca^{2+} ions on the structure of LPS Ra membranes

LPS Ra molecules were spread into Langmuir film balance and compressed to an area per molecule of $A \approx 200$ Å^2. XRR were performed to investigate the structure of the LPS Ra monolayers perpendicular to the membrane surface on Ca^{2+}-free and on Ca^{2+}-loaded subphases. Fig. 6.2A shows the XRR curves of LPS Ra monolayers on Ca^{2+}-free (open circles) and Ca^{2+}-loaded (solid circles) together with the best fit results (red lines). For the fitting of the measured XRR curves, the LPS Ra monolayer is modeled with two slabs at the air-water interface: the first slab represents the hydrocarbon chains and the second for the carbohydrate head group. The layer parameters of LPS Ra previously measured by grazing incidence X-ray scattering out of specular plane (GIXOS) [148] were used as starting values for the fitting. It should be noted that the monolayer was prepared from the spreading of LPS Ra dissolved in organic solvents (see section 3.2), which enables one to precisely control the spreading amount. This is in contrast to the previous protocol that relied on the spreading of aqueous suspensions [148].

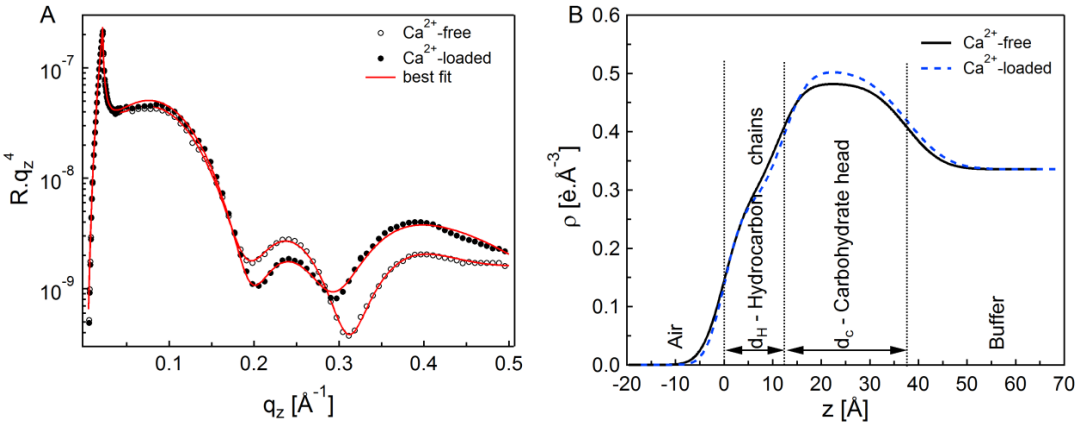

Fig. 6.2 *(A) XRR curves of LPS Ra monolayer on Ca-free buffer (open circles) and on Ca-loaded buffer (solid circles). The best fits matching the experimental results are indicated in red lines. (B) The reconstructed electron density profiles perpendicular to the interface for Ca-free (black) and Ca-loaded (broken blue line) buffers.*

Fig. 2B represents the reconstructed electron density profiles normal to the monolayer plane, and the layer parameters corresponding to the best fit results are summarized in

table 6.1. These profiles indicate that Ca^{2+} ions induce an increase in the electron density of the carbohydrate head group, accompanied with a slight decrease in the head group thickness. This finding seems consistent with the GIXOS results of Oliveira et al. [148], while the improved preparation step seems to result in a more smooth film by avoiding the re-adsorption of LPS Ra from the bulk subphase. The electron density of the Hydrocarbon chains is comparable to previously reported values of phospholipids $\rho \sim 0.3$ $e \times Å^{-3}$ [128-129, 149-151].

Table 6.1. Thickness *d*, electron density ρ, and roughness σ corresponding to best fits of the XRR data of LPS Ra monolayers in the presence and absence of Ca^{2+} ions corresponding to Fig. 6.2

LPS Ra on Ca^{2+}-free buffer (π= 24 mN/m)

	d (Å)	ρ ($e \times Å^{-3}$)	σ (Å)
Hydrocarbon chains	11.1 ± 0.3	0.288 ± 0.028	3.7 ± 0.4
Carbohydrate head groups	26.4 ± 0.7	0.483 ± 0.006	3.9 ± 0.5
Buffer	∞	0.334	5.8 ± 0.1

LPS Ra on Ca^{2+}-loaded buffer (π= 10 mN/m)

	d (Å)	ρ ($e \times Å^{-3}$)	σ (Å)
Hydrocarbon chains	12.2 ± 0.7	0.275 ± 0.029	3.1 ± 0.4
Carbohydrate head groups	25.4 ± 1.3	0.504 ± 0.007	3.9 ± 0.5
Buffer	∞	0.334	6.7 ± 0.9

6.1.2 Influence of Ca^{2+} ions on the electrostatics of LPS Ra membranes

Every XRR measurement on LPS Ra monolayers was followed by performing GIXF measurement to determine the concentration profiles of the ions in the vicinity of saccharide monolayers. Fig. 3 represents the fluorescence spectra from LPS Ra monolayers on Ca^{2+}-free (top) and Ca^{2+}-loaded (bottom) buffers measured at angles of

incidence below (α_i = 0.1°, solid squares) and above (α_i = 0.2°, open circles) the critical angle of incidence, α_c = 0.154°. These spectra were fitted with multiple Gaussian peaks fitting routine to extract contribution of each fluorescence characteristic line (Fig. 3, red lines). K K_α and K K_β lines appear at peak positions of 3.31 keV and 3.59 keV, respectively. Ca K_α line has an overlap with K K_β line at 3.69 keV, while Ca K_β line has a peak at 4.01 keV. The penetration depth of the evanescent field calculated for α_i = 0.1° and 0.2° can be calculated from Eq. 2, Λ(0.1°) = 60 Å and Λ(0.2°) = 1309 Å. In the absence of Ca^{2+} ions (top panel), K K_α intensity is enhanced at the interface (solid squares) compared to the signal intensity from the bulk (open circles). On the other hand, Cl^- ions do not show any sign of accumulation to the interface [152]. In the presence of Ca^{2+} ions (bottom panel), Ca K_α signal is more pronounced at α_i = 0.1°. This finding suggests the condensation of Ca^{2+} ions at the interface, which is in contrast to K K_α signal exhibiting no sign of condensation.

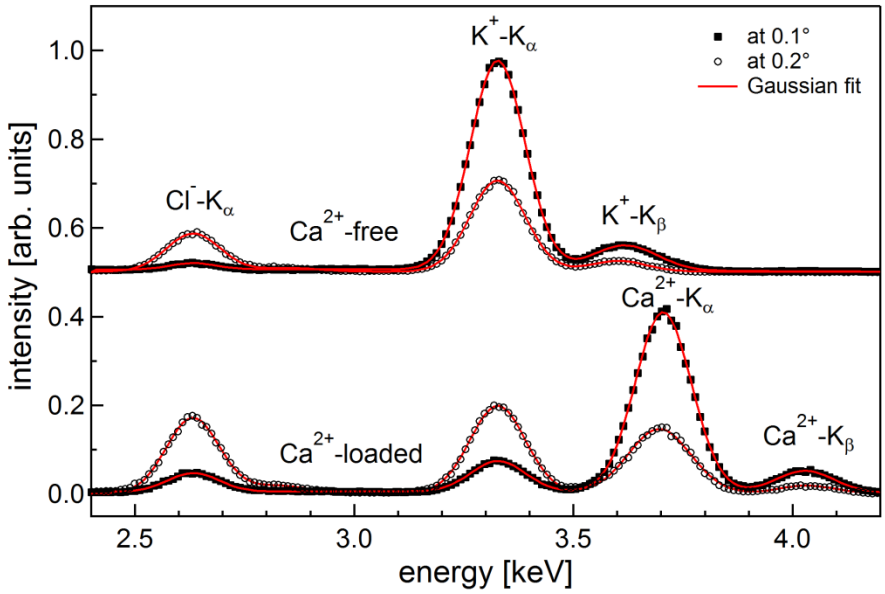

Fig. 6.3 *Fluorescence spectra from LPS Ra monolayers on Ca-free (top) and Ca-loaded (bottom) buffers recorded at angles of incidence below (solid squares) and above (open circles) the critical angle of incidence (α_i = 0.154°). Red lines indicate the multiple-Gaussian peaks fitting. The spectra of LPS Ra on Ca^{2+}-free are shifted vertically for clarity.*

Fig. 6.4 represents the normalized fluorescence signal of each line plotted as a function of q_z. On Ca^{2+}-free buffer (Fig 4A), the K K_α signal below the critical edge (q_c = 0.022 $Å^{-1}$)

was much more enhanced in the presence of a LPS Ra monolayer (solid squares) than that on the blank buffer (open squares). This finding implies the enrichment of K^+ ions near the air-water interface through interaction with the LPS Ra surface. On Ca^{2+}-loaded buffer (Fig. 4B), the K K_α signal in the presence of LPS Ra monolayer (solid squares) is comparable to the signal on the blank buffer. In contrast, the Ca K_α signal (open circles) exhibited a prominent peak at $q < q_c$, indicating the condensation of Ca^{2+} ions near the interface. The depletion of K^+ ions and condensation of Ca^{2+} observed on Ca^{2+}-loaded buffer suggest that K^+ ions near the interface are replaced by Ca^{2+} ions. It should be noted that the measured fluorescence signals are given as a function of illumination intensity, concentration profile normal to the interface, the quantum yield of each element, and the re-absorption from the bulk medium (water). The latter two effects can be canceled out by normalizing the fluorescence signals to the corresponding signals from blank buffer. This step also excludes the artifacts from geometrical effects. The normalization procedure can be summarized by the following equation:

$$I(q_z)_{relative} = \left(\frac{I(q_z)_{Fluo.line}}{I(q_z)_{elestic\ peak}} \right)_{monolayer} \div \left(\frac{I(q_z)_{Fluo.line}}{I(q_z)_{elestic\ peak}} \right)_{blank\ buffer} \tag{6.1}$$

In addition, the K_α lines were used to reconstruct the concentration profiles since they are more intense than the K_β lines (Fig. 6.3) and thus less erroneous.

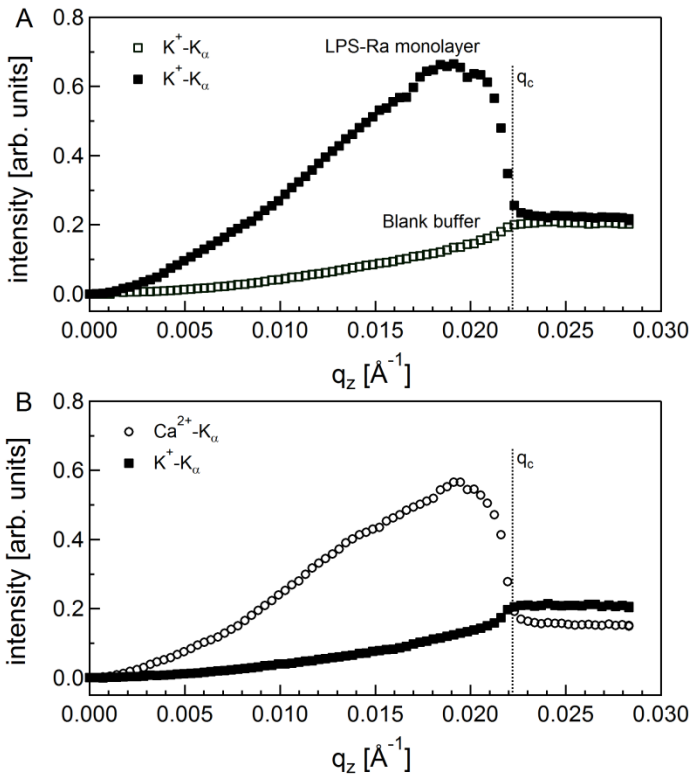

Fig. 6.4 *(A) K K_α fluorescence signals in the presence (solid squares) and absence (open squares) of LPS Ra monolayer on Ca-free buffer. (B) Comparison of Ca K_α signal (open circles) and K K_α signal (solid squares) in the presence of LPS Ra monolayer on Ca-loaded buffer. The q_z value corresponding to the critical angle (q_c) is indicated by dotted lines.*

The black solid squares in Fig 6.5A represent the relative K K_α signals from LPS Ra monolayer on Ca-free buffer (solid squares) given as a function of q_z. The blue open and solid squares in the panel A are K K_α and Ca K_α from LPS Ra monolayer on Ca^{2+}-loaded buffer, respectively. The experimental data was fitted by equation 2.45 (see section 2.5). Here, the illumination intensity was calculated using the values obtained from the XRR analysis (table 6.1). The concentration profile of the ion species condensed near the interface was modeled using equation 2.51, taking bulk concentrations of c_0 = 0.1 M and c_0 = 0.05 M for K^+ and Ca^{2+} ions, respectively. On the other hand, we assumed constant ion concentration profiles for blank buffers, since the ion depletion/condensation near the interface is negligibly small in the absence of surfactant films [139]. The value of z_{HC} in equation 2.51 is provided from the thickness of hydrocarbon chains obtained by XRR; *d* = 11.1 and 12.2 Å in the absence and presence of Ca^{2+} ions, respectively. The ion

concentration profiles corresponding to the best fit results in Fig. 6.5A are presented in Fig. 6.5B. The distribution of K^+ ions on Ca^{2+}-free buffer (black solid line) has a clear peak at z_{max} = 15 Å, c_{max} = 8.6 ± 0.5 M. The peak position (z_{max} = 15 Å) corresponds to the inner core saccharides of a LPS Ra molecule, possessing four negatively charged saccharide units (two phosphorylated glucosamine units and two KDO units). Integrating the excess ion concentration along the z-axis yields the lateral density of K^+ ions, c_L = (2.9 ± 0.25) × 10^{14} ions/cm^2. Taking the area occupied by one LPS Ra molecule on Ca^{2+}-free buffer (A = 200 $Å^2$, π-A isotherm in section 5.1.1), one can quantitatively determine the number of K^+ ions bound to one LPS Ra molecule, N = 5.9 ± 0.6. This value can be understood from the conservation of charge neutrality, since one LPS Ra can carry negative charges up to Q_{LPSRa} ~ - 6 e.

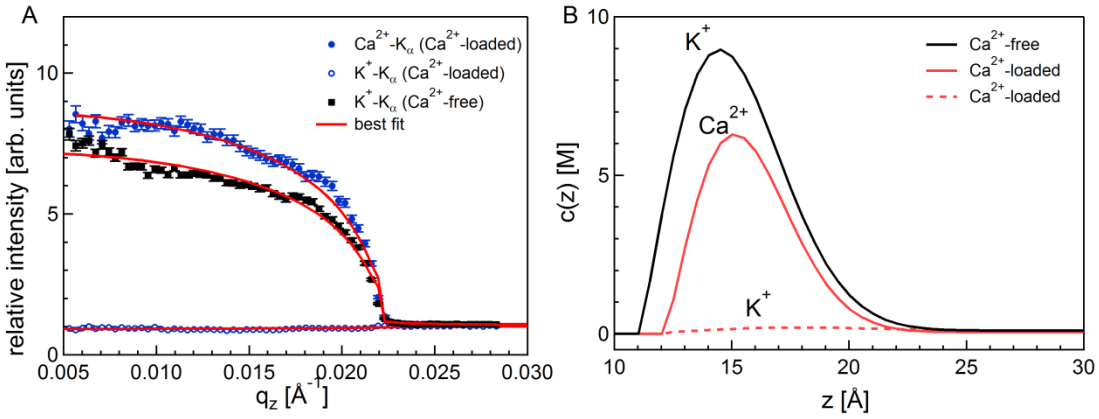

Fig. 6.5 *(A) Relative fluorescence intensities from LPS Ra monolayers of K K_α (black solid squares) on Ca-free buffer, K K_α (blue open circles) and Ca K_α (blue solid circles) on Ca-loaded buffer. The red lines indicate the best fit from equation 2.45 to the experimental data. Vertical bars are ± standard deviation obtained from Gaussian error propagation during the fit of the fluorescence spectra. (B) The corresponding ion concentration profiles perpendicular to the interface that obtained from the fits for K^+ ions (black line) on Ca-free buffer, K^+ ions (broken line) and Ca^{2+} ions (red line) on Ca-loaded buffer.*

The red lines in Fig. 6.5B represent the concentration profiles of Ca^{2+} (solid) and K^+ (broken) ions on Ca^{2+}-loaded buffer. First, it should be noted that the concentration of K^+ ions near the interface is almost identical to the bulk concentration, while Ca^{2+} ions exhibit a distinct maximum at z_{max} = 16 Å, corresponding to the concentration of c_{max} = 6.2 ± 0.3 M. Integrating the excess concentration along the z-axis yields the lateral

density of Ca^{2+} ions $c_L = (1.8 \pm 0.1) \times 10^{14}$ ions/cm^2. If one takes the area per molecule on Ca^{2+}-loaded buffer (A = 192 Å^2, π-A isotherm in section 5.1.1), the number of Ca^{2+} ions associated with one LPS Ra molecule can be determined to be N = 3.5 ± 0.3 Ca^{2+} ions are associated with one LPS Ra molecule. Note that the chloride ions are neglected in the calculation of the total effective charge of LPS Ra molecules (see appendix A.6).

It should also be noted that the relative K^+ fluorescence intensity in Ca-loaded buffer (Fig. 6.5A, blue open circles) at $q_z < q_c$ is slightly less than unity. Though this may be attributed to the depletion of K^+ ions near the interface, the corresponding concentration profile (Fig. 6.5B, red broken line) obtained from the fit indicates that the K^+ ion concentration at the head group region is slightly higher than the bulk concentration. In fact, the estimated number of K^+ ions associated with LPS Ra molecule is N = 0.3 ± 0.2. We concluded that the slightly lower intensity at $q < q_c$ reflects the modification of the electron density at the air-water interface in the presence of LPS Ra monolayer. The observed replacement of monovalent cations by divalent cations from the negatively charged inner core saccharides is consistent with our previous study of LPS Re possessing only inner core saccharide units [18]. Compared to the simulation we used previously, the fitting of c_{max} and z_{max} developed in this study allows for the localization of ions with a higher precision (z_{max} ± 3 Å, see section 2.5), unraveling the condensation of ions in the charged inner core saccharides of a more complex LPS Ra molecule. Our experimental results are in a good agreement with the number density of K^+ and Ca^{2+} ions calculated from the coarse-grained Monte Carlo simulations on LPS Ra [148] as well as the molecular dynamic simulations [37, 153-154]. The results are summarized in table 6.2.

Table 6.2. Summary of the results obtained from GIXF. Number of ions associated with LPS Ra molecule N, position of the concentration profile maxima z_{max}, its maximum value c_{max} and excess lateral concentration of ions $c_{L.}$

LPS Ra on:	Ca-free	Ca-loaded
N (K) [ions/LPS Ra]	5.9 ± 0.6	0.3 ± 0.2
z_{max}(K) [Å]	15 ± 3	18 ± 3
c_{max}(K) [M]	8.6 ± 0.5	0.15 ± 0.07
c_L(K) [$\times 10^{14}$ ions/cm^2]	2.9 ± 0.5	0.16 ± 0.11
N (Ca) [ions/LPS Ra]	--	3.5 ± 0.3
z_{max}(Ca) [Å]	--	16 ± 3
c_{max}(Ca) [M]	--	6.2 ± 0.3
c_L(Ca) [$\times 10^{14}$ ions/cm^2]	--	1.8 ± 0.1

Moreover, the presented ions distributions exhibit peaks at around z_{max} ~ 15 Å which decays gradually and reaches the bulk concentration near z ~ 22 Å. Since the total thickness of the LPS Ra monolayer in the absence or presence of Ca^{2+} is around d = 37.5 Å, the fast decay in ion density profiles suggests that the majority of ions are accumulated near the KDO and phosphorylated saccharide units but not around the uncharged saccharide units in the outer core.

6.2 Interactions of peptide drugs with bacterial membrane

6.2.1 Interaction of anti-sepsis peptide with LPS Ra monolayer

The interactions of anti-sepsis peptide Pep 19-2.5 with LPS Ra monolayers in the absence and presence of Ca^{2+} were studied by injecting Pep 19-2.5 into the subphase underneath LPS Ra monolayers to reach the final bulk concentration of 7 µg/ml (see section 3.2.2.3). On Ca-free buffer, the surface pressure (π = 24 mN/m) increased up to $\pi \approx$ 50 mN/m. On the other hand, although the initial surface pressure was much lower (π = 10 mN/m), the LPS monolayer on Ca-loaded buffer showed an increase of the surface pressure to π = 27 mN/m.

Fig. 6.6A shows the XRR curves of LPS Ra after the injection of Pep 19-2.5 in the absence (open circles) and the presence (solid circles) of Ca^{2+}. The best fits matching to the results are shown in red lines. To evaluate the change in the monolayer structure caused by Pep 19-2.5, the parameters of the LPS Ra monolayers obtained from the fits prior to the peptide injection (table 6.1) were used as the starting values for fitting. The parameters corresponding to the fits results are summarized in table 6.3.

In the absence of Ca^{2+}, the injection of Pep 19-2.5 led to an increase in the electron density of the head groups from $\rho = 0.483$ e × $Å^{-3}$ to 0.506 e × $Å^{-3}$, accompanied with a small increase in the total monolayer thickness ($\Delta d = 0.7$ Å). Moreover, we also observed an increase in the roughness of each layer. The observed increase in the electron density, thickness, and roughness seems consistent with a significant increase in the surface pressure to $\pi = 50$ mN/m. These results suggest that Pep 19-2.5 molecules do not only adsorb on the monolayer surface but also further go deeper into the head group region of the LPS Ra monolayer in the absence of Ca^{2+} ions. It is noteworthy that the electron density profile of the LPS Ra monolayer can still be represented by stratified "slabs" even in the absence of Ca^{2+}. This is in contrast to our previous studies on herring protamine, where we observed the destruction of the layered structures caused by the protamine injection [18].

On the other hand, in the presence of Ca^{2+}, the increase in surface pressure was not accompanied with the destruction of monolayer structures. The thickness and the electron density of both the hydrocarbon chains and the carbohydrate head groups remained almost identical before and after the injection of Pep 19-2.5, but, similar to the case of Ca^{2+}-free buffer, we observed an increase in the roughness of each layer [19]. The increase in the surface pressure and the interfacial roughness implies that Pep 19-2.5 molecules weakly interact with the LPS Ra monolayer without destroying the stratified layer structures. In fact, there was no improvement in the quality of the reflectivity analysis by using additional slab assuming another Pep 19-2.5 layer.

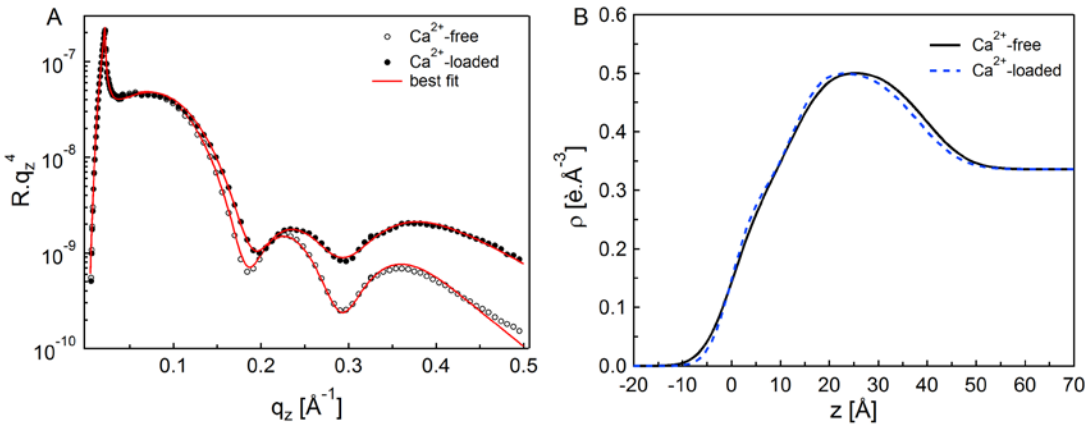

Fig. 6.6 *(A) XRR results from LPS Ra monolayer on Ca-free buffer (open circles) and Ca-loaded buffer (solid circles) after the injection of Pep 19-2.5 underneath LPS Ra monolayers. The best fits to the experimental results are presented as red lines. (B) The electron density profiles reconstructed from the best fits.*

Table 6.3. Thickness *d*, electron density ρ, and roughness σ corresponding to the best fits of the XRR of LPS Ra after the injection of Pep 19-2.5 solution into the subphase. The values correspond to Fig. 6.6. The errors are standard deviations from the fitting error propagation.

LPS Ra + Pep 19-2.5 on Ca-free buffer (π= 50 mN/m)

	d (Å)	ρ (e × Å^{-3})	σ (Å)
Hydrocarbon chain	12.5 ± 0.7	0.280 ± 0.008	4.8 ± 0.6
Carbohydrate head	27.1 ± 1.2	0.506 ± 0.008	5.6 ± 0.4
Buffer	∞	0.334	6.9 ± 0.1

LPS Ra + Pep 19-2.5 on Ca-loaded buffer (π= 27 mN/m)

	d (Å)	ρ (e × Å^{-3})	σ (Å)
Hydrocarbon chain	12.5 ± 0.6	0.293 ± 0.015	3.8 ± 0.4
Carbohydrate head	25.5 ± 1.4	0.504 ± 0.007	4.4 ± 0.6
Buffer	∞	0.334	7 ± 0.6

The black solid squares in Fig. 6.7A represent the relative fluorescence intensities of K K_α from LPS Ra monolayer on Ca-free buffer after Pep 19-2.5 injection. The K K_α and Ca K_α signals from the same monolayer on Ca-loaded buffer are indicated by blue, open

and solid circles, respectively. The best fit results of the GIXF signals are shown as red lines in Fig. 6.7A.

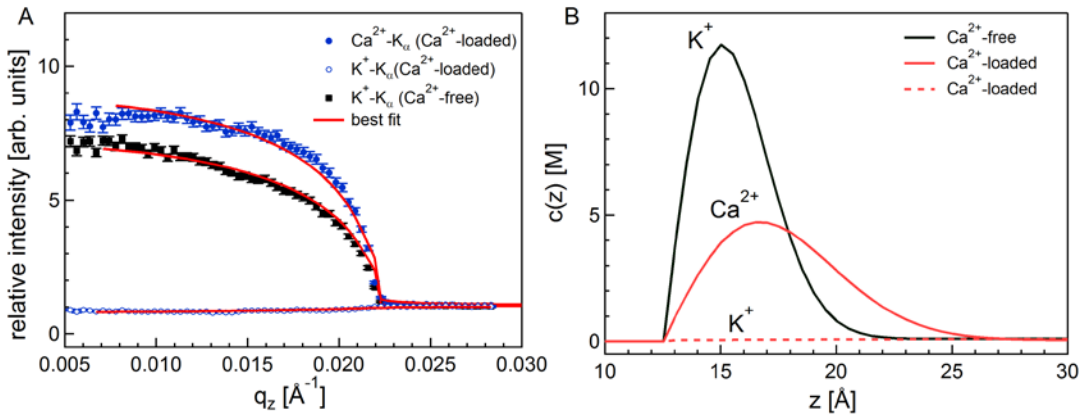

Fig. 6.7 *(A) Relative fluorescence intensities from LPS Ra monolayers with Pep 19-2.5 of K K_α (black solid squares) on Ca-free buffer, K K_α (blue open circles) and Ca K_α (blue solid circles) on Ca^{2+}-loaded buffer. The red lines indicate the best fit from equation 2.45 to the experimental data. Vertical bars are ± standard deviation obtained from Gaussian fitting of the fluorescence spectra. (B) The corresponding ion concentration profile normal to the interface obtained from the fits for K^+ ions (black line) on Ca-free buffer, K^+ ions (broken line) and Ca^{2+} ions (red line) on Ca-loaded buffer.*

The concentration profile of K^+ on Ca^{2+}-free buffer reconstructed from the best fit result (red line, Fig. 6.7A) is presented as black line in Fig. 6.7B. It should be noted that the peak position of K^+ distribution (z_{max} = 15 Å) was found at the same position as the one in the absence of Pep 19-2.5 (Fig. 6.8A). In addition, the K^+ concentration decays to the bulk level at z = 22 Å and z = 23 Å in the absence and presence of Pep 19-2.5, respectively. These changes are below the z-resolution (±3 Å) of GIXF. In fact, the number of K^+ ions associated with one LPS Ra molecule (N = 5.8 ± 0.6) is almost equal to that in the absence of Pep 19-2.5 (N = 5.9 ± 0.6). These results thus demonstrated that the distribution of K^+ ions in the negatively charged inner core saccharide region remains intact even in the presence of Pep 19-2.5 molecules. This observation suggests that the Pep 19-2.5 molecules adsorb to into the peripheral part of the LPS Ra monolayer, but do not reach the charged inner core region (Fig. 6.8A). This interpretation is further supported by the intactness of the electron density and the thickness of the hydrocarbon chain region (table 6.1 and table 6.3).

The red lines in Fig. 6.7B represent the density profiles of Ca^{2+} (solid) and K^+ (broken) ions on Ca^{2+}-loaded buffer after Pep 19-2.5 injection. Similar to the results obtained in the absence of Pep 19-2.5 (Fig. 6.5B), we observed the replacement of K^+ ions by Ca^{2+} ions. However, in contrast to the K^+ distribution on Ca-free buffer, the density profile of Ca^{2+} ions takes a peak at z_{max} = 17 Å which is shifted from the position before injecting Pep 19-2.5 (z_{max} = 15 Å). Moreover, a clear broadening of the Ca^{2+} distribution could be observed. Here, the Ca^{2+} concentration reaches the bulk level at z = 26 Å. On the other hand, the numbers of Ca^{2+} and K^+ ions associated with one LPS Ra molecule are almost identical to those in the absence of Pep 19-2.5, N_K = 0.5 ± 0.1 and N_{Ca} = 3.7 ± 0.3, respectively. However, the broadening of the Ca^{2+} distribution as well as the increase in the surface pressure to 27 mN/m do not cause any remarkable change in the thickness, electron density, and roughness of the head group region, suggesting that the adsorption of Pep 19-2.5 on Ca-loaded buffer is much weaker than that on Ca-free buffer (Fig. 6.8B).

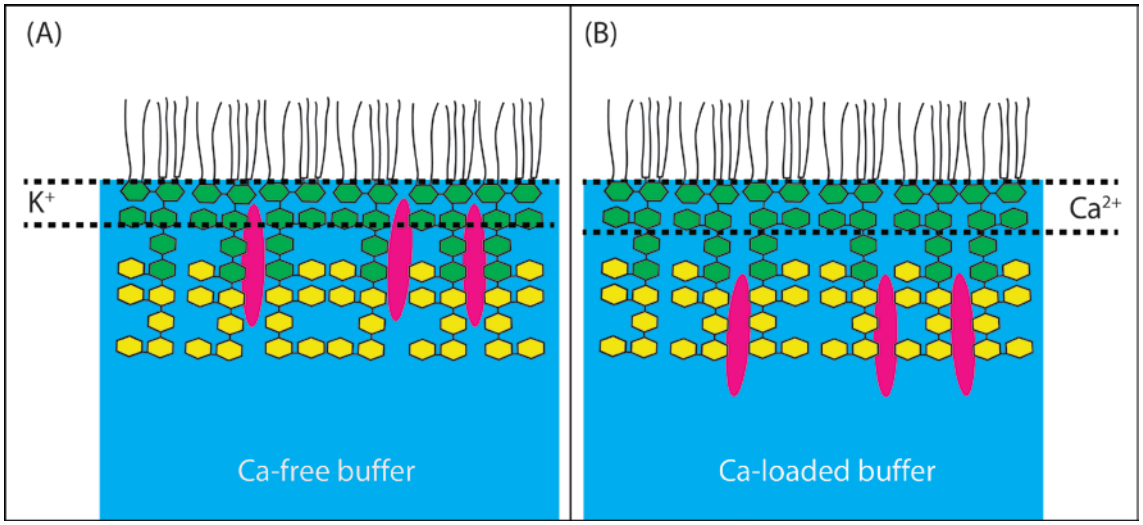

Fig. 6.8 *Illustration showing the suggested interaction mechanisms of LPS Ra monolayers with Pep 19-2.5 molecules indicated in red ellipses on Ca-free buffer (A) and on Ca-loaded buffer (B). The neutral and negatively charged sugar units are represented by yellow and green colors, respectively. The area between dashed lines indicates the position of the maximum concentration of the ions.*

The fact that the injection of Pep 19-2.5 causes almost no change in the K^+ distribution on Ca-free buffer (black lines in Fig. 6.5B and Fig. 6.7B) suggests that the slight increase in the electron density ($\Delta\rho_m$ = 0.023 e × $Å^{-3}$) and the thickness (Δd_C = 0.7 Å) of the head

group region is caused by the penetration of Pep 19-2.5 molecules into the saccharide head group up to z > 22 Å. Here, the volume fraction of Pep 19-2.5 within the head group layer ϕ_{P19} can be obtained by:

$$\phi_{P19} = \frac{\Delta\rho_m}{\rho_{dry} - \rho_{buffer}} \qquad (6.2)^2$$

where ρ_{dry} and ρ_{buffer} are the electron densities of Pep 19-2.5 in dry state and the blank buffer, respectively. From the known amino acid sequence of Pep 19-2.5 [102] (see section 3.1.3), one can estimate the molecular volume of Pep 19-2.5 to be V_{P19} = 3346 ± 24 Å^3 [134-135] and its electron density in dry state to be ρ_{dry} = 0.433 ± 0.003 e × Å^{-3}, yielding ϕ_{P19} = 23 %. Taking the area per molecule on Ca^{2+}-free buffer (A = 200 Å^2) and the thickness of the head group region (d_C = 27.1 Å), the number of Pep 19-2.5 molecules interacting with one LPS Ra molecule can be calculated to be N = 0.37. This value seems to be in an excellent agreement with the number of Pep 19-2.5 per one LPS Ra molecule, estimated from the isothermal titration calorimetry experiments N = 0.3 [29, 102, 155].

6.2.2 Interaction of fish protamine with LPS Ra monolayer

Protamine is a naturally occurring cationic antibacterial peptide (CAP) used in food industry as food preservative. To determine the influence of protamine on the electrostatics and the structure of LPS Ra monolayer, herring protamine was injected into the subphase to a final concentration of 1 mg/ml, which is comparable with the minimum inhibitory concentration determined by in vivo experiments (1.25 mg/ml) [156] (see section 3.2). On Ca-free buffer, the injection of protamine led to an abrupt increase in the surface pressure of LPS Ra monolayers up to π = 50 mN/m, which is closed to the value we reported previously (45 mN/m) [148]. On the other hand, LPS Ra monolayer on Ca-loaded buffer remained almost intact, showing a very small increase in the surface pressure (Δπ < 5 mN/m).

Fig. 6.9A shows the XRR data of LPS Ra monolayers after protamine injection on Ca^{2+}-free (open circles) and Ca^{2+}-loaded (solid circles) buffers with the best matching fits (red

[2] See appendix A.7 for verification of this equation

lines). The parameters obtained from the best fitting results are summarized in table 6.4. The electron density profiles reconstructed from the fits are presented in Fig. 6.9B, where black line stands for calcium free subphase and blue broken line for calcium loaded subphase.

In the absence of Ca^{2+} ions, a drastic decrease in the hydrocarbon chains layer thickness down to d_H = 7.1 Å and a clear increase in the head group layer thickness (d_C = 31.1 Å) was observed. Moreover, the roughness of all interfaces showed a clear increase compared to the corresponding values presented in table 6.1. In addition, the modifications of the electron density profile (Fig. 6.2B and Fig. 6.9B) and a significant increase in the surface pressure ($\Delta\pi$ ~ 30 mN/m) suggests that the protamine molecules disrupt the overall structure of LPS Ra monolayer. This makes it difficult to distinguish chains and headgroups as independent slabs. In contrast, in the presence of Ca^{2+} ions, the structure of LPS Ra monolayer is almost retained even after the protamine injection. The slight differences in the electron density of head groups can be attributed to the deviation in the lateral compression caused by different preparations.

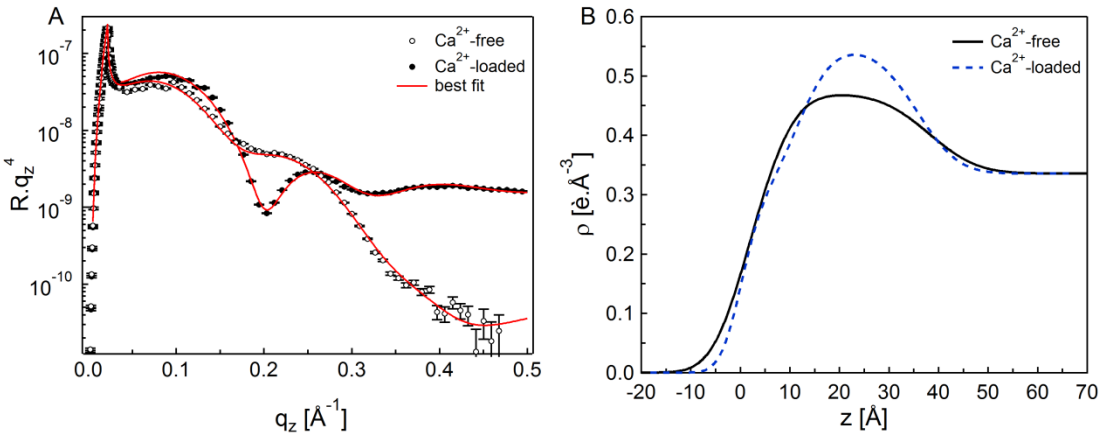

Fig. 6.9 *(A) XRR curves of LPS Ra monolayer on Ca-free buffer (open circles) and Ca-loaded buffer (solid circles) after the injection of protamine molecules underneath LPS Ra monolayer. The best fits matching the experimental results are shown in red lines. (B) The reconstructed electron density profile perpendicular to the membrane surface.*

Table 6.4. Thickness *d*, electron density ρ, and roughness σ corresponding to best fits of the XRR of LPS Ra after protamine injection into the subphase corresponding to Fig. 6.8.

LPS Ra + Protamine on Ca-free buffer (π= 50 mN/m)

	d (Å)	ρ (e × Å^{-3})	σ (Å)
Hydrocarbon chains	7.1 ± 2.3	0.299 ± 0.015	5.3 ± 0.9
Carbohydrate head group	31.1 ± 5.1	0.470 ± 0.073	5.3 ± 3.7
Buffer	∞	0.334	7.7 ± 4.1

LPS Ra + Protamine on Ca-loaded buffer (π= 24 mN/m)

	d (Å)	ρ (e × Å^{-3})	σ (Å)
Hydrocarbon chains	11.3 ± 0.1	0.276 ± 0.007	3.3 ± 0.1
Carbohydrate head group	24.4 ± 0.2	0.546 ± 0.009	5.6 ± 0.3
Buffer	∞	0.334	6.6 ± 0.2

In Fig. 6.10A, the relative K K_α fluorescence intensities of LPS Ra monolayers in the presence of protamine on Ca-free buffer are presented by solid black squares, and the signals from K K_α and Ca K_α on Ca-loaded buffer are in blue open and solid circles. The best fit results are labeled with red lines in the same panel. It is remarkable that the concentration profile of K^+ ions (black line, Fig. 6.10B) has a constant value equal to the bulk concentration (c_0 = 0.1 M) up to the air-water interface, which is completely different from that in the case of Pep 19-2.5. This means that protamine molecules fully replace the K^+ ions in the charged inner core saccharides and completely compensates the negative charge of the LPS Ra molecule despite the presence of 100 mM salt. This demonstrates that LPS Ra monolayer cannot act as a non-permeable barrier against protamine molecules when only monovalent K^+ ions are present (Fig. 11A).

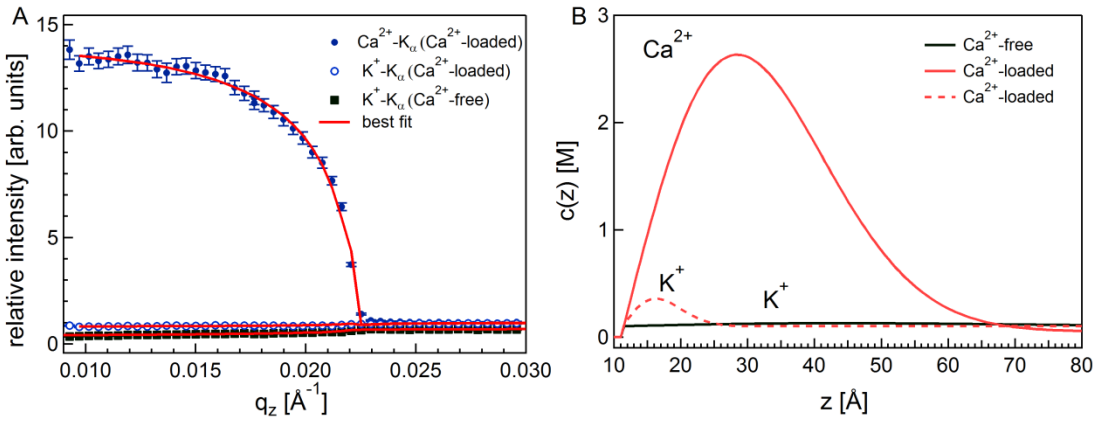

Fig. 6.10 *(A) Normalized fluorescence intensities from LPS Ra monolayers with protamine of K K_α (black solid squares) on Ca-free buffer, K K_α (blue open circles) and Ca K_α (blue solid circles) on Ca-loaded buffer. The red lines indicate the best fit from eq. 3 to the experimental data. . Vertical bars are ± standard deviation obtained from Gaussian fitting of the fluorescence spectra. The K K_α curve on Ca-free buffer is shifted with an offset of -0.3 to discriminate it from the one on Ca-loaded buffer (B) The corresponding ion concentration profile normal to the interface obtained from the fits for K^+ ions (black line) on Ca-free buffer, K^+ ions (broken line) and Ca^{2+} ions (red line) on Ca-loaded buffer.*

On Ca-loaded buffer, K^+ ions are mostly displaced from the head group region and the concentration profile (red broken line in Fig. 6.10B). The amount of K^+ ions remaining was below the detection limit (N = 0.2 ± 0.6). The maximum Ca^{2+} concentration is located at z_{max} = 30 (Fig. 11B), yielding the calculated number of Ca^{2+} ions associated with one LPS Ra molecule is N = 7.3 ± 0.5 (solid red line in Fig. 6.10B). This is almost the double of the Ca^{2+} ions associated with one LPS Ra molecule in the presence of Pep 19-2.5, which cannot be attributed to the compensation of negative charges in core saccharide units. In fact, the concentration of Ca^{2+} does not decay to the bulk level until it reaches z = 70 Å, which is far beyond of the thickness of saccharide head groups (z = 36 Å). Ca^{2+} ions tend to accumulate near the head group/water interface in the presence of protamine, which carries a large amount of positive charges (Q ~ + 20 e). This can be rather interpreted within the framework of dielectric continuum theory [157-159] which explains the accumulation of large, strongly polarizable ions as the gain in the cavitational energy with a small electrostatic energy penalty. Within this theory they calculated the density profiles of trivalent, monovalent and anions around a negatively charged colloidal particle and showed that the anions are pushed away from the colloidal

surface [159-160]. The similar tendency was also observed, though in a less pronounced manner, for Pep 19-2.5 carrying less positive charges (Q = + 7.7 e) and two orders of magnitudes lower in concentration.

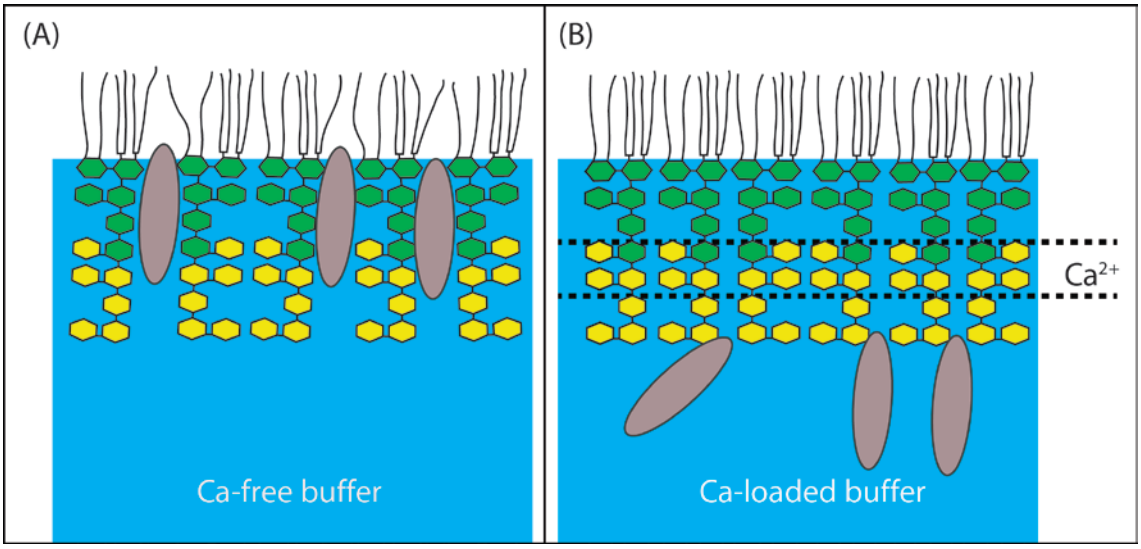

Fig. 6.11 *Illustration showing the suggested interaction mechanisms of LPS Ra monolayers with protamine molecules indicated in brown ellipses on Ca-free buffer (A) and on Ca-loaded buffer (B). The neutral and negatively charged sugar units are represented by yellow and green colors, respectively. The area between dashed lines indicates the position of the maximum concentration of the ions.*

7. Conclusions

In this thesis, the fine-structures, lateral correlations and diffusion at biological interfaces have been investigated by the combination of surface sensitive techniques, including grazing incidence X-ray scattering/fluorescence and single molecule tracking microscopy. A special focus was put on the physical modeling of biological surfaces coated with crowded layers of biomacromolecules, which still remains as an experimental challenge.

As the model of microorganism's surfaces coated with dense layers of proteins coupled to lipid anchors (such as *Trypansoma brucei*), the fine-structures and lateral correlation of membrane-anchored proteins were studied in Chapter 4. The designed model system consists of lipid monolayers at the air/water interface incorporating biotinylated lipids that allow for the coupling of non-crystalline proteins (neutravidin) at high surface densities. In the first step, the fine-structures of the lipid-protein layer normal to the membrane surface were characterized using specular X-ray reflectivity (XRR), confirming that the neutravidin proteins can be characterized as a uniform slab with the thickness of 4.7 nm and electron density of 0.388 è/Å^3. The lateral correlation of proteins was determined by grazing incidence small-angle X-ray scattering (GISAXS), where the measured scattering intensities were analyzed with a two-dimensional Percus-Yevick function within the framework of distorted wave Born approximation. This allowed for the calculation of the form and structure factors of non-crystalline neutravidin proteins coupled to the surface of fluid lipid monolayers for the first time, yielding the intermolecular distance between proteins d = 6.8 - 7.4 nm and the correlation length ξ ~20 nm. This finding suggests that the correlation between the neutravidin proteins can reach up to the third nearest neighbor. Moreover, from the methionine and cysteine amino acids content of neutravidin that carried sulfur atoms, the lateral density of proteins was determined through the S K_α fluorescence emission using grazing incidence X-ray fluorescence (GIXF). The obtained lateral density of proteins was estimated to be 2.2 $\times 10^{-8}$ mol/m^2 and thus d = 8.6 nm, showing a good agreement with that value calculated from GISAXS results. The results suggest that the unique combination of XRR, GISAXS and GIXF is a powerful tool to investigate the fine-structures in-plane

and out-of-plane of membranes as well as the correlation strength of the densely packed, non-crystalline proteins coupled to membrane surfaces.

In order to study the influence of molecular crowding on the lateral diffusion and the frictional coupling of membrane-anchored proteins, two fluorescence microscopy techniques were utilized in Chapter 5. Fluorescence recovery after photobleching (FRAP) is employed as an ensemble method to determine the average diffusion coefficient and mobile fraction, while single particle tracking (SPT) microscopy was used to obtained the local statistical details of the lateral diffusion of individual proteins. Similar to the model used in Chapter 4, neutravidin coupled to supported lipid membranes incorporating biotinylated lipids were used as the first model system. FRAP results suggested a distinct transition from free to obstacled diffusion, where the diffusion coefficient (D = 0.7 $\mu m^2/s$) abruptly dropped to zero at the inter-molecular distance of d = 6.9 nm. With aid of SPT experiments, this transition can be attributed to the transition from free diffusion to confined diffusion. As the directly relevant model of trypanosome surfaces, lipid vesicles incorporating GPI-anchored VSG were spread on a pre-deposited lipid monolayer. Mixing of VSG-incorporating vesicles and pure phospholipid vesicles makes it possible to control the lateral density of VSG proteins. Similar to neutravidin a clear decrease in the diffusion coefficient of VSG could be observed according to the increase in its lateral density. Within the framework of the modified continuum theory developed by Evans and Sackmann, this decrease in the diffusion coefficient was interpreted by the increase of the frictional coupling exerted on the proteins. Surprisingly, VSG proteins are still diffusive even in its crowded state. On the other hand, the addition of neutravidin suppressed the diffusion coefficient to zero, suggesting that neutravidin molecules act as "obstacles" to VSGs diffusion.

In Chapter 6, membrane-protein interactions in the presence of dense saccharide brushes have been studied to model the defense mechanism of bacteria against external intruders. As the model of outer membranes of gram negative bacteria, monolayers of lipopolysaccharides extracted from rough strains of *Salmonella enterica* (serovar Minnesota) (LPS Ra) was deposited at the air-water interface. To study the physical interaction between LPS Ra and antimicrobial peptides, two small peptides were selected;

fish protamine from herring and antisepsis peptide drug (Pep 19-2.5). LPS Ra monolayers were deposited onto a buffer in the presence and absence of Ca^{2+} ions, called Ca-loaded and Ca-free subphase, respectively, and peptides were injected underneath the monolayers while keeping the area per LPS Ra constant. In each step, XRR and GIXF were carried out to determine the structure and the concentration profile of ions and peptides normal to the membrane surface. A new analysis method was developed based on the Abelè's matrix formalism. It should be emphasized that the quantitative fitting of fluorescence intensity requires the full calculation of the illumination profiles. Therefore, the determination of electron density profiles by XRR is essential because the reflection and refraction of electromagnetic waves in thin stratified systems significantly depend on the electronic structures. The newly developed procedure could reach a very high spatial resolution up to ± 3 Å in determining the peak positions of ion density profiles, which is unbeatable with other spectroscopic methods. GIXF analysis yielded 5.9 × K^+ ions are associated with one LPS Ra molecule Ca-free subphase, while K^+ ions were completely displaced by 3.5 × Ca^{2+} on Ca-loaded subphase. In the presence of peptides, the results revealed two different physical interactions between the cationic peptides and the bacterial outer membranes. Pep 19-2.5 molecules adsorbed near uncharged carbohydrate groups but could not penetrate into the dense, negatively charged core carbohydrate head groups on Ca^{2+}-loaded subphase. In contrast, protamine molecules are pushed further apart from the membrane surface on Ca^{2+}-loaded subphase. On Ca^{2+}-free subphase, Pep 19-2.5 molecules could penetrate up to the concentrated inner core carbohydrate head groups, while protamine molecules adsorbed to the air-water interface and hence destroyed the layered structures. The results demonstrated the combination of XRR and GIXF allows for the discrimination of different modes of interactions between biological membranes and proteins at the molecular level.

Appendix

A.1 Form Factor of some particle shapes

In the following a calculated form factors are provided for some basic shapes. For additional form factors one can refer to some text books [51, 85].

1. Full sphere

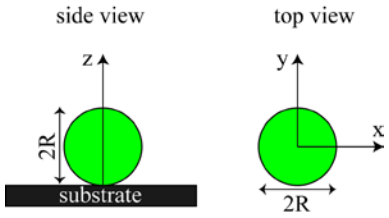

$$F(\mathbf{q},R)=4\pi R^3\left(\frac{\sin(qR)-qR\cos(qR)}{(qR)^3}\right)e^{iq_zR}$$

2. Cylinder

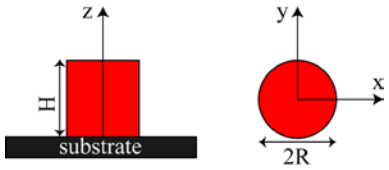

$$F(\mathbf{q},R,H)=4\pi R^2H\left(\frac{J_1(q_\parallel R)}{q_\parallel R}\right)\sin_c(q_zH/2)\,e^{iq_zH/2}$$

3. Truncated sphere

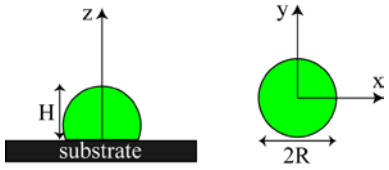

$$F(\mathbf{q},R,H)=e^{iq_z(H-R)}\int_{R-H}^{H}4\pi R_z^2\frac{J_1(q_\parallel R_z)}{q_\parallel R_z}e^{iq_zz}dz$$

$$R_z=\sqrt{R^2-z^2},\quad 0<H/R<2$$

4. Full spheroid

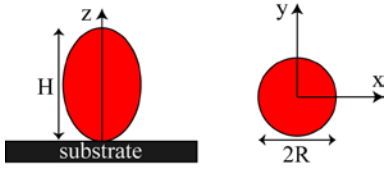

$$F(\mathbf{q},R,H)=e^{iq_zH/2}\int_0^{H/2}4\pi R_z^2\frac{J_1(q_\parallel R_z)}{q_\parallel R_z}\cos(iq_zz)\,dz$$

$$R_z=R\sqrt{1-4\frac{z^2}{H^2}}$$

5.Hemi-spheroid

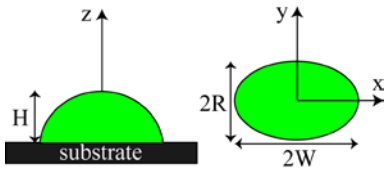

$$F(\mathbf{q},R,W,H)=2\pi\int_0^{H/2}R_zW_z\frac{J_1(\gamma)}{\gamma}e^{iq_zz}\,dz$$

$$R_z=R\sqrt{1-\frac{z^2}{H^2}};\quad W_z=W\sqrt{1-\frac{z^2}{H^2}};\quad \gamma=\sqrt{(q_xR_z)^2+(q_yW_z)^2}$$

A.2 Structure factor within the Percus-Yevik approximation

The structure factor within the Percus-Yevick approximation for hard spheres (particles interacting with hard core potential) with diameter D_{hs} and volume fraction η_{hs} is given by equation 2.43 as follows:

$$S(q_{\|}) = \left\{ 1 + 24 \frac{\eta_{hs} G(q_{\|} D_{hs})}{q_{\|} D_{hs}} \right\}$$

Where G is a function given as:

$$G(x) = \frac{\alpha(\sin x - x\cos x)}{x^2} + \frac{\beta(2x\sin x + (2 - x^2)\cos x - 2)}{x^3} + \frac{\gamma(-x^4\cos x + 4\left[(3x^2 - 6)\cos x + (x^3 - 6x)\sin x + 6\right])}{x^5},$$

with

$$\alpha = (1 + 2\eta_{hs})^2 / (1 - \eta_{hs})^4$$
$$\beta = -6\eta_{hs}(1 + \eta_{hs}/2)^2 / (1 - \eta_{hs})^4$$
$$\gamma = \alpha\eta_{hs}/2$$

A.3 the VSG proteins operates at a molecular crowding threshold

The impact of lateral protein density on the diffusion of VSG was quantified in supported membranes using FRAP measurements (shown in the following figure). The protein concentration is expressed in relative VSG coat density units. The solid lines represent the fit with Eq. 5.2. The diffusion coefficients (left panel) and mobile fractions (right panel) remain constant until the molecular crowding threshold is reached at ≈ 1.5-fold concentration of VSG coat density.

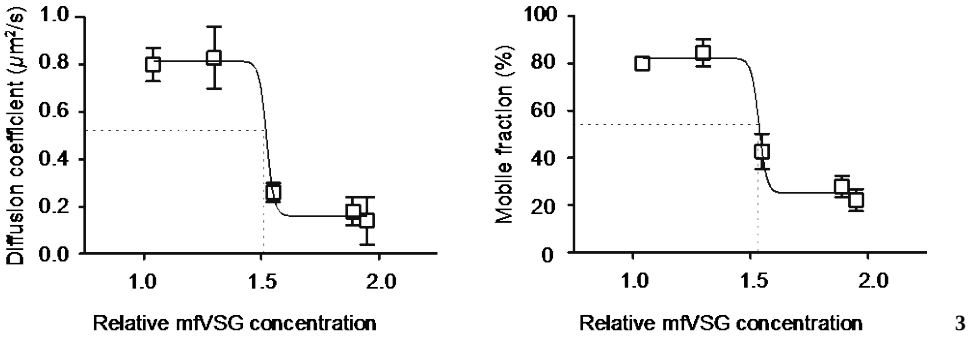

A.4 Background for SPT measurements of NA proteins

The distribution of diffusion coefficients of background measurements prior the injection of NA proteins is shown in the following. The distribution is similar to the case where NA proteins are in diluted state, indicating that the measured diffusion coefficients represents the diffusion coefficients of remaining NA proteins in the sample chamber.

[3] FRAP measurements were performed by Andreas Hartel (Department of Cell and Developmental Biology, University of Würzburg), the analysis were performed by wasim abuillan.

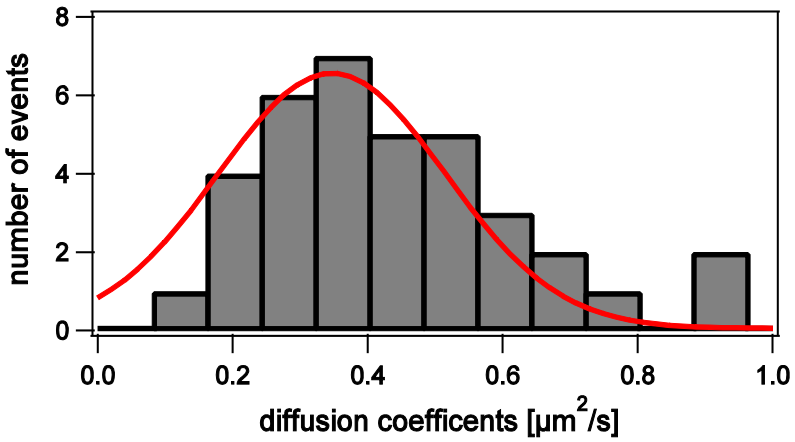

A.5 NA proteins act as "obstacles" to VSG diffusion[4]

The following figure shows the influence of varying concentrations of membrane-bound neutravidin on the diffusion of VSG. The black squares indicate VSG diffusion coefficients and grey squares represent the corresponding mobile fractions. Lines show the results of fitting with equation 2.8. The concentration of neutravidin on the artificial membranes was determined by the amount of DOPE-biotin. (A) At high concentrations of non-VSG (5 - 10% DOPE-biotin) the diffusion coefficients decrease more than 15-fold and VSG mobility is reduced from > 95% to 20%. (B) At low concentrations of non-VSG (0.1 - 1% DOPE-biotin) the diffusion coefficients are decreased four-fold, whereas the mobile fraction is reduced to 70%. The best fit results of the data points in the figure with equation 2.8 imply distinctly different γ values; γ = 11 (in the presence of neutravidin) and γ = 0.5 (VSG alone), respectively. This finding suggests that neutravidin molecules act as "obstacles" to VSGs diffusion and may explain why the VSG-diffusion coefficient on living trypanosomes was found to be smaller than on homogenous supported membranes

[4] FRAP measurements were performed by Andreas Hartel (Department of Cell and Developmental Biology, University of Würzburg), the analysis were performed by wasim abuillan.

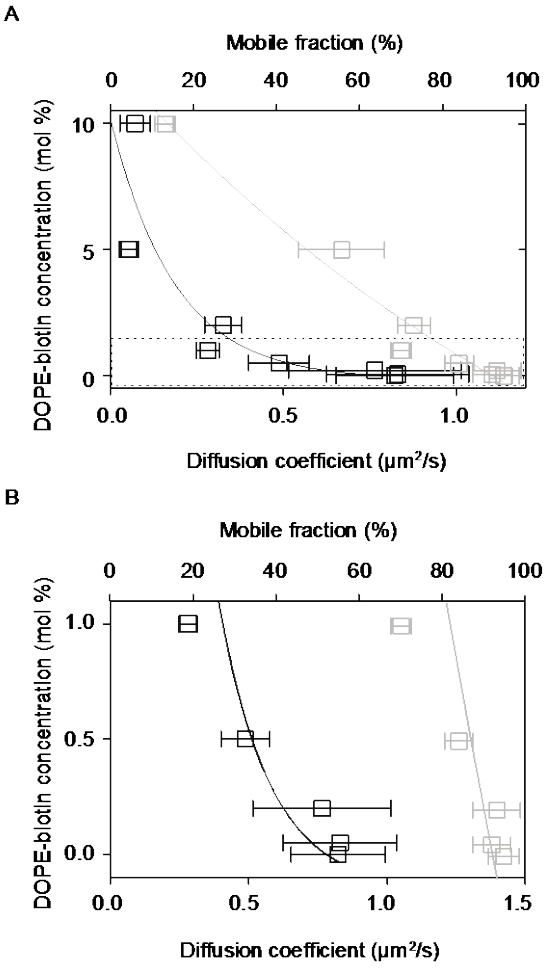
A
Mobile fraction (%)
0
20
40
60
80
100
10
5
0
DOPE-biotin concentration (mol %)
0.0
0.5
1.0
Diffusion coefficient (μm²/s)
B
Mobile fraction (%)
0
20
40
60
80
100
1.0
0.5
0.0
DOPE-biotin concentration (mol %)
0.0
0.5
1.0
1.5
Diffusion coefficient (μm²/s)

A.6 Chloride ions

Relative fluorescence intensity from LPS Ra monolayers of Cl K_α on Ca-loaded buffer is shown in open circles. (Inset) The corresponding ion concentration profiles normal to the interface obtained from the fit. The excess ions at the interface were below the detection limit (N ~ 0 ions per LPS Ra). Therefore, the chloride ions were neglected in the calculation of the total effective charge of LPS Ra molecules.

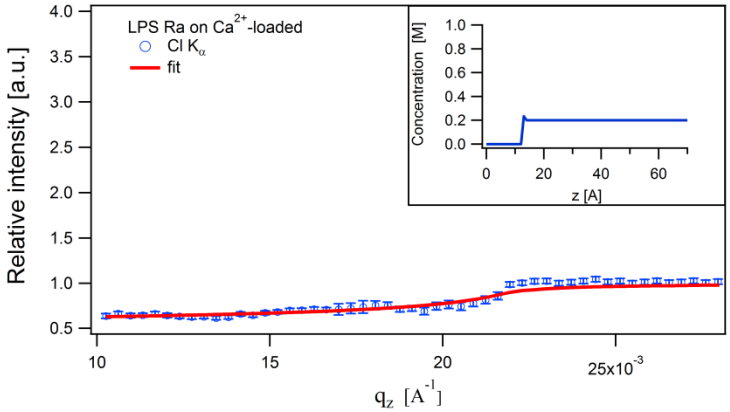

A.7 Number of Pep 19-2.5 molecules per one LPS Ra molecule

From XRR results the head group region has an increase of the electron density due to the penetration of P19.

Prior to P19 injection the measured electron density of the head group is given by

$$\rho_{m\_wihtoutP19} = \phi_H \rho_H + (1 - \phi_H)\rho_w \quad (1)$$

The volume fraction of the head group remains constant before and after the injection of P19-2.5 (table 6.1 and table 6.3) and the increase in the electron density owing to the replacement of water with P19-2.5 molecules. The influence of K^+ ions is neglected since their concentration at the head group is unchanged after the P19 injection as predicted from GIXF results.

In the same way, the measured electron density of the head group layer after Pep 19-2.5 injection is given by

$$\rho_{m\_withP19} = \phi_H \rho_H + \phi_{P19} \rho_{P19} + (1 - \phi_H - \phi_{P19}) \rho_w \quad (2)$$

where ρ_H and ρ_{P19} the electron densities in dry state of the head group and of Pep 19-2.5 respectively.

Subtraction of eq. 1 from eq. 2 yields:

$$\phi_{P19} = \frac{\Delta \rho_m}{\rho_{P19} - \rho_w} \quad (3)$$

Where $\Delta \rho_m = \rho_{m\_wihtP19} - \rho_{m\_wihtoutP19}$.

Pep 19-2.5 is small molecule → its electron density in dry state and its volume can be accurately calculated from its amino acid sequence using the same method for NA protein in chapter 4. $\rho_{P19} = 0.433$ and V_{P19}=3346 Å^3

This gives $\phi_{P19} = 23.2\%$

The lateral concentration of LPS Ra c = 1/(area per molecule) = 1/200 Å^2 = 5×10^{13} LPS/cm^2.

Within an area of A = 1 cm^2 and layer thickness of *d* = 27.1 Å, the number of Pep 19-2.5 molecules N is given by:

$$N = \phi_{P19} \frac{A.d}{V_{P19}} = 1.879 \times 10^{13}$$

This means → within the head group region there is 3.7 Pep 19-2.5 molecules per 10 LPS Ra molecules.

Bibliography

1. Tanaka, M. and E. Sackmann, *Polymer-supported membranes as models of the cell surface.* Nature, 2005. **437**(7059): p. 656-663.
2. Tanford, C., *The hydrophobic effect and the organization of living matter.* Science, 1978. **200**(4345): p. 1012-8.
3. Singer, S.J. and G.L. Nicolson, *The fluid mosaic model of the structure of cell membranes.* Science, 1972. **175**(4023): p. 720-31.
4. Yeagle, P.L., *The Structure of Biological Membranes, Second Edition*. 2010: Taylor & Francis.
5. Bruce Alberts, A.J., Julian Lewis, Martin Raff, Keith Roberts, and Peter Walter., *Membrane Structure*, in *Molecular Biology of the Cell*. 2002, Garland Science: New York.
6. Karp, G., *Cell and Molecular Biology*. 7 ed. 2013: John Wiley and Sons. 864.
7. Prusiner, S.B., *Prions.* Proceedings of the National Academy of Sciences of the United States of America, 1998. **95**(23): p. 13363-13383.
8. Stahl, N., et al., *Scrapie Prion Protein Contains a Phosphatidylinositol Glycolipid.* Cell, 1987. **51**(2): p. 229-240.
9. Ikezawa, H., *Glycosylphosphatidylinositol (GPI)-anchored proteins.* Biological & Pharmaceutical Bulletin, 2002. **25**(4): p. 409-417.
10. Mayor, S. and H. Riezman, *Sorting GPI-anchored proteins.* Nature Reviews: Molecular Cell Biology, 2004. **5**(2): p. 110-120.
11. Chesebro, B., et al., *Anchorless prion protein results in infectious amyloid disease without clinical scrapie.* Science, 2005. **308**(5727): p. 1435-1439.
12. Cox, D.L., R.R.P. Sing, and S.C. Yang, *Prion disease: Exponential growth requires membrane binding.* Biophysical Journal, 2006. **90**(11): p. L77-L79.
13. Breydo, L., et al., *Nonpolar substitution at the C-terminus of the prion protein, a mimic of the glycosylphosphatidylinositol anchor, partially impairs amyloid fibril formation.* Biochemistry, 2007. **46**(3): p. 852-861.
14. Schubert, T., et al., *Diffusion of glycosylphosphatidylinositol (GPI)-anchored bovine prion protein (PrPc) in supported lipid membranes studied by single-molecule and complementary ensemble methods.* Journal of Membrane Science, 2008. **321**(1): p. 61-68.
15. Rudd, P.M., et al., *Prion glycoprotein: Structure, dynamics, and roles for the sugars.* Biochemistry, 2001. **40**(13): p. 3759-3766.

16. Ferguson, M.A.J., *The structure, biosynthesis and functions of glycosylphosphatidylinositol anchors, and the contributions of trypanosome research.* Journal of Cell Science, 1999. **112**: p. 2799-2809.

17. Cross, G.A.M., *Antigenic variation in trypanosomes: Secrets surface slowly.* Bioessays, 1996. **18**(4): p. 283-291.

18. Borst, P., et al., *Antigenic variation in trypanosomes.* Archives of Medical Research, 1996. **27**(3): p. 379-388.

19. Donelson, J.E., K.L. Hill, and N.M.A. El-Sayed, *Multiple mechanisms of immune evasion by African trypanosomes.* Molecular and Biochemical Parasitology, 1998. **91**(1): p. 51-66.

20. Mclintock, L.M.L., C.M.R. Turner, and K. Vickerman, *Comparison of the Effects of Immune Killing Mechanisms on Trypanosoma-Brucei Parasites of Slender and Stumpy Morphology.* Parasite Immunology, 1993. **15**(8): p. 475-480.

21. O'Beirne, C., C.M. Lowry, and H.P. Voorheis, *Both IgM and IgG anti-VSG antibodies initiate a cycle of aggregation-disaggregation of bloodstream forms of Trypanosoma brucei without damage to the parasite.* Mol Biochem Parasitol, 1998. **91**(1): p. 165-93.

22. Cross, G.A.M., *Glycolipid Anchoring of Plasma-Membrane Proteins.* Annual Review of Cell Biology, 1990. **6**: p. 1-39.

23. Engstler, M., et al., *Hydrodynamic flow-mediated protein sorting on the cell surface of trypanosomes.* Cell, 2007. **131**(3): p. 505-515.

24. Lüderitz, O., et al., *Lipopolysaccharides of Gram-Negative Bacteria*, in *Current Topics in Membranes and Transport*. 1982, Academic Press. p. 79-151.

25. Raetz, C.R., *Biochemistry of endotoxins.* Annu Rev Biochem, 1990. **59**: p. 129-70.

26. Rietschel, E.T., et al., *Bacterial endotoxin: molecular relationships of structure to activity and function.* FASEB J, 1994. **8**(2): p. 217-25.

27. Alexander, C. and E.T. Rietschel, *Bacterial lipopolysaccharides and innate immunity.* Journal of Endotoxin Research, 2001. **7**(3): p. 167-202.

28. Evans, M.E. and M. Pollack, *Effect of antibiotic class and concentration on the release of lipopolysaccharide from Escherichia coli.* J Infect Dis, 1993. **167**(6): p. 1336-43.

29. Brandenburg, K., et al., *Peptide-based treatment of sepsis.* Applied Microbiology and Biotechnology, 2011. **90**(3): p. 799-808.

30. Brock, T.D., *The effect of salmine on bacteria.* Canadian Jour Microbiol, 1958. **4**((2)): p. 65-71.

31. Hansen, L.T., J.W. Austin, and T.A. Gill, *Antibacterial effect of protamine in combination with EDTA and refrigeration.* International Journal of Food Microbiology, 2001. **66**(3): p. 149-161.

32. Islam, N.M., T. Itakura, and T. Motohiro, *Antibacterial Spectra and Minimum Inhibition Concentrations of Clupeine and Salmine.* Nippon Suisan Gakkaishi, 1984. **50**(10): p. 1705-1708.

33. Lugtenberg, B. and L. Van Alphen, *Molecular architecture and functioning of the outer membrane of Escherichia coli and other gram-negative bacteria.* Biochim Biophys Acta, 1983. **737**(1): p. 51-115.

34. Vaara, M., *Agents that increase the permeability of the outer membrane.* Microbiol Rev, 1992. **56**(3): p. 395-411.

35. Beutler, B. and E.T. Rietschel, *Innate immune sensing and its roots: the story of endotoxin.* Nature Reviews Immunology, 2003. **3**(2): p. 169-176.

36. Kotra, L.P., et al., *Dynamics of the lipopolysaccharide assembly on the surface of Escherichia coli.* J. Am. Chem. Soc., 1999. **121**(38): p. 8707-8711.

37. Shroll, R.M. and T.P. Straatsma, *Molecular structure of the outer bacterial membrane of Pseudomonas aeruginosa via classical simulation.* Biopolymers, 2002. **65**(6): p. 395-407.

38. Lins, R.D. and T.P. Straatsma, *Computer simulation of the rough lipopolysaccharide membrane of Pseudomonas aeruginosa.* Biophys. J, 2001. **81**(2): p. 1037-1046.

39. Pink, D.A., et al., *Divalent calcium ions inhibit the penetration of protamine through the polysaccharide brush of the outer membrane of Gram-negative bacteria.* Langmuir, 2003. **19**(21): p. 8852-8858.

40. Schneck, E., et al., *Quantitative determination of ion distributions in bacterial lipopolysaccharide membranes by grazing-incidence X-ray fluorescence.* Proceedings of the National Academy of Sciences of the United States of America, 2010. **107**(20): p. 9147-9151.

41. Leroy, F., et al., *In situ GISAXS study of the growth of Pd on MgO(001).* Applied Surface Science, 2004. **238**(1-4): p. 233-237.

42. Revenant, C., et al., *Quantitative analysis of grazing incidence small-angle x-ray scattering: Pd/MgO(001) growth.* Physical Review B, 2004. **69**(3).

43. Revenant, C., et al., *Defect-pinned nucleation, growth, and dynamic coalescence of Ag islands on MgO(001): An in situ grazing-incidence small-angle x-ray scattering study.* Physical Review B, 2009. **79**(23).

44. Stangl, J., et al., *Self-assembled carbon-induced germanium quantum dots studied by grazing-incidence small-angle x-ray scattering.* Applied Physics Letters, 1999. **74**(25): p. 3785-3787.

45. Metzger, T.H., et al., *Shape, size, strain and correlations in quantum dot systems studied by grazing incidence X-ray scattering methods.* Thin Solid Films, 1998. **336**(1-2): p. 1-8.

46. Metzger, T.H., et al., *Grazing incidence x-ray scattering: an ideal tool to study the structure of quantum dots.* Journal of Physics D: Applied Physics, 1999. **32**(10A): p. A202-A207.

47. Kegel, I., et al., *Vertical alignment of multilayered quantum dots studied by x-ray grazing-incidence diffraction.* Physical Review B, 1999. **60**(4): p. 2516-2521.

48. Muller-Buschbaum, P., *Grazing incidence small-angle X-ray scattering: an advanced scattering technique for the investigation of nanostructured polymer films.* Analytical and Bioanalytical Chemistry, 2003. **376**(1): p. 3-10.

49. Muller-Buschbaum, P., R. Cubitt, and W. Petry, *Nanostructured diblock copolymer films: A grazing incidence small-angle neutron scattering study.* Langmuir, 2003. **19**(19): p. 7778-7782.

50. Rossetti, F.F., et al., *Structures of regenerated cellulose films revealed by grazing incidence small-angle x-ray scattering.* Biointerphases, 2008. **3**(4): p. 117-127.

51. Renaud, G., R. Lazzari, and F. Leroy, *Probing surface and interface morphology with Grazing Incidence Small Angle X-Ray Scattering.* Surface Science Reports, 2009. **64**(8): p. 255-380.

52. Tanford, C., *The Hydrophobic Effect*. 1980, New York: Wiley.

53. MaAuliffe, C., *Solubility in Water of Paraffin, Cycloparaffin, Olefin, Acetylene, Cycloolefin, and Aromatic Hydrocarbons1*. Journal of Physical Chemistry 1966. **70**: p. 8.

54. Sackmann, E., *Biological Membranes Architecture and Function*, in *Handbook of Biological Physics: Structure and Dynamics of Membranes*, R. Lipowsky and E. Sackmann, Editors. 1995, North Holland: New York.

55. Cevc, G. and D. Marsh, *Phospholipid Bilayer: physical principles and models*. Cell Biology ed. E. Bittar. Vol. 5. 1988, New York: John Wiley and Sons.

56. Einstein, A., *Investigations on the Theory of the Brownian Movement*, ed. R. F¨urth. 1956, New York.

57. Saffman, P.G., *Brownian motion in thin sheets of viscous fluid.* Journal of Fluid Mechanics, 1976. **73**(04): p. 593-602.

58. Saffman, P.G. and M. Delbruck, *Brownian motion in biological membranes.* Proc Natl Acad Sci U S A, 1975. **72**(8): p. 3111-3.

59. Vaz, W.L., R.M. Clegg, and D. Hallmann, *Translational diffusion of lipids in liquid crystalline phase phosphatidylcholine multibilayers. A comparison of experiment with theory.* Biochemistry, 1985. **24**(3): p. 781-6.

60. Merkel, R., E. Sackmann, and E. Evans, *Molecular Friction and Epitactic Coupling between Monolayers in Supported Bilayers.* Journal De Physique, 1989. **50**(12): p. 1535-1555.

61. Hughes, B., B. Pailthorpe, and L. White, *The translational and rotational drag on a cylinder moving in a membrane.* Journal of Fluid Mechanics, 1981. **110**: p. 13.

62. Criado, M., et al., *Translational diffusion of acetylcholine receptor (monomeric and dimeric forms) of Torpedo marmorata reconstituted into phospholipid bilayers studied by fluorescence recovery after photobleaching.* Biochemistry, 1982. **21**(23): p. 5750-5755.

63. Vaz, W.L.C., et al., *Size dependence of the translational diffusion of large integral membrane proteins in liquid-crystalline phase lipid bilayers. A study using fluorescence recovery after photobleaching.* Biochemistry, 1982. **21**(22): p. 5608-5612.

64. Evans, E. and E. Sackmann, *Translational and rotational drag coefficients for a disk moving in a liquid membrane associated with a rigid substrate.* Journal of Fluid Mechanics, 1988. **194**: p. 8.

65. Tanaka, M., et al., *Frictional drag and electrical manipulation of recombinant proteins in polymer-supported membranes.* Langmuir, 2007. **23**(10): p. 5638-44.

66. Purrucker, O., et al., *Control of frictional coupling of transmembrane cell receptors in model cell membranes with linear polymer spacers.* Phys Rev Lett, 2007. **98**(7): p. 078102.

67. Saxton, M.J., *Lateral Diffusion in an Archipelago - the Distance Dependence of the Diffusion Constant.* Biophysical Journal, 1987. **51**(2): p. A542-A542.

68. Saxton, M.J., *Lateral Diffusion in an Archipelago - the Effect of Mobile Obstacles.* Biophysical Journal, 1987. **52**(6): p. 989-997.

69. Tahir-Kheli, R.A. and N. El-Meshad, *Correlated diffusion in two-dimensional systems.* Physical Review B, 1985. **32**(10): p. 6166-6175.

70. van Beijeren, H. and R. Kutner, *Mean square displacement of a tracer particle in a hard-core lattice gas.* Physical Review Letters, 1985. **55**(2): p. 238-241.

71. Sentenac, A. and J. Daillant, *Statistical Aspects of Wave Scattering at Rough Surfaces*, in *X-ray and Neutron Reflectivity*, J. Daillant and A. Gibaud, Editors. 2009, Springer Berlin Heidelberg. p. 59-84.

72. Wong, P., *Scattering by inhomogeneous systems with rough internal surfaces: Porous solids and random-field Ising systems.* Phys Rev B Condens Matter, 1985. **32**(11): p. 7417-7424.

73. Sinha, S.K., et al., *X-ray and neutron scattering from rough surfaces.* Phys Rev B Condens Matter, 1988. **38**(4): p. 2297-2311.

74. L. Névot, P.C., *Caractérisation des surfaces par réflexion rasante de rayons X. Application à l'étude du polissage de quelques verres silicates.* Rev. Phys. Appl. , 1980. **15**(3): p. 761-779

75. Parratt, L.G., *Surface Studies of Solids by Total Reflection of X-Rays.* Physical Review, 1954. **95**(2): p. 359-369.

76. Azzam, R.M.A. and N.M. Bashara, *Ellipsometry and Polarized Light*. 1977: North-Holland.

77. Als-Nielsen, J. and D. McMorrow, *Refraction and reflection from interfaces*, in *Elements of Modern X-ray Physics*. 2011, John Wiley & Sons, Inc. p. 69-112.

78. Rauscher, M., et al., *Grazing incidence small angle x-ray scattering from free-standing nanostructures.* Journal of Applied Physics, 1999. **86**(12): p. 6763-6769.

79. Rauscher, M., T. Salditt, and H. Spohn, *Small-angle x-ray scattering under grazing incidence: The cross section in the distorted-wave Born approximation.* Physical Review B, 1995. **52**(23): p. 16855-16863.

80. Lazzari, R., et al., *Adhesion of growing nanoparticles at a glance: Surface differential reflectivity spectroscopy and grazing incidence small angle x-ray scattering.* Physical Review B, 2009. **79**(12).

81. Sinha, S.K., et al., *X-Ray and Neutron-Scattering from Rough Surfaces.* Physical Review B, 1988. **38**(4): p. 2297-2311.

82. Yoneda, Y., *Anomalous Surface Reflection of X Rays.* Physical Review, 1963. **131**(5): p. 2010-2013.

83. Pedersen, J.S., *Determination of Size Distributions from Small-Angle Scattering Data for Systems with Effective Hard-Sphere Interactions.* Journal of Applied Crystallography, 1994. **27**: p. 595-608.

84. Pedersen, J.S., *Small-Angle Scattering from Precipitates - Analysis by Use of a Polydisperse Hard-Sphere Model.* Physical Review B, 1993. **47**(2): p. 657-665.

85. Lazzari, R., *Grazing Incidence Small-Angle X-Ray Scattering from Nanostructures*, in *X-ray and Neutron Reflectivity*, J. Daillant and A. Gibaud, Editors. 2009, Springer Berlin Heidelberg. p. 283-342.

86. Babonneau, D., *FitGISAXS: software package for modelling and analysis of GISAXS data using IGOR Pro.* Journal of Applied Crystallography, 2010. **43**: p. 929-936.

87. Als-Nielsen, J. and D. McMorrow, *Refraction and reflection from interfaces*, in *Elements of Modern X-ray Physics*. 2001, John Wiley & Sons, Inc. p. 69 - 112.

88. Yun, W.B. and J.M. Bloch, *X-Ray near Total External Fluorescence Method - Experiment and Analysis.* Journal of Applied Physics, 1990. **68**(4): p. 1421-1428.

89. Novikova, N.N., et al., *X-ray fluorescence methods for investigations of lipid/protein membrane models.* Journal of Synchrotron Radiation, 2005. **12**(4): p. 511-516.

90. Ohta, K. and H. Ishida, *Matrix Formalism for Calculation of Electric-Field Intensity of Light in Stratified Multilayered Films.* Applied Optics, 1990. **29**(13): p. 1952-1959.

91. Daillant, J. and A. Gibaud, *Specular Reflectivity from Smooth and Rough Surfaces*, in *X-ray and Neutron Reflectivity: Principles and Applications*. 1999, Springer Berlin Heidelberg. p. 87-120.

92. Boggs, P.T., et al., *Odrpack - Software for Weighted Orthogonal Distance Regression.* Acm Transactions on Mathematical Software, 1989. **15**(4): p. 348-364.

93. Brandenburg, K. and U. Seydel, *Physical aspects of structure and function of membranes made from lipopolysaccharides and free lipid A.* Biochimica et Biophysica Acta (BBA) - Biomembranes, 1984. **775**(2): p. 225-238.

94. Jiao, B.H., M. Freudenberg, and C. Galanos, *Characterization of the Lipid-a Component of Genuine Smooth-Form Lipopolysaccharide.* European Journal of Biochemistry, 1989. **180**(3): p. 515-518.

95. Hiller, Y., et al., *Biotin Binding to Avidin - Oligosaccharide Side-Chain Not Required for Ligand Association.* Biochemical Journal, 1987. **248**(1): p. 167-171.

96. Hiller, Y., et al., *[6] Nonglycosylated avidin*, in *Methods in Enzymology*. 1990, Academic Press. p. 68-70.

97. Ratanabanangkoon, P., et al., *Two-dimensional streptavidin crystals on giant lipid bilayer vesicles.* Langmuir, 2002. **18**(11): p. 4270-4276.

98. Jap, B.K., et al., *2d Crystallization - from Art to Science.* Ultramicroscopy, 1992. **46**(1-4): p. 45-84.

99. Gill, T.A., D.S. Singer, and J.W. Thompson, *Purification and analysis of protamine.* Process Biochemistry, 2006. **41**(8): p. 1875-1882.

100. Ottensmeyer, F.P., R.F. Whiting, and A.P. Korn, *Three Dimensional Structure of Herring Sperm Protamine Y-I with the Aid of Dark Field Electron Microscopy.* Proceedings of the National Academy of Sciences of the United States of America, 1975. **72**(12): p. 4953-4955.

101. Kowalski, I., et al., *Physicochemical and Biological Characterization of Anti-Endotoxin Peptides and Their Influence on Lipid Properties.* Protein and Peptide Letters, 2010. **17**(11): p. 1328-1333.

102. Gutsmann, T., et al., *New Antiseptic Peptides To Protect against Endotoxin-Mediated Shock.* Antimicrobial Agents and Chemotherapy, 2010. **54**(9): p. 3817-3824.

103. Abraham, T., et al., *Monolayer Film Behavior of Lipopolysaccharide from Pseudomonas aeruginosa at the Air-Water Interface.* Biomacromolecules, 2008. **9**(10): p. 2799-2804.

104. Kern, W. and D. Puotinen, *Cleaning solutions based on hydrogen peroxide for use in silicon semiconductor technology.* RCA Review, 1970. **31**: p. 19.

105. Rigaud, J.L., M.T. Paternostre, and A. Bluzat, *Mechanisms of Membrane-Protein Insertion into Liposomes during Reconstitution Procedures Involving the Use of Detergents .2. Incorporation of the Light-Driven Proton Pump Bacteriorhodopsin.* Biochemistry, 1988. **27**(8): p. 2677-2688.

106. Erb, E.M., et al., *Integrin alpha IIb beta 3 reconstituted into lipid bilayers is nonclustered in its activated state but clusters after fibrinogen binding.* Biochemistry, 1997. **36**(24): p. 7395-7402.

107. Böttcher, C.J.F. and F.P. Woodford, *Lipid and fatty-acid composition of plasma lipoproteins in cases of aortic atherosclerosis.* Journal of Atherosclerosis Research, 1961. **1**(5–6): p. 434-443.

108. Metin, T., *Reflectivity of x-rays from surfaces*, in *X-Ray Scattering from Soft-Matter Thin Films*. 1999, Springer Berlin Heidelberg. p. 5-31.

109. Nelson, A., *Co-refinement of multiple-contrast neutron/X-ray reflectivity data using MOTOFIT.* Journal of Applied Crystallography, 2006. **39**: p. 273-276.

110. Ponchut, C., et al., *MAXIPIX, a fast readout photon-counting X-ray area detector for synchrotron applications.* Journal of Instrumentation, 2011. **6**.

111. Soumpasis, D.M., *Theoretical analysis of fluorescence photobleaching recovery experiments.* Biophys J, 1983. **41**(1): p. 95-7.

112. Axelrod, D., et al., *Mobility measurement by analysis of fluorescence photobleaching recovery kinetics.* Biophys J, 1976. **16**(9): p. 1055-69.

113. Saxton, M.J., *Single-particle tracking: The distribution of diffusion coefficients.* Biophysical Journal, 1997. **72**(4): p. 1744-1753.

114. Azarnia, R., G. Dahl, and W.R. Loewenstein, *Cell Junction and Cyclic AMP:III. Promotion of Junctional Membrane Permeability and Junctional Membrane Particles in a Junction Deficient Cell Type.* The Journal of Membrane Biology, 1981. **63**: p. 13.

115. Flagg-Newton, J.L., G. Dahl, and W.R. Loewenstein, *Cell Junction and Cyclic AMP:I. Upregulation of Junctional Membrane Permeability and Junctional Membrane Particles by Administration of Cyclic Nucleotide or Phosphodiesterase Inhibitor.* The Journal of Membrane Biology, 1981. **63**: p. 16.

116. King, G.I. and W. Stoecknius, *The Location of Retinal in the Purple Membrane Profile by Neutron Diffraction.* Journal of Molecular Biology, 1979. **130**: p. 9.

117. Abney, J.R. and J.C. Owicki, *Theories of protein-lipid and protein-protein interactions in membranes*, in *Progress in Protein-Lipid Interactions*, W.D. Pons, Editor. 1985, Elsevier Science Publishers B. V.

118. Markovics, J., L. Glass, and G.G. Maul, *Pore patterns on nuclear membranes.* Experimental Cell Research, 1974. **85**(2): p. 443-451.

119. Perelson, A.S., *Spatial distribution of surface immunoglobulin on B lymphocytes: Local ordering.* Experimental Cell Research, 1978. **112**(2): p. 309-321.

120. Pearson, L.T., et al., *Pair distribution functions of bacteriorhodopsin and rhodopsin in model bilayers.* Biophysical Journal, 1983. **43**(2): p. 167-174.

121. Pearson, L.T., J. Edelman, and S.I. Chan, *Statistical mechanics of lipid membranes. Protein correlation functions and lipid ordering.* Biophysical Journal, 1984. **45**(5): p. 863-871.

122. He, J.B., et al., *Self-Assembly of Tobacco Mosaic Virus at Oil/Water Interfaces.* Langmuir, 2009. **25**(9): p. 4979-4987.

123. Yang, L., et al., *Structure and interaction in 2D assemblies of tobacco mosaic viruses.* Soft Matter, 2009. **5**(24): p. 4951-4961.

124. Fukuto, M., et al., *Effects of surface ligand density on lipid-monolayer-mediated 2D assembly of proteins.* Soft Matter, 2010. **6**(7): p. 1513-1519.

125. Romao, R.I.S. and A.M.G. da Silva, *Phase behaviour and morphology of binary mixtures of DPPC with stearonitrile, stearic acid, and octadecanol at the air-water interface.* Chemistry and Physics of Lipids, 2004. **131**(1): p. 27-39.

126. Sanchez-Martin, M.J., et al., *A Langmuir monolayer study of the interaction of E1(145-162) hepatitis G virus peptide with phospholipid membranes.* J Phys Chem B, 2010. **114**(1): p. 448-56.

127. Chen, Y.Y., R.G. Sun, and B. Wang, *Monolayer behavior of binary systems of betulinic acid and cardiolipin: Thermodynamic analyses of Langmuir monolayers and AFM study of Langmuir-Blodgett monolayers.* Journal of Colloid and Interface Science, 2011. **353**(1): p. 294-300.

128. Majewski, J., et al., *Packing of ganglioside-phospholipid monolayers: An X-ray diffraction and reflectivity study.* Biophysical Journal, 2001. **81**(5): p. 2707-2715.

129. Weygand, M., et al., *Bacterial S-layer protein coupling to lipids: X-ray reflectivity and grazing incidence diffraction studies.* Biophysical Journal, 1999. **76**(1): p. 458-468.

130. Malkova, S., et al., *X-ray reflectivity studies of cPLA(2)alpha-C2 domains adsorbed onto Langmuir monolayers of SOPC.* Biophysical Journal, 2005. **89**(3): p. 1861-1873.

131. Vogel, M., et al., *Thermal unbinding of highly oriented phospholipid membranes.* Physical Review Letters, 2000. **84**(2): p. 390-393.

132. Novakova, E., K. Giewekemeyer, and T. Salditt, *Structure of two-component lipid membranes on solid support: An x-ray reflectivity study.* Physical Review E, 2006. **74**(5).

133. Rosano, C., P. Arosio, and M. Bolognesi, *The X-ray three-dimensional structure of avidin.* Biomolecular Engineering, 1999. **16**(1-4): p. 5-12.

134. Matthews, B.W., *Solvent content of protein crystals.* J Mol Biol, 1968. **33**((2)): p. 491-497.

135. Harpaz, Y., M. Gerstein, and C. Chothia, *Volume Changes on Protein-Folding.* Structure, 1994. **2**(7): p. 641-649.

136. Baus, M. and J.L. Colot, *Thermodynamics and Structure of a Fluid of Hard-Rods, Disks, Spheres, or Hyperspheres from Rescaled Virial Expansions.* Physical Review A, 1987. **36**(8): p. 3912-3925.

137. Lee, B., et al., *Structural analysis of block copolymer thin films with grazing incidence small-angle X-ray scattering.* Macromolecules, 2005. **38**(10): p. 4311-4323.

138. Comes, R., M. Lambert, and A. Guinier, *The chain structure of BaTiO3 and KNbO3.* Solid State Communications, 1968. **6**(10): p. 715-719.

139. Padmanabhan, V., et al., *Specific ion adsorption and short-range interactions at the air aqueous solution interface.* Physical Review Letters, 2007. **99**(8).

140. Huang, T.S. and R.J. De Lange, *Egg White Avidin Part 2 Isolation Composition and Amino-Acid Sequences of the Tryptic Peptides.* Journal of Biological Chemistry, 1971. **246**(3): p. 686-697.

141. Salditt, T., *Thermal fluctuations and stability of solid-supported lipid membranes.* J. Phys.: Condens. Matter 2005. **17**(6): p. 29.

142. Wang, S.T., M. Fukuto, and L. Yang, *In situ x-ray reflectivity studies on the formation of substrate-supported phospholipid bilayers and monolayers.* Physical Review E, 2008. **77**(3).

143. Miller, C.E., et al., *Characterization of biological thin films at the solid-liquid interface by X-ray reflectivity.* Physical Review Letters, 2005. **94**(23).

144. Kuhl, T.L., et al., *A neutron reflectivity study of polymer-modified phospholipid monolayers at the solid-solution interface: Polyethylene glycol-lipids on silane-modified substrates.* Biophysical Journal, 1998. **75**(5): p. 2352-2362.

145. Hetzer, M., et al., *Asymmetric molecular friction in supported phospholipid bilayers revealed by NMR measurements of lipid diffusion.* Langmuir, 1998. **14**(5): p. 982-984.

146. Kuhner, M., R. Tampe, and E. Sackmann, *Lipid Monolayer and Bilayer Supported on Polymer-Films - Composite Polymer-Lipid Films on Solid Substrates.* Biophysical Journal, 1994. **67**(1): p. 217-226.

147. Hancock, R.E.W. and D.S. Chapple, *Peptide antibiotics.* Antimicrobial Agents and Chemotherapy, 1999. **43**(6): p. 1317-1323.

148. Oliveira, R.G., et al., *Physical mechanisms of bacterial survival revealed by combined grazing-incidence X-ray scattering and Monte Carlo simulation.* Comptes Rendus Chimie, 2009. **12**(1-2): p. 209-217.

149. Daillant, J., et al., *Interaction of Cations with a Fatty-Acid Monolayer - a Grazing-Incidence X-Ray-Fluorescence and Reflectivity Study.* Langmuir, 1991. **7**(4): p. 611-614.

150. Helm, C.A., et al., *Synchrotron X-Ray-Diffraction and Reflection Studies of Phospholipid Monolayers at the Air-Water-Interface.* Biophysical Journal, 1987. **51**(2): p. A205-A205.

151. Kjaer, K., et al., *Synchrotron X-Ray-Diffraction and Reflection Studies of Arachidic Acid Monolayers at the Air-Water-Interface.* Journal of Physical Chemistry, 1989. **93**(8): p. 3200-3206.

152. *Supplemental Material*. 2012.

153. Lins, R.D. and T.P. Straatsma, *Computer simulation of the rough lipopolysaccharide membrane of Pseudomonas aeruginosa.* Biophysical Journal, 2001. **81**(2): p. 1037-1046.

154. Kotra, L.P., et al., *Dynamics of the lipopolysaccharide assembly on the surface of Escherichia coli.* Journal of the American Chemical Society, 1999. **121**(38): p. 8707-8711.

155. Kaconis, Y., et al., *Biophysical Mechanisms of Endotoxin Neutralization by Cationic Amphiphilic Peptides.* Biophysical Journal, 2011. **100**(11): p. 2652-2661.

156. Potter, R., L.T. Hansen, and T.A. Gill, *Inhibition of foodborne bacteria by native and modified protamine: Importance of electrostatic interactions.* International Journal of Food Microbiology, 2005. **103**(1): p. 23-34.

157. Levin, Y., A.P. dos Santos, and A. Diehl, *Ions at the Air-Water Interface: An End to a Hundred-Year-Old Mystery?* Physical Review Letters, 2009. **103**(25).

158. dos Santos, A.P., A. Diehl, and Y. Levin, *Surface Tensions, Surface Potentials, and the Hofmeister Series of Electrolyte Solutions.* Langmuir, 2010. **26**(13): p. 10778-10783.

159. dos Santos, A.P., A. Bakhshandeh, and Y. Levin, *Effects of the dielectric discontinuity on the counterion distribution in a colloidal suspension.* Journal of Chemical Physics, 2011. **135**(4).

160. dos Santos, A.P., A. Diehl, and Y. Levin, *Colloidal charge renormalization in suspensions containing multivalent electrolyte.* Journal of Chemical Physics, 2010. **132**(10).